THE USE OF FRICTION-SURFACE PROCESSING AS A METHOD OF CORROSION PROTECTION OF A FRICTION-STIR WELD IN THE AL-LI-CU ALLOY AA2050-T851

by

BEN JAMES MELROSE

A thesis submitted to
The University of Birmingham
for the degree of
MRes in Science and Engineering of Materials

Department of Metallurgy and Materials
The University of Birmingham
September 2010

Abstract

Friction-surface processing (FSP) was explored as a possible method for mitigating corrosion of a friction-stir weld (FSW) in the Al-Li-Cu alloy AA2050-T851. The microstructure, hardness and corrosion behaviour of the base alloy, the FSW and the FSP regions was examined. The base alloy showed susceptibility to pitting parallel to the rolling direction and some intragranular corrosion, but no susceptibility to intergranular corrosion (IGC) or exfoliation corrosion. The FSW showed evidence of IGC in the nugget region and thermomechanically-affected zone (TMAZ), and exfoliation corrosion in the heat-affected zone (HAZ). Regions of the base alloy that had been treated by FSP also showed some IGC. Treatment of the FSW with FSP showed some indication of a reduction of IGC, and there was no evidence of exfoliation corrosion in the FSP-treated FSW-HAZ, but further work needs to be carried out to confirm this.

Acknowledgements

This project was sponsored by Alcan, Centre de Reserches de Voreppe and the University of Birmingham.

I would firstly like to thank my supervisor Dr. A. J. Davenport for her continued invaluable advice, support and guidance throughout my time at the University of Birmingham, as well as the technicians, and administrative staff of the Metallurgy and Materials Department who made the project possible.

Particular thanks go to Christine Henon and her team at Alcan, Centre de Reserches de Voreppe for their guidance and hospitality.

Finally, thank you to my family for their support, and friends for making my time in Birmingham so thoroughly enjoyable.

CONTENTS

Chapter 1 – Introduction **1**

Chapter 2 –Literature Review **3**

2.1	Al-Li introduction	3
2.2	Metallurgy of Al-Li-X alloys	3
2.2.1	Al-Li-Cu system	6
2.2.2	Al-Li-Cu-Mg system	7
2.2.3	Al-Li-Cu-Mg-Ag-Zr system	7
2.3	Effect of ageing conditions	9
2.4	Corrosion introduction	11
2.4.1	Corrosion of aluminium	11
2.4.2	Corrosion mechanisms in aluminium	14
2.4.3	Influence of alloying elements	19
2.4.4	Corrosion of Al-Li-Cu-X alloys	19
2.5	Friction-stir welding introduction	22
2.5.1	Friction-stir welding process	22
2.5.2	Microstructure of FSW in aluminium alloys	24
2.5.2.1	Heat-affected zone	25
2.5.2.2	Thermomechanically-affected zone	26
2.5.2.3	Nugget	27
2.6	Friction-surface processing	29
2.7	Microstructural properties of FSW and FSP aluminium alloys	30
2.8	Corrosion properties of FSW and FSP aluminium alloys	32

Chapter 3 – Experimental Procedure **35**

3.1	Material composition	35
3.2	Sample preparation	37
3.3	Microstructural characterisation	38
3.4	Microhardness testing	38
3.5	Immersion testing	38
3.6	MASTMAASIS Testing	39

CONTENTS

Chapter 4 – Results **40**

4.1	Microstructural characteristics	40
4.1.1	Base material microstructure	40
4.1.2	FSW Microstructure	40
4.1.3	FSP Microstructure	43
4.2	Microhardness results	46
4.2.1	FSW Microhardness	46
4.2.2	FSP Microhardness	47
4.3	MASTMAASIS results	49
4.4	Immersion results	53
4.4.1	Immersion surface characteristics	53
4.4.1.1	FSW Immersion characteristics	53
4.4.1.2	Cold FSP Immersion characteristics	54
4.4.1.3	Hot FSP Immersion characteristics	56
4.4.2	Depth of attack analysis	57
4.4.2.1	Base material depth of attack	58
4.4.2.2	FSW depth of attack	59
4.4.2.3	FSP depth of attack	66
4.4.3	FSW with Hot FSP(r) immersion characteristics	72
4.4.4	FSW with Hot FSP(r) depth of attack analysis	74
4.4.4.1	FSW Nugget with Hot FSP(r) depth of attack	74
4.4.4.2	FSW TMAZ with Hot FSP(r) depth of attack	76
4.4.4.3	FSW HAZ with Hot FSP(r) depth of attack	78

Chapter 5 – Discussion **83**

5.1	Base material	83
5.2	Friction-stir weld	84
5.2.1	Nugget	84
5.2.2	Thermomechanically-affected zone	85
5.2.3	Heat-affected zone	86

CONTENTS

5.3	Friction-surface processing	87
5.4	Effect of FSP on the corrosion behaviour of FSW	89

Chapter 6 – Conclusions **91**

Chapter 7 – References **92**

Chapter 1 - Introduction

Aluminium-lithium alloys have been an attractive material firstly for use in structural applications in Germany in the 1920's, with the alloys 2020 (Al-Li-Cu) and 01420 (Al-Mg-Li), and later in the aerospace industry from the mid-1960's [1]. Second generation Al-Li alloys including AA2090, AA2080, and AA2091 showed improved mechanical properties compared with the original AA2020 alloy, but showed anisotropy of mechanical properties and a low stress-corrosion threshold [1]. The latest, third generation Al-Li alloys, developed primarily for military and aerospace applications, include AA2194, AA2096, AA2099, AA2196, AA2198, and AA2050, and are all part of the Al-Cu-Li-(Mg)-(Ag)-Zr system. Al-Li alloys are an ideal candidate for use in the aerospace industry as extremely high weight savings can be achieved through reduced alloy density, without the sacrifice of strength or corrosion resistance, or the high cost associated with novel composite structures.

Friction-stir welding (FSW) is a technique that uses rotational friction and mechanical stirring to join two pieces of material together [2]. This novel technology is one of the first to successfully join the notoriously difficult to weld 7xxx and 2xxx series alloys, producing quick, energy efficient, virtually defect-free welds [3]. FSW can add to the significant weight savings in aerospace structures by producing welds that do not require consumable filler or mechanical fastening. Due to the thermal input and mechanical deformation during FSW, a change in microstructure is created which, depending upon processing parameters can lead to increased corrosion susceptibility, particularly of ICG attack in the highly plastically deformed material in the centre of the weld, and of exfoliation corrosion where the weld meets the base material in Al-Li-Cu alloys.

FSW has recently been modified to create friction-surface processing (FSP) [3]. Using similar techniques to FSW, FSP uses a shorter rotating tool piece that does not penetrate as

deep, with a series of overlapping passes to create a region of processed material across the surface of the alloy. As with FSW, processing parameters and tool piece designs can be changed to alter the depth and microstructure of the processed material, which can be used to produce desired mechanical and corrosion properties.

Chapter 2 - Literature Review

2.1 – Al-Li Introduction

Lithium is an ideal alloying element for aluminium due to its high solid solubility (up to 4%) and, because of its low density (0.54g cm^{-3}) can give an overall alloy density reduction of 3% for every 1% addition of lithium. A further benefit of lithium as an alloying element is an increase in Young's modulus of 6% for every 1% added [4]. Both binary and complex Al-Li alloys are responsive to age hardening treatments, with the precipitation of strengthening phase. With the use of heat treatment and perfected alloy compositions, the third generation Al-Li alloys exhibit very low-density and high-stiffness making them ideal materials for use in aircraft structures [5].

The alloy used in this study is AA2050-T851 (Al-3.49Cu-0.83Li-0.43Mn-0.36Mg-0.35Ag %wt), a heat treatable alloy which has been solution heat treated, cold worked (stretched 1.5-3.5%), and artificially aged (155°C for 18hr) prior to FSW (friction-stir welding) and FSP (friction surface processing).

2.2 – Metallurgy of Al-Li-X alloys

The Al-Li equilibrium phase diagram consists of a eutectic diagram between a face-centered cubic Al-Li solid solution and body-centered cubic δ (AlLi) [6]. The precipitation sequence in the decomposition of the supersaturated solid solution for binary Al-Li alloys was shown to be [7]:

Supersaturated solid solution (SSSS) $\rightarrow$ δ' (Al_3Li) $\rightarrow$ δ (AlLi)

However binary Al-Li alloys are rarely used in industry as once heat treated often suffer from low ductility and toughness, due to δ' precipitates being easily sheared by dislocations moving through the matrix. Because of this, Al-Li alloys are readily alloyed with other solute elements in order to form additional strengthening precipitates and dispersoids which control recrystallization growth size [4]. These additional elements often include Cu, Mg, Ag, Mn, and Zr.

Age hardening is a process of nucleation and growth of precipitates that that is carried out to optimise the mechanical properties of alloys. The typical heat treatment process for aluminium alloys is as follows:

- High temperature solution treatment – dissolving the alloying elements to obtain a single phase
- Quenching – to create a supersaturated solid solution (SSSS)
- Ageing heat treatment – to decompose the SSSS forming precipitates that block the motion of dislocations in the alloy matrix.

The decomposition of the SSSS can itself comprise of a number of stages, where Guinier-Preston (GP) zones, intermediate precipitates, and eventually equilibrium phases can be formed.

The ageing process is ultimately characterised by the alloy's hardness, which will peak at a specific temperature and time combination. An alloy that is heat treated for times and temperatures prior to this peak considered under-aged, whilst treatments beyond the peak hardness can be described as over-aged, whereby the hardness begins to fall. The sub-optimal hardness seen in underaged material is attributed to strengthening precipitates being too small

and thus easily sheared by moving dislocations, while the subsequent decrease in hardness once the maximum is reached is due to the strengthening precipitates becoming too large and too widely dispersed, allowing dislocations to pass round them in a bowing action.

The decomposition of the SSSS and formation of precipitate particles can be very complex and is dependent upon the alloying system. Figure 2.1 is a schematic diagram of the possible precipitate phases in the Al-Li-X system, while Table 2.1 lists the possible precipitates and stoichiometrys possible in Al-Li-Cu alloys.

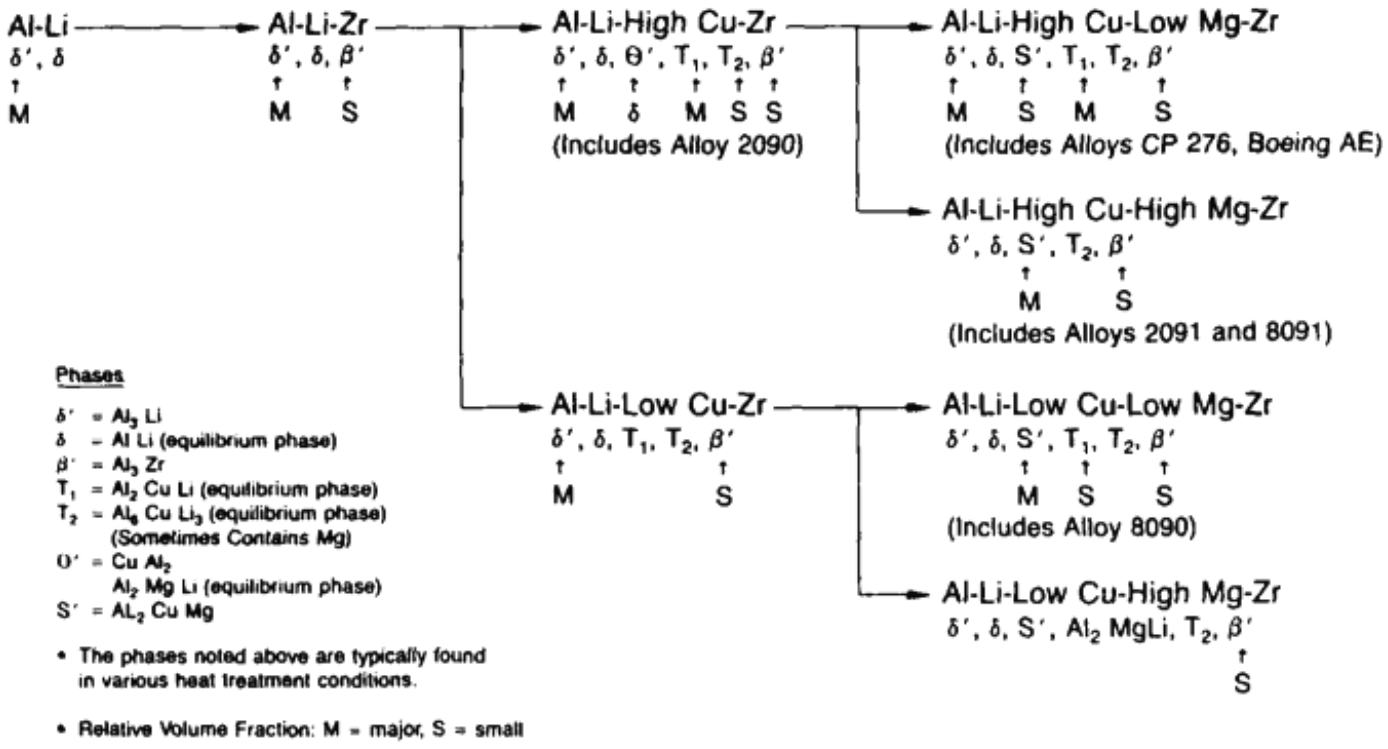

Figure 2.1 – A schematic diagram of the precipitate phases in the Al-Li-X system [8]

Table 2.1 – A table showing common possible precipitates found in Al-Li-Cu alloys with their associated stoichiometry [8]

Precipitate	Stoichiometry
δ	AlLi
δ'	Al_3Li
δ''	-
θ	Al_2Cu
θ'	Al_2Cu
θ''	Al_2Cu
T_1	Al_2CuLi
T_2	Al_5Li_2Cu
T_B	$Al_{7.5}LiCu_4$
β	Al_3Zr

2.2.1 – Al-Li-Cu System

Copper reduces the solid solubility of lithium so that precipitation of δ' is enhanced, as well as aiding in the formation of Guinier-Preston (GP) zones and θ' precipitates [7]. As Al-Cu-Li alloys such as AA2090 were developed they moved towards lower Cu contents and higher Cu:Li ratios. AA2090 is not only strengthened by δ' (Al_2Cu) precipitates but also by the hexagonal phase T_1 (Al_2CuLi) which precipitates as thin platelets on the {111} planes.

The precipitation sequence for the Al-Cu-Li system is [7]:

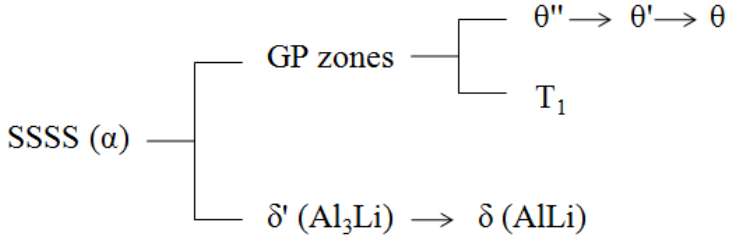

In Al-Cu-Li alloys containing low Li contents (<0.6%) the non-shearable θ (Al_2Cu) precipitate are predominantly present, while for medium Li containing alloys (<1.4-1.5%) the main strengthening phase is T_1 (Al_2CuLi) [9]. Promoted by Cu content, the T_1 precipitate is aided in its nucleation and growth by the addition of Mg and Ag. In high Li containing alloys (>1.4-1.5%), the main strengthening phase is still T_1, however δ' (Al_3Li), produced via artificial ageing has been found to significantly contribute to strength [10].

2.2.2 – Al-Li-Cu-Mg System

The addition of magnesium to the Al-Li-Cu system reduces the solubility of lithium in aluminium [10]. The heat treatment process on Al-Li-Cu-Mg alloys including AA2091, AA8090, and AA8091 has been found to lead to the co-precipitation of the semi-coherent phases T_1 (Al_2CuLi) and S' (Al_2CuMg), as well as the coherent δ' (Al_2Cu) [7]. The nucleation of both T_1 and S' are difficult, thus these alloys are usually used in the T8 temper (cold worked before ageing) [4].

2.2.3 – Al-Li-Cu-Mg-Ag-Zr System

Developed through preliminary trials using Al-Cu-Mg-Ag alloys with progressive addition of lithium content up to 2.5% and ageing at 200°C carried out by Polmear [4], an alloy with 1% lithium content showed optimum age hardening levels. From this alloy, Weldalite 049 (Al-6.3Cu-1.3Li-0.4Mg-0.4Ag-0.18Zr), was developed. It was a breakthrough alloy produced in the US that can displayed tensile strengths of up to 700MPa when in the T6 and T8 tempers, making it one of the first ultra-high strength aluminium alloy. The high strength was attributed to homogenously distributed fine T_1 phase [11], as well as θ' and S',

where by the addition of the alloying elements Ag, Mg, and Zr aid in providing low-energy nucleation sites for T_1 precipitation [10, 12].

Other studies into Al-Li-Cu-Mg-Ag-Zr alloys found that for low levels of lithium and magnesium (0-1.4%) coherent platelets of T_1 were found. Also S' and θ' were found, particularly when increasing magnesium levels as the S' volume fraction increases accordingly [12]. Also for the alloy AA2195, with a lithium content of 1% and following a heat treatment at 180°C, T_1 was observed to be the main strengthening precipitate. T_1 was shown to precipitate heterogeneously at subgrain boundaries and homogeneously throughout the matrix [10]

Zirconium, chromium, and manganese are added to inhibit recrystallisation: they form dispersoids that pin grain boundaries, limiting grain growth. Usually added at approximately 0.1-0.2% levels, zirconium precipitates coherently to form Al_3Zr, and produces alloys with better strength and fatigue properties due to the resulting finer microstructure [13].

The addition of manganese to Al-Li alloys forms $MnAl_6$ dispersoids that promote nucleation of δ' precipitates, and at 0.5 atomic% produces intermetallic phases that can drastically increase strength [14].

Silver and magnesium are commonly added to Al-Li alloys to promote Ω precipitation. A considerable improvement can be seen in the precipitation response and strength of the alloy when Ag and Mg are added to Al-Li-Cu-Zr systems, such that the addition of 1.3% Li with Ag and Mg can double the yield strength of the alloy. Further, in Al-Cu-Li-Mg-Ag-Zr alloys such as AA2050, the presence of Mg promotes T_1 precipitation and increases GP zone formation whilst the addition of Ag also produces and promotes the lengthening of T_1 and θ' precipitates [10].

2.3 – Effect of Ageing Conditions

A number of studies have been carried out to determine the hardness response to artificial ageing treatment in Al-Li-Cu-X alloys [11, 12, 15, 16]. Peak ageing results in a great increase in hardness and tensile properties through a fine homogeneous distribution of T_1, θ', and S' precipitates. As these alloys are over-aged, T_1 becomes the only strengthening phase as θ' and S' are dissolved [12]. It is common for Al-Cu-Li-Mg-Ag-Zr alloys to be manufactured in the T8 temper, which involves prior cold working to increase the dislocation density before artificial ageing. This is to ensure effective T_1 precipitation occurs, which is difficult to nucleate. Stretching prior to heat treatment has been shown to achieve an increase in tensile strength of up to 25%, 5 times faster, through a vastly increased volume fraction of T_1 precipitates in Al-Li-Cu-Zr alloys [17].

Time-Temperature-Precipitation diagrams and hardness variations as a function of heat-treatment conditions were determined for Al-Li alloy AA2195, with prior 3% stretching, by Chen and Bhat [15], as shown in Figure 2.2. It shows that at approximately between 150-320°C, T_1 is the major precipitate that forms preferentially at subgrain boundaries. At temperatures greater than 320°C, θ and θ’ become the predominant precipitates that form both in the matrix and at subgrain boundaries. It also shows that severe over ageing at temperatures above 320°C leads to the precipitation of T_B phase.

The effect of hardness variation with artificial ageing time and temperature for AA2195 is shown in Figure 2.3. It can be seen that the most effective temperature range for peak ageing is approximately 300-450°F (150-230°C), caused by the precipitation of T_1 phase. At higher temperatures 600-800°F (315-425°C), severe over ageing occurs causing θ and θ' precipitates to coarsen rapidly, with a decrease in hardness from the onset.

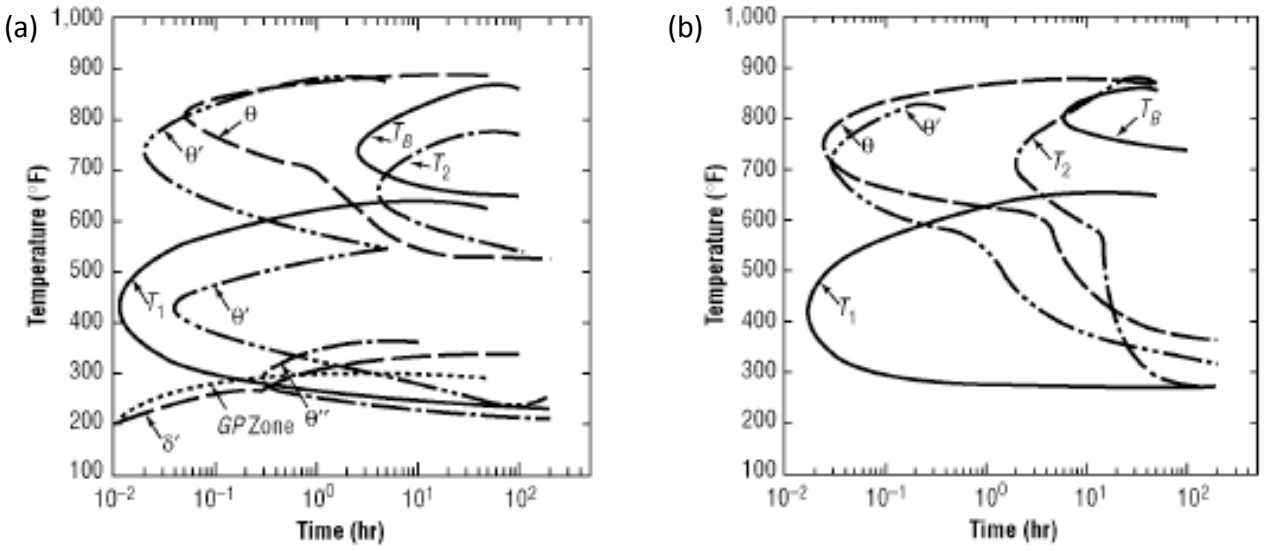

Figure 2.2 – Time-temperature-precipitation diagrams for AA2195 3% stretched and solution heat treated at 510°C for 1h in (a) the matrix, and (b) at subgrain boundaries [15]

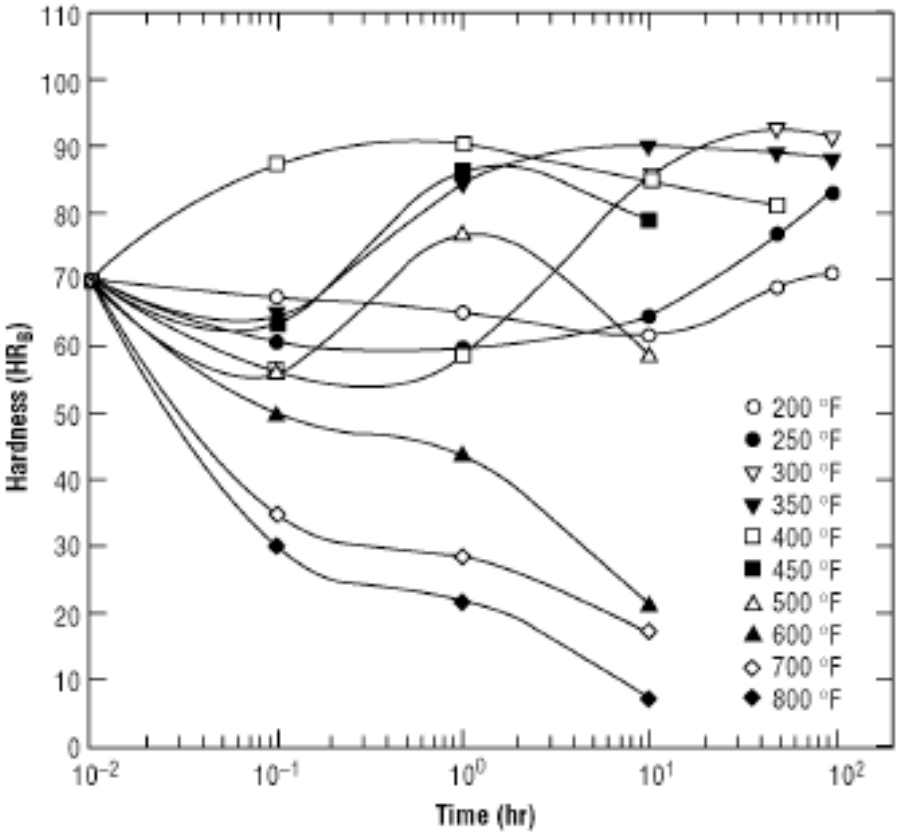

Figure 2.3 – Hardness variations as a function of heat-treatment conditions for AA2195 3% stretched and solution heat treated at 510°C for 1h [15]

2.4 – Corrosion Introduction

Metallic corrosion takes place in wet environments when the chemical or electrochemical reaction between a metal and the surrounding environment results in the oxidation of the metal. For corrosion to occur, electrons are produced by the anodic oxidation of the metal must be consumed in a cathodic reaction. These two processes can take place on different parts of a metal structure providing that there is a conducting path for the electrons between the two, and a continuous electrolyte path for ion transport.

2.4.1– Corrosion of Aluminium

Aluminium is highly reactive, with a negative standard electrode potential of -1660mV, and is therefore unstable in the presence of water. However aluminium reacts quickly with the oxygen in air or water to form a protective oxide film (alumina, Al_2O_3) that is stable in pH range 4-9 and prevents corrosion of the metal.

In aqueous solutions, the oxide film is formed during the reaction:

Eq. 2.1 **Oxidation Reaction:** $2Al_{(s)} + 3H_2O_{(l)} \rightarrow Al_2O_{3(s)} + 6H^+_{(aq)} + 6e^-$

This thickness of the oxide layer can be between 1-10nm [18], and the speed at which it grows is temperature and pH dependent [4]. The oxide layer forms within 1 ms in aqueous environments and is protective as it is resistant to dissolution in neutral environments, and blocks the cathodic reaction as it is an insulator.

Although surface oxide layer of aluminium acts as an efficient insulator preventing electron transfer to the surface, commercial alloys contain intermetallic particles that have

thinner and more conducting oxide layers allowing electrons to pass through, so that anodic and cathodic reactions can take place [18, 19].

Anodic Dissolution

Anodic active dissolution or oxidation is the loss of electrons from an Al atom to leave an Al ion plus electrons. This reaction is given below:

Eq. 2.2 **Anodic Dissolution:** $Al \rightarrow Al^{3+} + 3e^-$

In order for the charge balance to be maintained, the electrons created must be used up in a cathodic reduction reaction.

Cathodic Reduction

The main cathodic reactions involve reduction of oxygen or water as shown in the reactions below depending on the environmental conditions:

Eq 2.3 **Cathodic Oxygen Reduction:** $O_{2(g)} + 2H_2O_{(l)} + 4e- \rightarrow 4OH^-_{(aq)}$ (Neutral Conditions)

Eq 2.4 **Cathodic Water Reduction:** $2H_2O_{(l)} + 2e^- \rightarrow 2OH^-_{(aq)} + H_{2(g)}$ (Neutral Conditions)

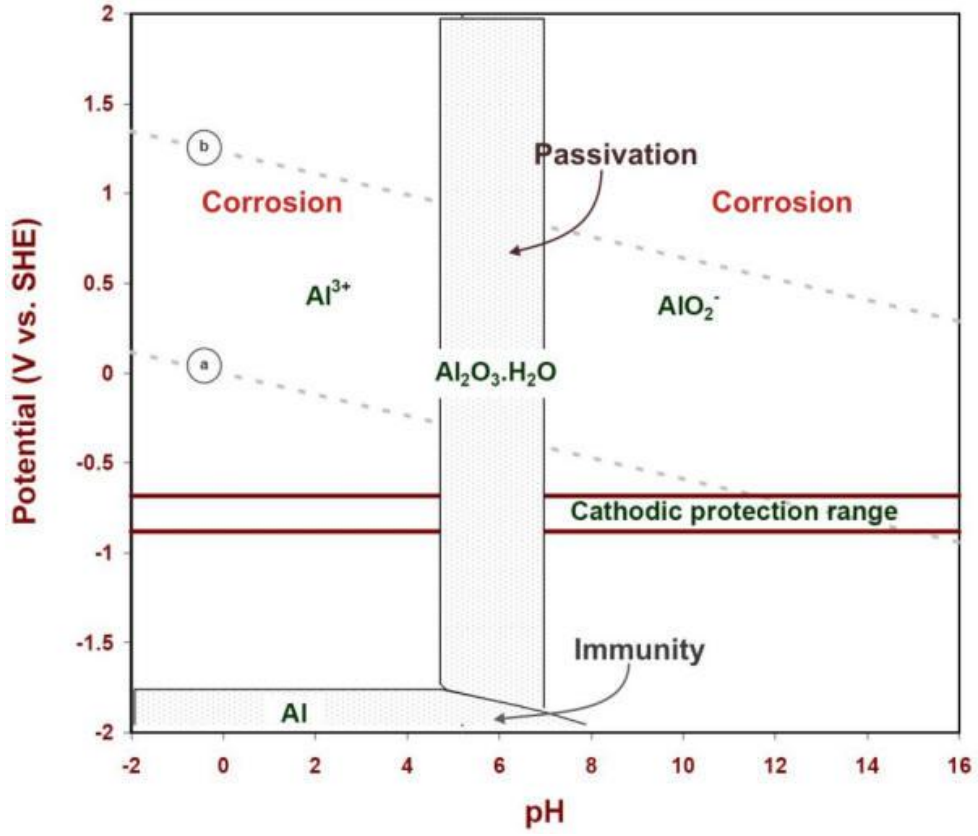

Figure 2.4 – Pourbaix diagram of aluminium in the presence of water at 25°C, showing regions of immunity, passivation and corrosion [20]

Under neutral pH conditions the oxide layer is a good insulator in preventing electrons from reaching the surface preventing dissolution. However at highly acidic and highly alkaline pH values aluminium's passive film becomes unstable and dissolves to leave the bare untreated metal so that active dissolution can take as indicated above in Equation 2.2. Figure 2.4 is a potential/pH, Pourbaix diagram which shows the theoretical regions of immunity, passivity, and corrosion as potential and pH change, whereby lines a) and b) indicate the lower and upper limits of corrosion with oxygen reduction.

The Al^{3+} ions generated at the anode react with water (hydrolysis) to produce local acidity:

Eq 2.5 **Hydrolysis:** $Al^{3+}_{(aq)} + H_2O_{(l)} \rightarrow AlOH^{2+}_{(aq)} + H^{+}_{(aq)}$

Aluminium can also undergo active dissolution in alkaline conditions:

Eq 2.6 **Alkaline Dissolution:** $Al_{(s)} + 4OH^{-}_{(aq)} \rightarrow Al(OH)_4^{-}{}_{(aq)} + 3e^{-}$

Localised corrosion can take a number of forms however is essentially promoted through the same principle; Firstly the passive film becomes damaged or impaired allowing dissolution to take place. Secondly dissolution products (Al^{3+} ions) react with water, creating H^{+} ions and leading to an increasingly acidic environment. Finally the acidic environment increases the rate at which dissolution takes place because it further prevents the passive oxide layer from reforming, thus corrosion continues to worsen.

2.4.2 – Corrosion Mechanisms in Aluminium

There are four main types of localised corrosion that affect aluminium in aqueous environments: pitting corrosion, intergranular corrosion, exfoliation corrosion and intragranular corrosion, whereby the mode of corrosion that takes place depends strongly on the alloy, its processing history and its environmental conditions.

Pitting can be a severe form of localised corrosion and is the development of cavities in the surface of the metal. There are two steps in the pitting mechanism, firstly pit initiation, followed by pit propagation. Pitting is often initiated by surface defects or intermetallic particles at the surface and the presence of chlorides which damage the oxide layer [21]. Although barely visible from surface observations, pits can often grow unseen beneath the surface of the metal for some time before blistering. Pit propagation does not occur in all

initiated pits, however those that do follow the series of steps illustrated in Figure 2.5, which can lead to severe pitting as shown in Figure 2.6.

- The damaged oxide layer leads to anodic dissolution of Al at the base of the pit, where electrons are transported to the surface and used in cathodic reactions.
- Al^{3+} ions are used in hydrolysis reactions leading to acidification within the pit, preventing formation of an oxide film within the pit.
- Chloride ions (Cl^-) are drawn into the pit to balance the positive charge generated by anodic reactions, producing a more aggressive environment preventing repassivation of the oxide layer so Al dissolution continues.

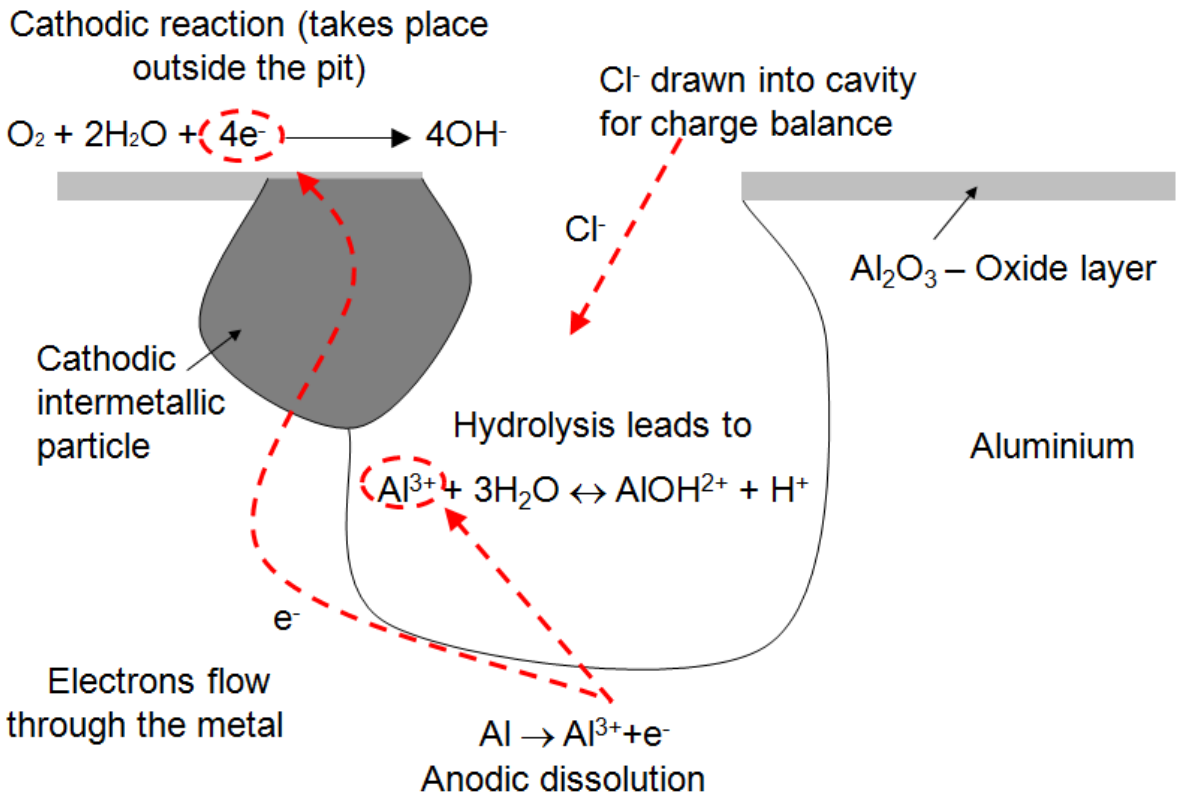

Figure 2.5 – A schematic diagram of the pitting process in aluminium due to the presence of an intermetallic particle at the surface

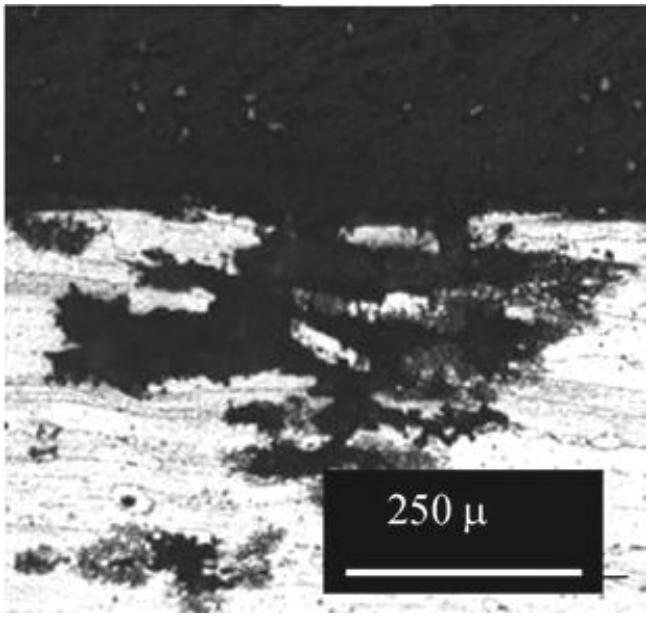

Figure 2.6 – An example of severe pitting attack in HAZ of FSW AA7075-T651, with attack at the precipitate-free zone following immersion testing in 3.5 wt.% NaCl solution [22]

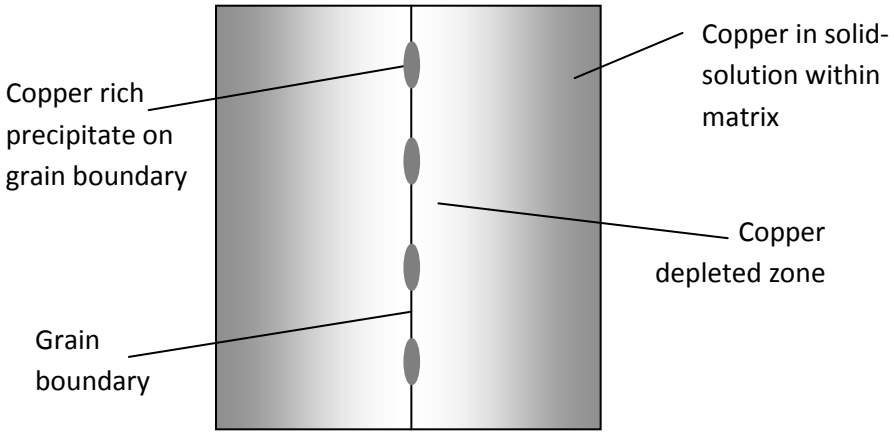

Figure 2.7 – Schematic diagram showing the role of the copper depleted zone in IGC

Intergranular corrosion (IGC), as shown in Figure 2.7 as a schematic diagram, is attack along grain boundaries or closely adjacent regions, without attack of the grain interior, and is caused by a difference in corrosion potential between grain boundary region and the grain itself. IGC can be caused by precipitation of anodically active intermetallic particles on

the grain boundaries, which corrode preferentially. It can also be caused by precipitation of more noble precipitates, particularly those containing copper, since this leads to formation of a copper depleted region adjacent to the boundary, which is more susceptible to anodic dissolution than the copper-rich matrix in the grains. Figure 2.8 illustrates the presence of a Cu depleted zone surrounding Cu rich precipitates that form along a grain boundary. The Cu depleted zone has a lower corrosion potential compared with the surrounding Al matrix and the Cu rich precipitates at the grain boundary and so goes into dissolution preferentially via microgalvanic coupling [23].

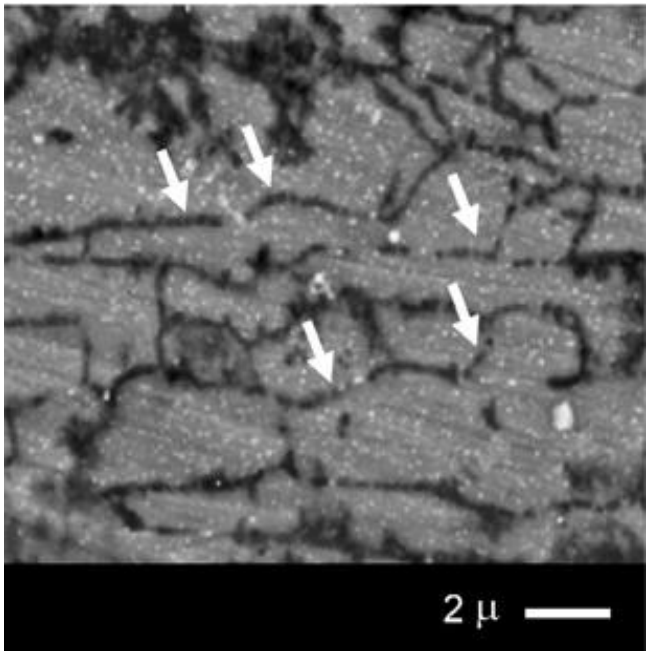

Figure 2.8 – Initial stages of IGC in the HAZ of FSW AA7075-T651, with attack at the precipitate-free zone: Note the presence of small "white" grain boundary precipitates (arrows) and attack of the precipitate-free zones (black) [22]

IGC can lead to intergranular stress corrosion cracking (IGSCC), which is the simultaneous interaction of sustained tensile stress and corrosion processes, leading to crack initiation and propagation which can result in premature brittle failure of a ductile material.

Another form of corrosion often present in aluminium alloys is intragranular corrosion. Intragranular corrosion, sometimes considered as technically a form of pitting, is when the grain interior corrodes preferentially to the grain boundary. Often a result initially of pitting at the surface, followed by intergranular corrosion through the material following grain boundaries, until a grain is reached that will corrode preferentially to the grain boundary. Intragranular susceptible grains are often those with a higher than average dislocation density, leading to either a high degree of precipitation of active precipitates, or a reduction of copper in solid solution through copper rich phases forming at sub-grain boundaries.

Exfoliation corrosion, as shown in Figure 2.9 is another form of localised corrosion that propagates along planes parallel to the rolling direction [24]. It is often as a consequence of IGC whereby the voluminous corrosion products are unable to dissolve into the environment and instead form along the paths of attack causing internal stresses leading to layers of metal being lifted from the surface [25]. It is a process that more often occurs in metal with strong directionality which creates highly elongated grains.

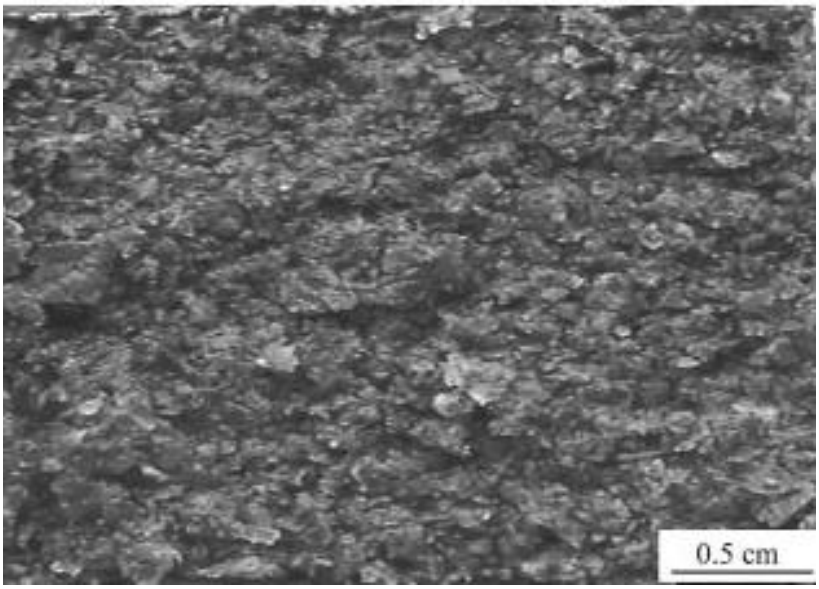

Figure 2.9 – An example of exfoliation corrosion on the surface of an Al-Li alloy following an immersion test of 96h in EXCO solution [24]

2.4.3 – Influence of alloying elements

Due its surface oxide layer, high purity aluminium is very corrosion resistant. However, it has insufficient strength for most practical applications [4], so is usually alloyed with elements such as Cu, Mg, Li, Zn, Mn, Si.

The effect of additional alloying elements is often detrimental with regards to corrosion resistance [26]. When the alloying elements are in solid solution the alloy generally remains corrosion resistant, however precipitation and the formation of second phase particles reduces the alloy's corrosion resistance by increasing the corrosion potential by providing sites for the cathodic reaction, and also sites for the initiation of localised corrosion.

These second phase intermetallic particles can form during solidification either through cellular/dendrite boundaries, or by precipitation from the SSSS, and can be anodic, inert, or cathodic to aluminium [19, 21]. Those particles that are more electrochemically active than aluminium act as localised anodes and go into dissolution themselves, while those that are less electrochemically active become net cathodes relative to the aluminium matrix where dissolution will occur [18].

2.4.4 – Corrosion of Al-Li-Cu-X alloys

The corrosion susceptibility of Al-Li-Cu-X alloys has been attributed to two fundamental metallurgical principles; firstly the precipitation of copper resulting in a lack of copper in solid solution, and secondly the presence of active Li containing precipitates.

As previously discussed, the presence of copper is one of the main causes of increased corrosion susceptibility in aluminium alloys. When copper is out of solid solution, copper rich precipitates form at high angle grain boundaries, often resulting in a copper depleted region close by [27, 28]. This copper depleted zone is not only susceptible to attack its self, but can

also create localised galvanic coupling with the surrounding matrix such that attack is further accelerated. A study has been carried out investigating the role of copper depleted zones in the corrosion of an Al-Li alloy, and Al-Li-Cu alloy AA2090, both stretched and un-stretched prior to artificial ageing treatment at 200°C [27]. It was found that in the un-stretched AA2090 the heat treatment lead to a copper depleted zone, as well as a precipitate free zone along high-angle grain boundaries, and that Cu rich precipitates formed preferentially at subgrain boundaries. This led to increased corrosion susceptibility at grain boundaries and subgrain boundaries, while in the stretched AA2090 there was no formation of a copper depleted zone, and corrosion at boundaries was not observed. In the Al-Li alloy, there was no observation of corrosion at grain boundaries or subgrain boundaries, and artificial ageing had no significant effect on the alloy's pitting potential. This strongly suggests that the presence copper depleted zones significantly increases the alloys susceptibility to corrosive attack.

The second main cause for increased corrosion susceptibility in Al-Cu-Li-X alloys is the reactivity of lithium containing active precipitates. When lithium containing precipitates, δ', T_2, and the main strengthening phase T_1 form at dislocation sites, grain boundaries, or subgrain boundaries they can promote intergranular corrosion through dissolution [29]. Polarization measurements have shown that T_1 precipitates are an active phase and have a higher potential than both the matrix and copper depleted zone in AA2090 [29, 30]. Despite a high copper content, the corrosion potential of T_1 was found to be higher than both the matrix and the copper depleted zone, such that T_1 would corrode preferentially where it led to prevalent attack at subgrain boundaries where T_1 precipitates formed when the alloy was tested in a Cl^- containing solution.

Further studies on Al-Cu-Li-Mg-Zn alloy AF/C458 found the most susceptible forms of attack were intergranular and intragranular attack, where T_1 was found to precipitate in

high concentrations at grain boundaries and sub-grain boundaries following a 57 g/l NaCl plus 10 mL/L H_2O_2 immersion test. When only non-lithium containing precipitates (θ' and T_B) were found there was no sign of either IGC or intragranular attack [31].

Electrochemical and potentiodynamic measurements have been made on simulated bulk T_1, T_2, and an aluminium alloy containing both T_1 and T_2, and it was determined that the potential of both T_1 and T_2 were more negative than α(Al) [32], as shown in Figure 2.10.

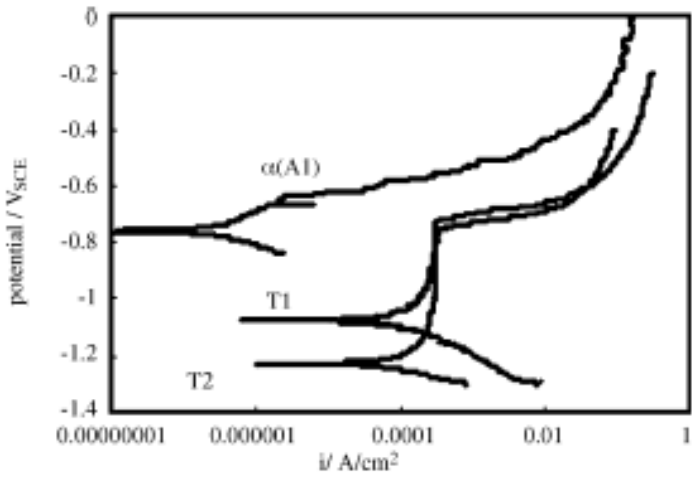

Figure 2.10 – Potentiodynamic scanning curves of (Al), T1 and T2 in 3.5% NaCl solution [32]

2.5 – Friction-Stir Welding

Friction-stir welding (FSW) is modern solid state welding technique, developed at The Welding Institute in Cambridge, UK, in 1991 [2]. The FSW concept is extremely simple, using the frictional heat and material flow produced by a non-consumable rotating tool piece to stir two pieces of metal together [33].

2.5.1 – Friction-Stir Welding Process

During FSW the rotating, non-consumable tool piece enters the material at the joint line of the two pieces of metal. The tool has a probe/pin that extends downwards from the shoulder into the material as shown in Figures 2.11 and 2.12. Once the tool has penetrated the weld joint it travels along it in the welding direction until it has successfully passed along the entire joint before being withdrawn from the metal [34].

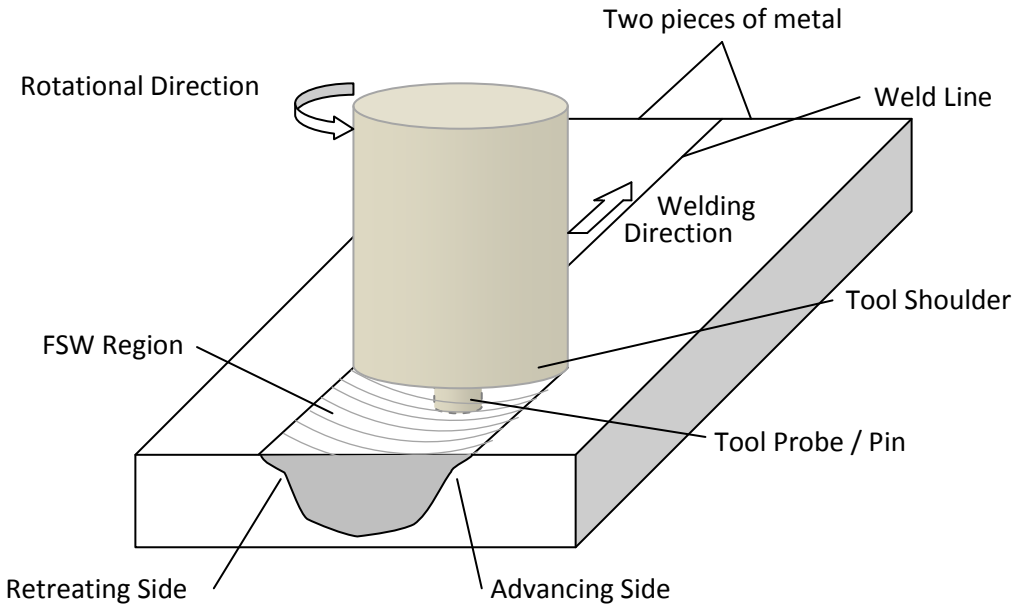

Figure 2.11 – Schematic diagram of the friction-stir welding process

It is an extremely efficient and quick process, which is why it is so attractive to industrial applications such as aerospace due to the reduced processing costs.

Frictional heat generated by the probe within the joint, and the shoulder on the surface causes the two joining metals to plasticize sufficiently for the tool to stir the two together. The shoulder acts to prevent metal from being removed from the joint. As the tool has to rotate as it travels along the joint line, an asymmetric weld is produced. This is because one side of the weld is from the 'advancing' side of the tool, while the other is from the 'retreating' side of the tool.

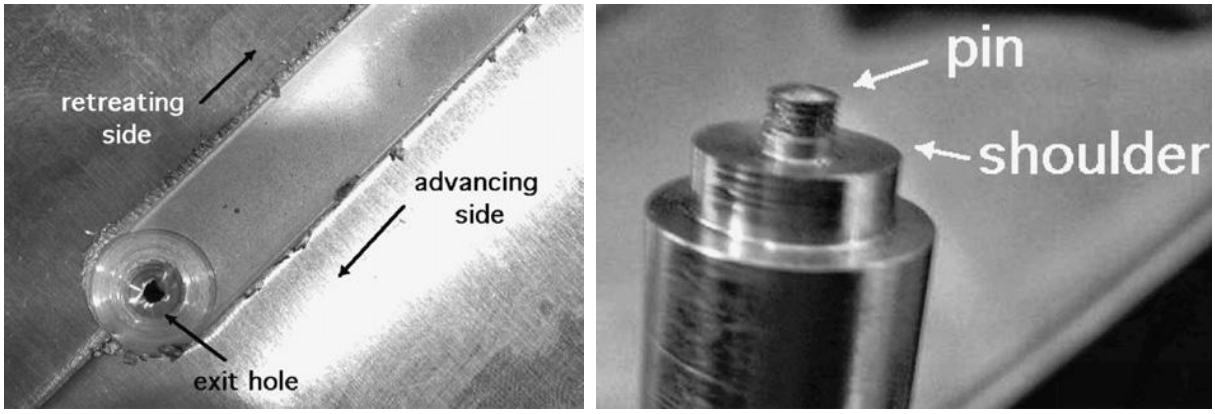

Figure 2.12 – A FSW weld between two aluminium sheets, and a tool piece with a threaded pin [35]

The advancing side of the tool always meets 'new', unaffected metal, while the retreating side of the tool always passes through metal that has already been plasticized. Figure 2.13 shows how the rotation of the tool piece defines one side as advancing and one as retreating, indicated by the traverse direction and the letter 'R' for retreating. This affects the microstructure and with it the metallurgical properties including hardness and possibly corrosion resistance.

Various conditions and parameters alter the resulting weld, including the weld materials, the size, shape, and material of the tool [36], its rotational direction (clockwise/anti-clockwise) and travelling speed, and its angle with respect to the metal surface [37, 38].

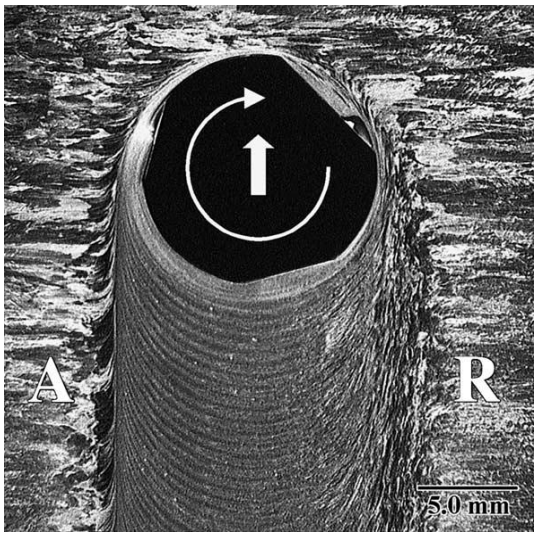

Figure 2.13 – A Plan view optical macrograph of the FSW showing the rotational and translational directions of the tool and the grain development around the tool piece. Advancing (A) and retreating (R) sides of the weld are labelled [39]

2.5.2 – Microstructure of FSW Aluminium Alloys

The cross-section of a FSW joint has three different microstructural regions that are created by the elevated temperature and mechanical motion of the tool piece. These three regions are the *heat-affected zone (HAZ)*, the *thermomechanically-affected zone (TMAZ)*, and the *nugget* (Figures 2.14 and 2.15). The base material is the surrounding metal that is entirely unaffected by the welding process.

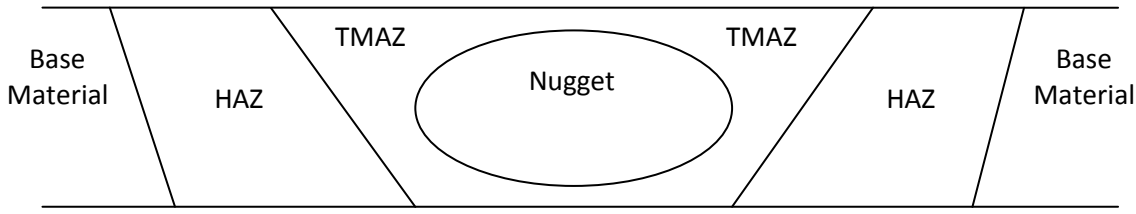

Figure 2.14 – Schematic diagram of the typical FSW regions

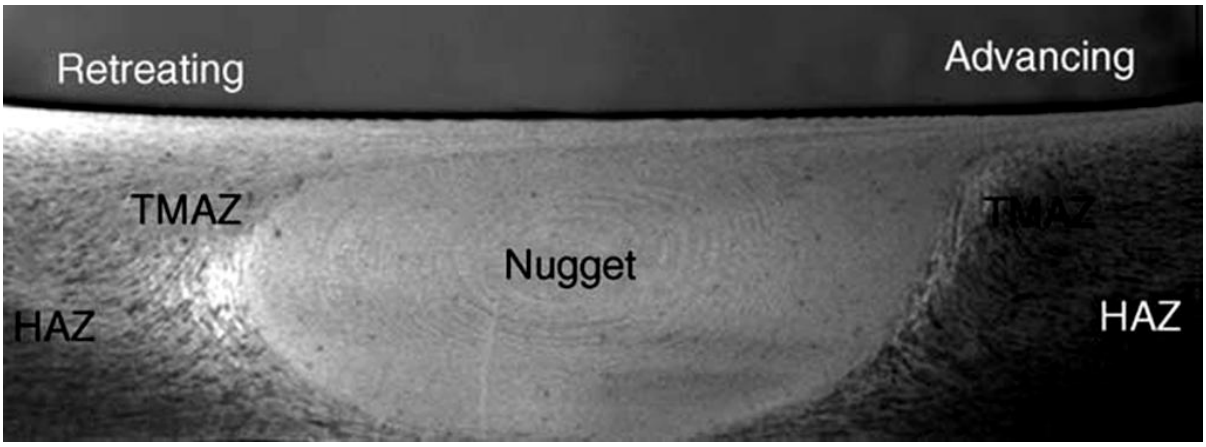

Figure 2.15 – A digital macrograph showing the typical microstructural zones formed during FSW in 7075Al-T651 [3]

2.5.2.1 – Heat-affected Zone

The heat-affected zone (HAZ) has been subjected only to heat generated by the weld without any mechanical deformation. As shown in Figures 2.14 and 2.15, it is located between the base material and TMAZ. It is similar in microstructure to the base material as the grain size remains unaffected by the FSW processing, and can only be detected by a change in hardness, which is a result of over-ageing of the hardening precipitates. There is no clear transition between the HAZ and the base material as the change in microstructure is extremely gradual, corresponding to the gradual change in temperature from the TMAZ to the base material. Typically the temperatures in 2xxx and 7xxx FSW alloys range from around 250°C close to the base material [40], between 250-300°C midway between base material and TMAZ, and between 300-350°C close to the TMAZ [15], however these are largely dependent upon weld depth and processing parameters. These temperatures do not alter the grain size or orientation, but can promote coarsening of precipitates.

The effect on precipitates across FSW Al-Li alloys have been studied including thin plate 2195-T8, where in the middle of the HAZ there was a slight decrease in T_1 length and almost complete dissolution of θ', with some θ' coarsening as shown in Figure 2.16.

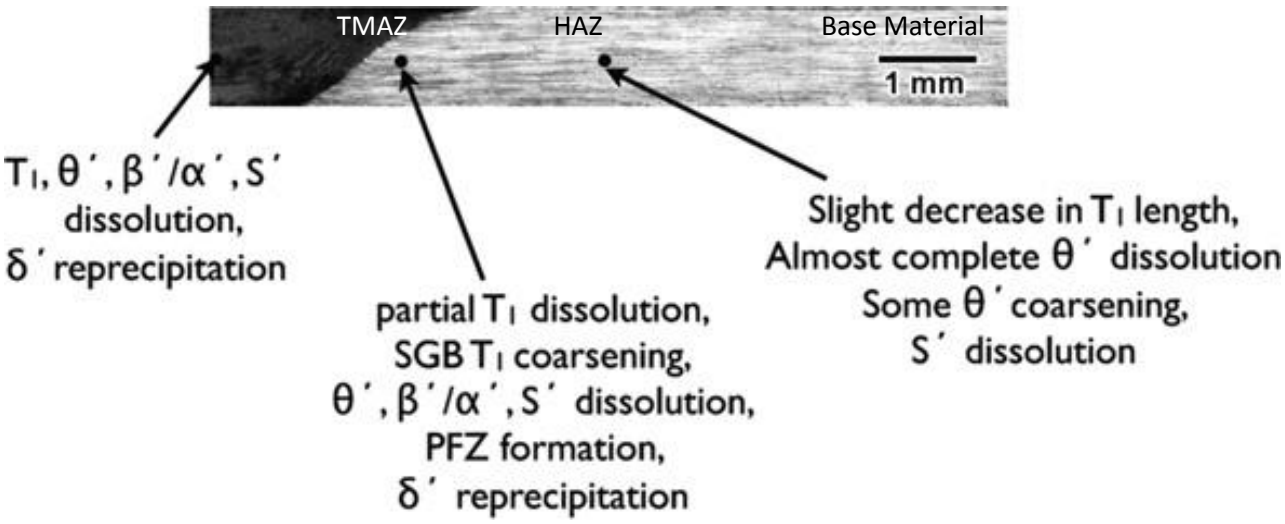

Figure 2.16 – A summary of the microstructural evolution in friction-stir welded thin-sheet 2195-T8 [40]

2.5.2.2 – Thermomechanically-affected Zone

The thermomechanically-affected zone (TMAZ) is the region between the nugget and the HAZ as shown in Figures 2.14 and 2.15. In this region, the alloy has been subjected to severe plastic deformation and heat owing to the proximity of the rotating toolpiece during welding. Full recrystallisation does not occur in this region, and the deformation of individual grains can be identified on a microscopic level, as shown in Figure 2.17. Temperatures in this region are reportedly 350-450°C [3] for typical heat-treatable aluminium alloys, however this is dependent upon weld depth and processing parameters.

Shukla and Baeslack observed partial T_1 dissolution, and coarsening of T_1 at subgrain boundaries (SGBs), as well as θ' dissolution, δ' reprecipitation, and the formation of precipitate free zones (PFZs) in the TMAZ of FSW thin-sheet AA2195-T8 [40].

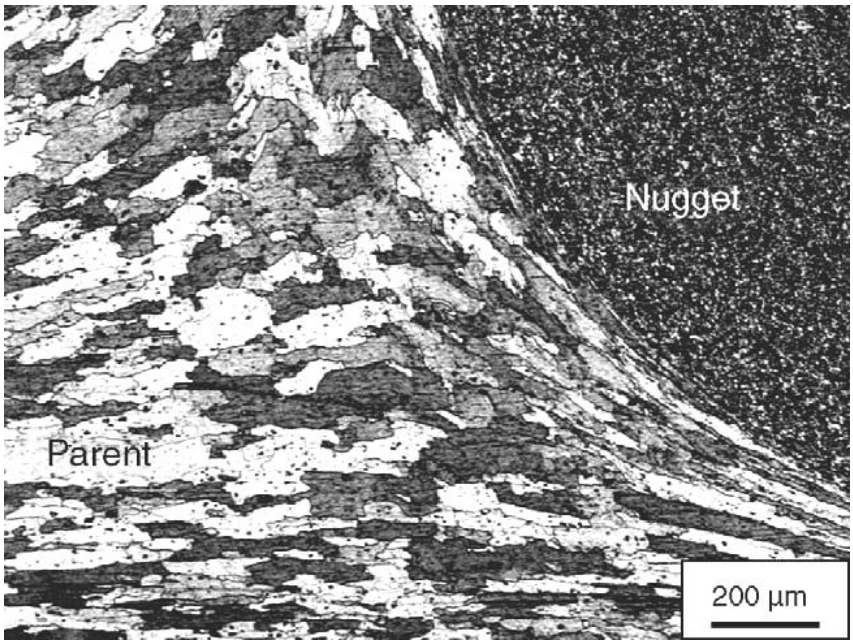

Figure 2.17 – Microstructure of base, TMAZ, and nugget in FSW AA7075 [41]

2.5.2.3 – Nugget

The nugget, as shown in Figures 2.14 and 2.15 is the central weld structure where the pin of the rotating tool piece passes directly through. This leads to a highly mechanically deformed material that can be subjected to temperatures of 400-500°C [42] causing a fine equiaxed grain structure through a mixture of simultaneous recovery and dynamic recrystallisation [35, 43]. The size of the resulting fine grains in aluminium alloys is typically 1-10 µm. However this depends heavily upon the alloy used, the processing parameters (rotational speed, traverse speed, tool design, vertical pressure, tilt angle, cooling rate), which

determine the temperatures in the stir zone [3]. Figure 2.18 shows how on average the temperature in the centre of the nugget determines the resultant grain size.

The extremely high levels of deformation in theory could act to increase the number of dislocations, whereas in reality the recovery processes that occur due to exposure to high temperatures diminishes dislocation density within the recrystallised grains. The dislocation densities of individual grains can differ greatly through the nugget, with some grains exhibiting relatively higher dislocation densities others [44, 45].

Figure 2.15 shows the typical banded striations known as “onion rings” that are visible following chemical etching. A number of studies have been carried out attempting to explain the onion ring phenomenon observed in many FSW nuggets. They are associated with distance covered, in the traversing direction, in a single rotation of the tool piece [45, 46], and have been attributed to the rotation of the tool piece and its forward motion acting to extrude the softened material from the advancing side around to the retreating side of the tool piece with each rotation [47], and to differences in intermetallic particle distribution due to enhanced quench sensitivity of particles that were fragmented by the rotating tool piece [48]. Views on the effect of grain size are differing, with some studies showing no difference in grain size [46-48], while others show significant differences [49, 50].

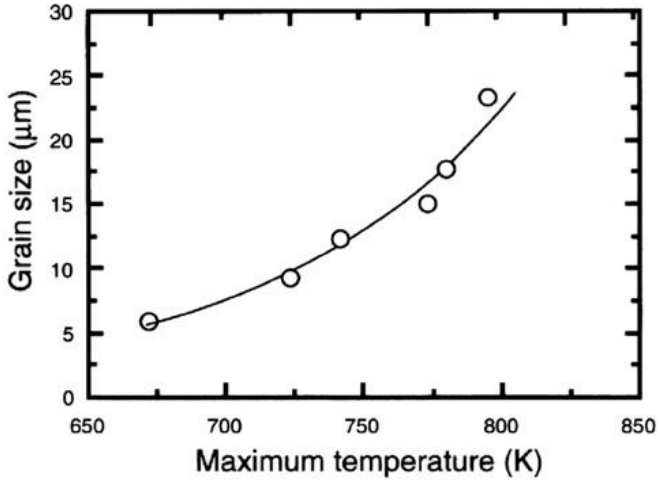

Figure 2.18 – Relationship between the grain size and maximum temperature of the welding thermal cycle [37]

2.6 – Friction-Surface Processing

Friction-surface processing (FSP) is a recent development of the well established FSW process for producing surfaces with modified microstructures [3, 51-53]. The principals are the same as FSW. However, the rotating tool piece consists of just the shoulder section, with the option of a much smaller tool probe or pin. The process is not intended to join two work pieces together, but rather to form a bulk layer of recrystallised material across the surface of the alloy or component to improve properties such as strength, and crack fatigue, and to reduce porosity, particularly in cast aluminium [54], as well as in the production of surface composites on aluminium substrates [51]. Much like FSW, FSP is affected by similar processing parameters including traverse speed, rotational speed, and the angle of the tool with respect to the material surface [55].

Previous work has been carried out on multiple FSP passes in order to create bulk fine equiaxed grain structure across the surface of aluminium alloys. Figure 2.19 shows

macroscopic and TEM cross-section images of the grain structure of AA7075 following four FSP passes, whereby superplasticity and thus considerably improved mechanical properties were achieved [56]. The maximum temperature reached in the centre of the weld zone in this study was 480°C with an average nugget grain size of 3.8 µm. Others have reported grain sizes of ~7.5 µm in AA7075-T651 following FSP with a rotation speed of 400 rpm and a traverse speed of 102 mm/min [54]. Ultra-fine-grain sizes of 0.4 to 0.7 µm have been obtained in FSP Al-4Mg-1Zr alloy using various tool pieces and under a number of different processing parameters [41].

One of the greatest attractions of FSP in producing bulk recrystallised material is in corrosion protection. Despite conflicting results on the corrosion behaviour of FSW as discussed previously, which are clearly due to differences in the processing parameters, the alloy composition, any previous or subsequent processing, it was observed that for thin plate AA2050 the most corrosion resistant FSW region was the nugget [57].

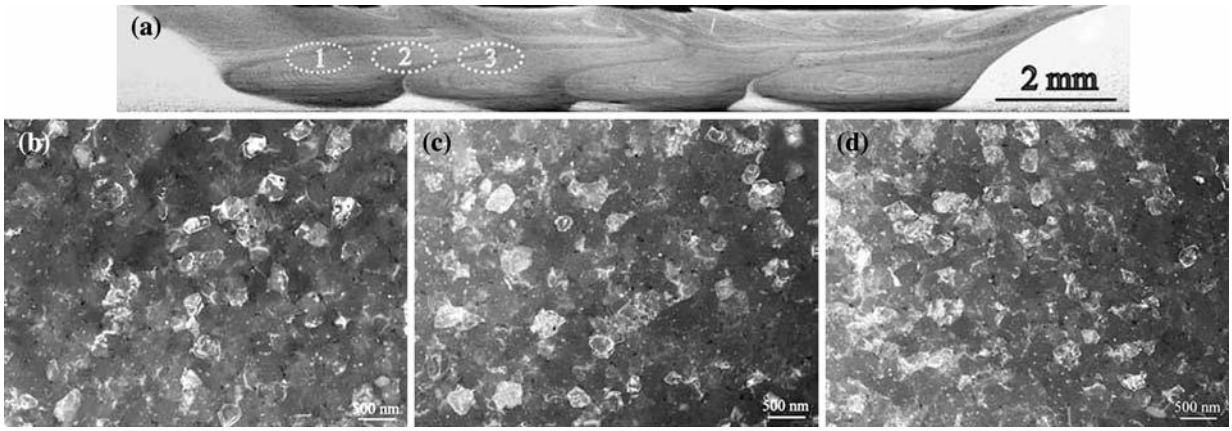

Figure 2.19 – (a) A macroscopic image of FSP AA7075 after four passes, with TEM micrographs showing the grain structures (b) through pass 1, (c) at the boundary of passes 1 and 2, and (c) through pass 2 [56]

2.7 – Microstructural Properties of FSW and FSP Al-Alloys

As previously discussed, in the case of heat treatable aluminium alloys, the determination of each FSW region is characterised by its hardness, as the heat generated through welding changes the microstructure of the material. Generally, an increase in hardness can be caused by a finer microstructure but is mainly caused by the precipitation of strengthening particles. Where as a decrease in hardness is attributed to the coarsening of the strengthening particles and their too wide dispersion leading to bowing by dislocations [58]. With regard the nugget and TMAZ regions, severe plastic deformation dramatically alters the microstructure and thus the hardness of the weld.

For most heat treatable aluminium alloys the weld region displays a reduced hardness compared with the base material. Many studies have identified a 'W' hardness profile, as shown in Figure 2.20(a), which shows the common reduction in hardness in the HAZ, compared to the base material [37]. The hardness reaches a minimum in the TMAZ, before a slight increase across the nugget region. The hardness across a weld will change, usually increasing with time as natural ageing takes place if temperatures are sufficient in the nugget to put the solute is put into solid solution [50], and can also be modified through post-weld heat treatment (PWHT) as shown in Figure 2.20(b). It can be seen that all regions, but particularly the nugget show improved hardness following PWHT of 175°C for 12 hours.

It has also been demonstrated that microstructure has an effect on the hardness on the profile of FS welds [59], where an increase in hardness follows a decrease in grain size which can also explain the increase in hardness across the nugget compared to the TMAZ.

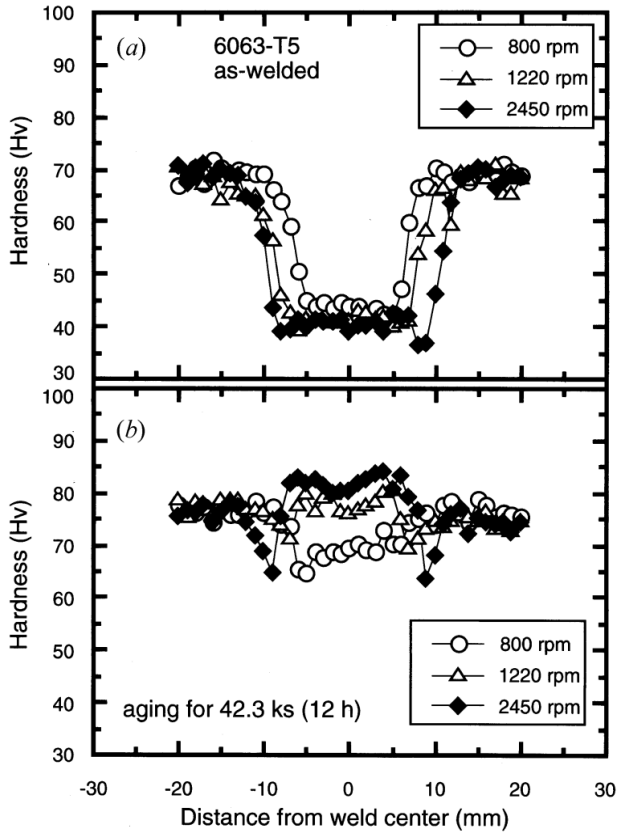

Figure 2.20 – Horizontal hardness profile of the welds of Al alloy 6063-T5 (a) in the as-welded condition and (b) in the post-weld aged condition [37]

2.8 – Corrosion Properties of FSW and FSP Al-Alloys

As previously discussed, the FSW and FSP process produces significant heat and mechanical deformation on the alloy which results in changes to the microstructure, as well as its corrosion behaviour. This change is largely determined by a change in microstructure and the size and distribution of precipitates. A number of studies have been carried assessing the effect of FSW on the corrosion behaviour of aluminium alloys most of which exhibiting different behaviours due to the differences in alloy composition and processing treatments [22, 60-69].

In AA7050, the nugget and TMAZ become susceptible to corrosion, with increasing resistance following PWHT for 25 minutes at temperature of 115-215°C [22].

In AA2024-T351, FSW leads to intergranular corrosion susceptibility in the nugget and HAZ, with specific relation to welding parameters whereby low rotation speeds lead to an increase in attack in the nugget, and high rotation speeds lead to increased attack in the HAZ due to increased anodic activity, and sensitisation at grain boundaries respectively [60].

In AA7108-T9, FSW caused increased susceptibility to intergranular corrosion in the TMAZ through an uneven distribution of $MgZn_2$ dispersoids via sensitisation of the weld [66].

In an Al-2.05Li-2.70Cu-0.6Mg-0.3Zn alloy, IGC and intragranular corrosion attack was observed in the base material, HAZ, and TMAZ, while the nugget suffered only IGC and pitting attack following FSW and a G110 immersion test. Both the nugget and HAZ were shown to suffer a great decrease in SCC resistance following the immersion test [61].

A previous study has already examined the corrosion properties of FSWs in AA2050 when subjected to various post-weld heat treatment conditions [57]. Macroscopic images of an identical 10 day 0.1M NaCl immersion test results are shown in Figure 2.21 of FS welded AA2050 immersion tested after different post-weld heat treatments (PWHT). It can be seen from Figure 2.21 that in the T-34 as welded condition, the base material is corrosion resistant; the nugget is subject to minor attack, while the TMAZ and HAZ suffer from severe pitting attack. In the T34-T8 3hr PWHT condition, the base material suffers from minor pitting attack. However, attack in the nugget, TMAZ and HAZ are all reduced compared with the as welded condition. As for the T34-T8 18hr PWHT, the base material suffers from severe pitting attack while the entire weld structure appears very resistant to pitting corrosion.

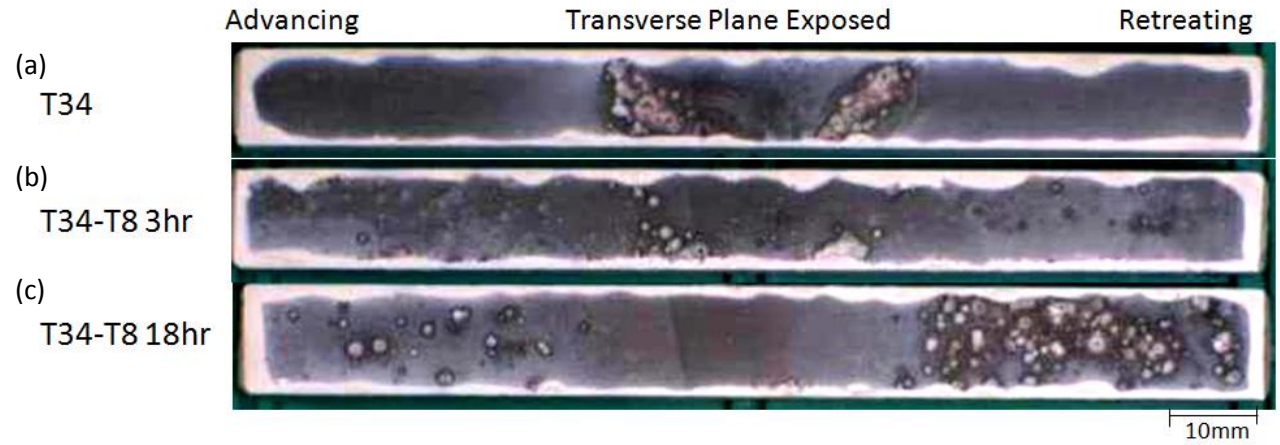

Figure 2.21 – Optical macrograph images of results from a 10 day 0.1M NaCl immersion test AA2050-T34 specimens with the corrosion product on the surface in the (a) as welded condition, (b) T34-T8 3hr PWHT condition, (c) T34-T8 18hr PWHT condition [57]

A study by Surekha *et. al*. [65] investigating FSP of AA2219 found that the rotation speed has a major influence on the corrosion behaviour, while traverse speed showed to have no effect. It was observed that at greater rotation speeds there is an increase in the dissolution of $CuAl_2$ particles, which in turn increases the corrosion resistance as there were fewer copper rich precipitates forming at grain boundaries, and thus no associated copper depletion adjacent to the grain boundaries. A significant reduction in pitting was observed at the higher rotational speeds, which lead to fewer initiation sites for IGC.

FSW in AA2050 can show susceptibility to corrosion. It has been shown that this can be mitigated by PWHT. However, owing to the difficulty of carrying this out on large structures such as airframes, it may be preferable to use FSP as an alternative method for improving the corrosion resistance by modifying the surface microstructure. In this project, the effect of FSP on the microstructure and corrosion resistance of a FSW in AA2050 will be explored. Corrosion performance and behaviour will be determined using immersion testing, and subsequent microstructural analysis. All regions including base material, each FSP, FSW,

and the FSW and FSP combined will be considered, and their corrosion behaviour will be quantified as a result of the corrosion mode (pitting, IGC, intragranular attack, or pitting with IGC), corrosion location (frequency of attack for a given area), and the depth of corrosion (the severity of attack).

Chapter 3 - Experimental Procedure

3.1 – Material Composition

An AA2050 (Al-3.49Cu-0.83Li-0.43Mn-0.36Mg-0.35Ag %wt) block in the T851 temper which has been solution heat treated, cold worked (stretched 1.5-3.5%), and artificially aged (155°C for 18hr), prior to a central FSW and two FSP (one under 'hot' parameters, and one under 'cold' parameters) running perpendicular to the FSW was supplied by Alcan, Centre de Recherches de Voreppe (CRV). The dimensions of block were 807 mm x 150 mm x 76 mm. The dimensions and locations of the FSW and FSPs are shown in Figure 3.1.

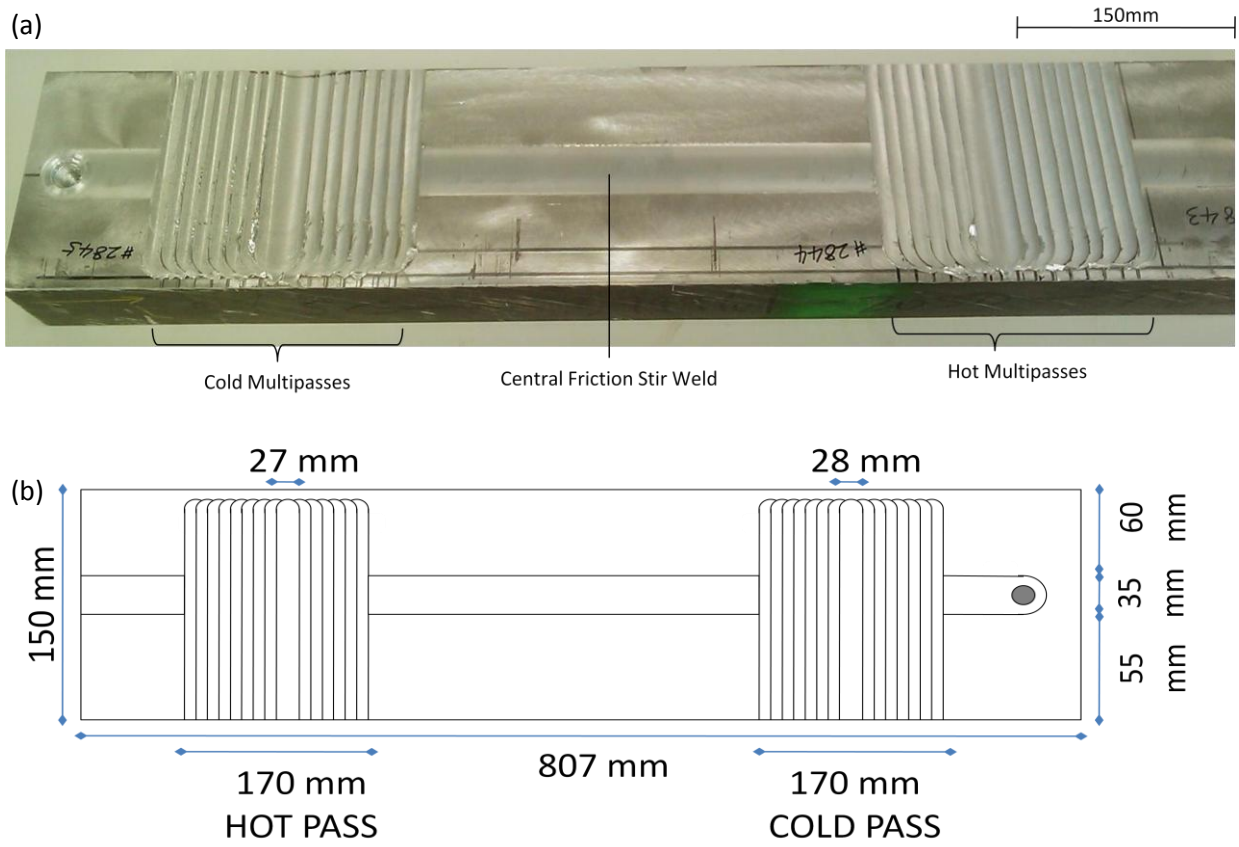

Figure 3.1 – (a) the AA2050 block with central FSW and perpendicular FSPs, and (b) schematic plan view giving dimensions

The FSW and FSPs were performed by the University of South Carolina, and the parameters of each of the processes are given in Table 3.1. Table 3.2 gives the nominal chemical composition and composition limits of AA2050.

Table 3.1 – Welding and FSP processing parameters (University of South Carolina)

Pass	Shoulder Diameter (mm)	Tool Length (mm)	Tool Details	Rotational Speed (rpm)	Travelling Speed (mm/min)	Z-Force	FSW Torque (Nm)	FSW Power (W)	Additional Notes
FSW	35.5	24.3	Threaded pin with 3 flats – 0.75" (Top) at 9° taper	220	152	15000 lbs	359.7	8220	
Hot FSP	28.5	5.0	Cylindrical threaded pin with 3 flats- 0.5" diameter	400	200	11000 lbs	115.6	4866	2.5 mm overlap from pass to pass
Cold FSP	28.5	5.0	Cylindrical threaded pin with 3 flats - 0.5" diameter	180	200	11000 lbs	215.3	4120	2.5 mm overlap from pass to pass

Table 3.2 – Chemical composition and composition limits (Alcan, Voreppe, France)

Element	AA Composition Limits (wt%)
Cu	3.2 - 3.9
Li	0.7 - 1.3
Mn	0.2 - 0.5
Mg	0.2 - 0.6
Ag	0.2 - 0.7
Zr	0.06 - 0.14
Fe	0.1
Zn	0.25
Si	0.08
Ti	0.1
Cr	0.05
Ni	0.05
Ga	0.05
V	0.05
Others	0.06 -1.14
Al	Balance

3.2 – Sample Preparation

For immersion, MASTMAASIS, and microhardness testing and microstructural analysis, cross-sections were taken perpendicular to the FSW and FSP directions, in the transverse plane through the un-treated FSW and in the longitudinal plane through the two FSPs. 2 mm were planed from the top surface of all test specimens to remove the rough processed surface. Figure 3.2 is a schematic diagram of the FSW test specimens in the transverse plane prior to immersion testing.

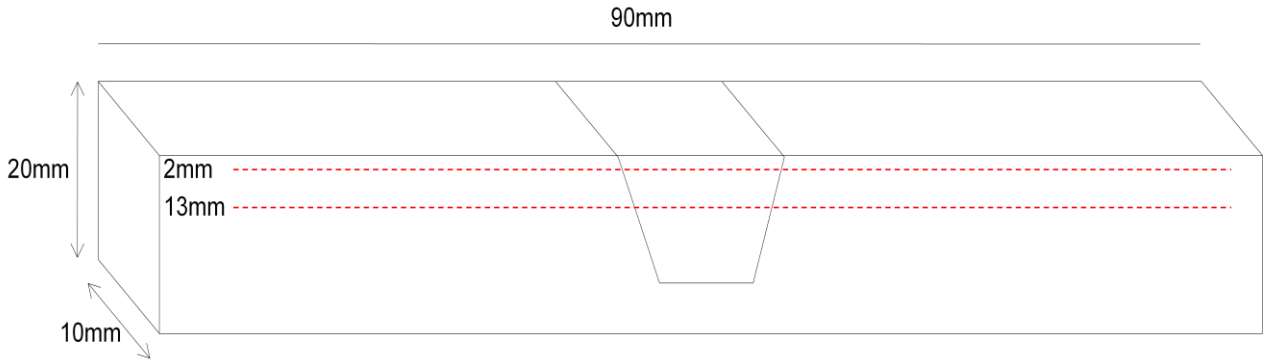

Figure 3.2 – Schematic diagram of FSW test specimens, showing depths of immersion testing at 2mm and 13mm from the surface

All samples were ground down to a 4000 grit finish by hand using successive grades of SiC grinding paper (120/240/800/1200/2500/4000), before polishing to 3 µm, and then 1 µm using Struers polishing supplies. Grinding and polishing was performed using Struers alcohol based Yellow, and Diamond Suspension lubricants respectively to avoid contact with water throughout. Before any testing, or analysis using the scanning electron microscopes (SEM), and after polishing, specimens were cleaned with ethanol using an ultrasonic cleaning bath.

3.3 – Microstructural Characterisation

Optical metallography was carried out using a Carl Zeiss optical microscope with an additional digital camera mounted on top for imaging. Polished specimens were etched using Keller's reagent for 15-20 seconds and cleaned using ethanol to produce a visible grain structure.

3.4 – Microhardness Testing

Microhardness tests were carried out using a Mitutoyo MVK-H1 hardness testing machine, with a load of 50 g. Tests were carries out at a depth of 3 mm from the surface, at 1 mm intervals along the entire cross-section of both the FSW and the FSPs. Samples were polished and etched to identify the weld regions under investigation. Further tests were carried out in the transverse direction through the middle of the centre nugget for each of the FSPs to observe any differences in the effective depth of the FSP treatments.

3.5 – Immersion Testing

10 day, 0.1 M NaCl immersion tests were performed on the FSW and FSP regions. The top surfaces were polished to 1 µm and cleaned with ethanol, while all other sides not under investigation were coated with a MacDermid 45 Stopping-Off Lacquer. The samples were left undisturbed in a naturally aerated 0.1 M NaCl solution at room temperature for 10 days.

After testing, the specimens were cleaned using ethanol and were macroscopically photographed using a digital camera, before being gently polished to remove the corrosion product. The immersed samples were then photographed again without corrosion product.

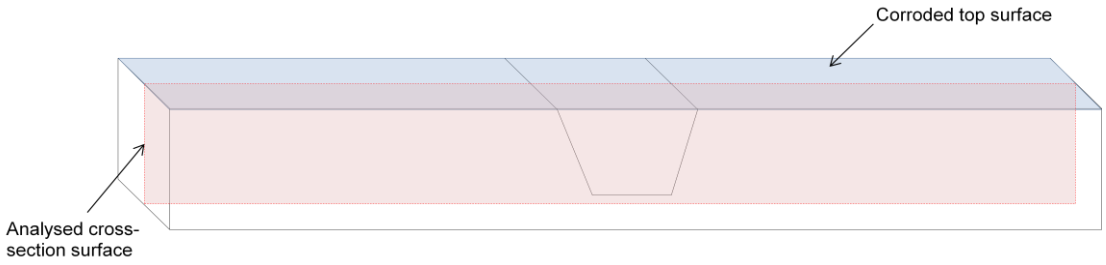

Figure 3.3 – A schematic diagram showing how the polished top surfaces were immersion tested before cross-sections were taken to determine corrosion behaviour

The immersed samples were then cut through in the transverse plane, as shown in Figure 3.3, before being cold mounted using a MetPrep Tri-Hard mounting powder, and polished to 1µm. The depth of attack through the cross-section was then quantified using a Carl Zeiss optical microscope, with a magnification of 50x. Further observations of corrosion attack were made using SEM analysis.

3.6 – MASTMAASIS Testing

MASTMAASIS (Modified ASTM Acetic Acid Salt Intermittent Spray) tests were carried out by Alcan at CRV Voreppe across the FSW and both FSPs prepared in exactly the same way as the immersion tests, with 2 mm being milled from the top surface and subsequently polished to 1 µm using non-aqueous lubricants. The MASTMAASIS was a dry bottom, accelerated seacoast exposure test. The test followed the ASTM G85 A2 standard [70]. Testing was carried out at 49°C in a NaCl 5% with a pH stabilised to pH 2.8-3 with a cyclic: 45min spray – 120min drying – 195min soak at low humidity, for a total of 750 hours.

Chapter 4 – Results

4.1 – Microstructural Characterisation

4.1.1 – Base Material Microstructure

The un-welded base material within the AA2050-T851 block consisted of a directional anisotropic grain structure, as shown in Figure 4.1. The rolling direction is clearly visible due to the alignment of pancake-like grains.

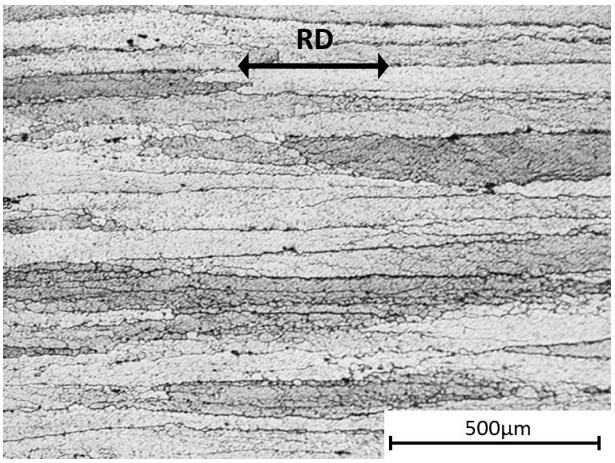

Figure 4.1 – Optical micrograph of base material in the longitudinal plane showing the rolling direction (RD)

4.1.2 – Friction-Stir Weld Microstructure

The FSW microstructural cross section was typical of that of most FS welds between similar heat-treatable aluminium alloys, consisting of a basin nugget structure, with thermomechanically-affected zones (TMAZ), and heat-affected zones (HAZ) either side. Figure 4.2 is a macroscopic image of the FSW structure where each region has been identified.

The central nugget region of the weld structure is approximately 25 mm deep, and 27 mm wide at the surface, and 12 mm wide at its deepest point. The grain structure in the

nugget consists of fine recrystallised, equiaxed grains, which are smallest (1-2 μm) at the surface and grow larger towards the bottom of the nugget (5-15 μm), as can be seen in Figure 4.3. Striations or "onion rings" can be seen through the centre of the nugget, and as a result of variations in the heat transfer and mechanical stirring of the FSW process.

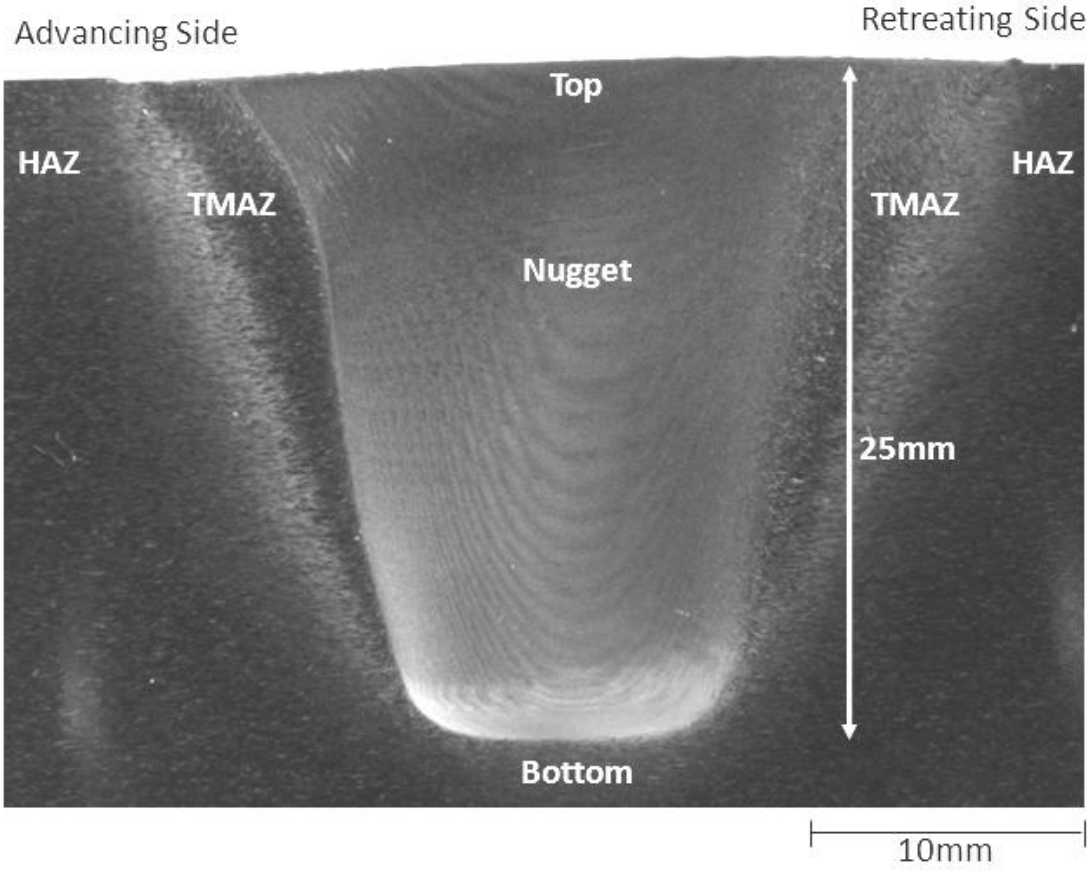

Figure 4.2 – Macrographic image of the cross-section of the friction-stir weld in the transverse plane (end grain) etched using Keller's reagent to reveal the grain structure

The TMAZ is the transitional interface between the nugget and HAZ. The grains within the TMAZ are not recrystallised, but are highly deformed in an upwards direction, parallel to the direction of rotation of the tool piece. The TMAZ is approximately 3 mm wide on the advancing side and 4 mm wide on the retreating side of the weld. However, the transition is much sharper on the advancing side than on the retreating side.

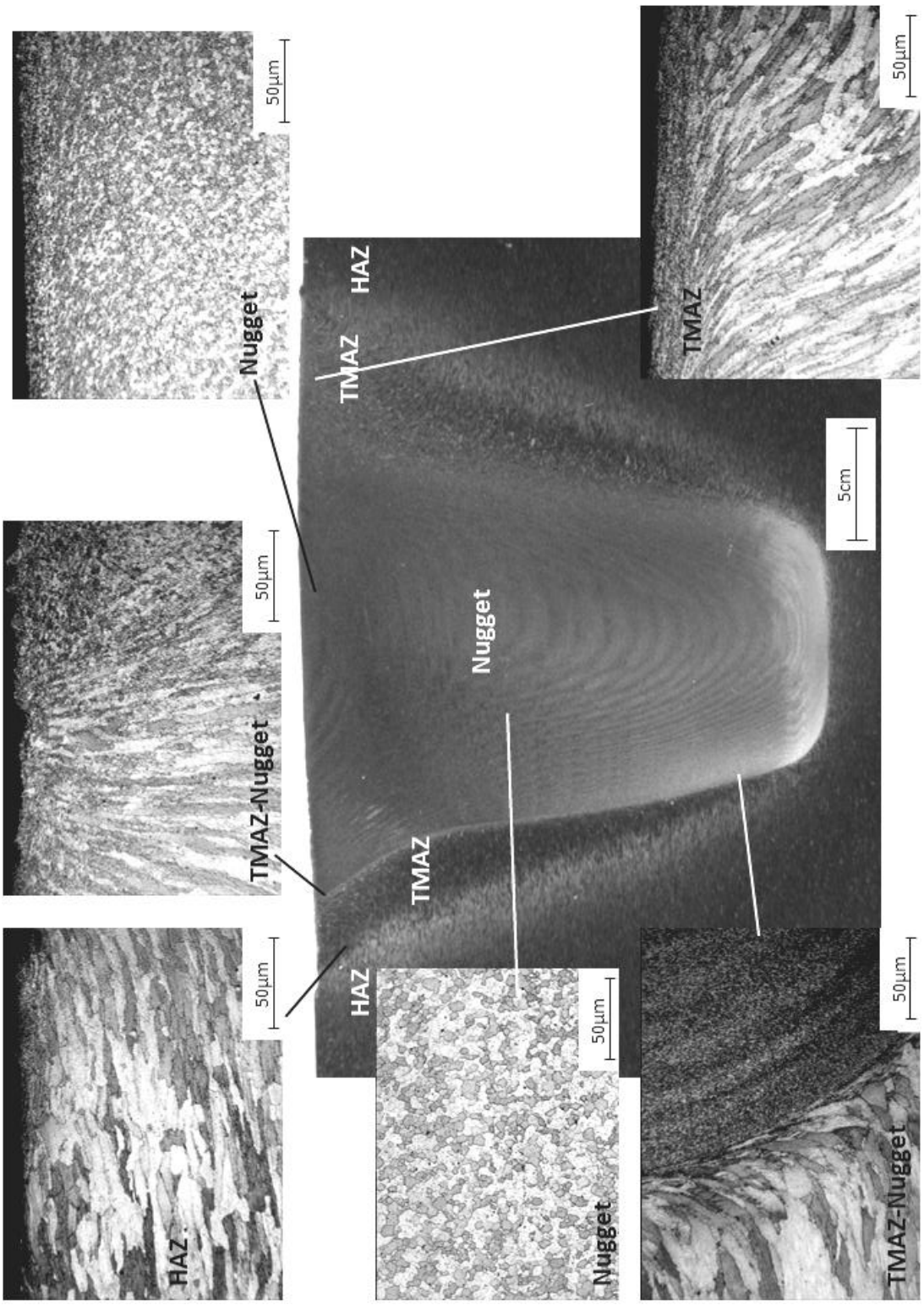

Figure 4.3 – Macrographic image of the friction-stir weld, with micrographic images of the grain structure in each region taken from a cross-section of the transverse plane

This is characteristic of Al-alloy FSWs, and is due to the localised heat differences as the tool piece cuts through new material on the advancing side, and passes through already plasticized material on the retreating side; this transition is particularly apparent towards the bottom of the nugget. The boundary on the retreating side is not as clearly defined as the advancing side, and shows a more gradual transition from TMAZ to HAZ.

The HAZ on both advancing and retreating sides shows grain sizes characteristic of that in the base material, which are elongated in the rolling direction.

4.1.3 – FSP Microstructure

The microstructures of the friction surface processing passes were similar for both "hot" and "cold" parameters (see Table 3.1). Both had an average nugget depth of 6-7 mm, as shown in Figure 4.4. Both show the characteristic FSW regions of nugget, TMAZ, and HAZ. However, some structures of the previous pass are effectively erased as the next overlapping pass takes place. Therefore all of the passes to the advancing side of the central pass consist of only advancing boundaries (TMAZa) over existing nuggets, and all of the passes to the retreating side of the central pass consist of retreating boundaries (TMAZr) over the existing nuggets. Differences between hot and cold FSPs include a "flatter" more even nugget base, or transition between nuggets and base material in the cold FSP, as can be seen in Figure 4.5, as well as a straighter transition line at the edges of each pass in the cold FSP, giving a more angular appearance compared to the hot FSP. There are also more pronounced and visible striations through the weld nugget in the cold FSP, and due to faster travel speed of the tool piece, and much more surface distortion across the top of the passes.

The grain structure throughout the FSPs is consistent with that of the FSW, with the nugget consisting of fine equiaxed grains which are smallest at the surface and become larger

towards the bottom of the nugget. The grain structure of the TMAZ on advancing and retreating sides also follows trend of the FSW, with the nugget-TMAZ transition being much sharper on the advancing side, and more gradual on the retreating side. The HAZ cannot be identified visually on a macroscopic level because, as with the FSW, the grain size is not affected. Also with subsequent passes effectively erasing any previous mechanical or heat treatment, the HAZ is only found beyond the two outer passes where the grain structures resemble the base material. The outer passes (Passes "A" and "O" shown in Figure 4.5) showing the HAZa on the advancing side and HAZr on the retreating side of the passes resembled the microstructure of the base material with no mechanical deformation.

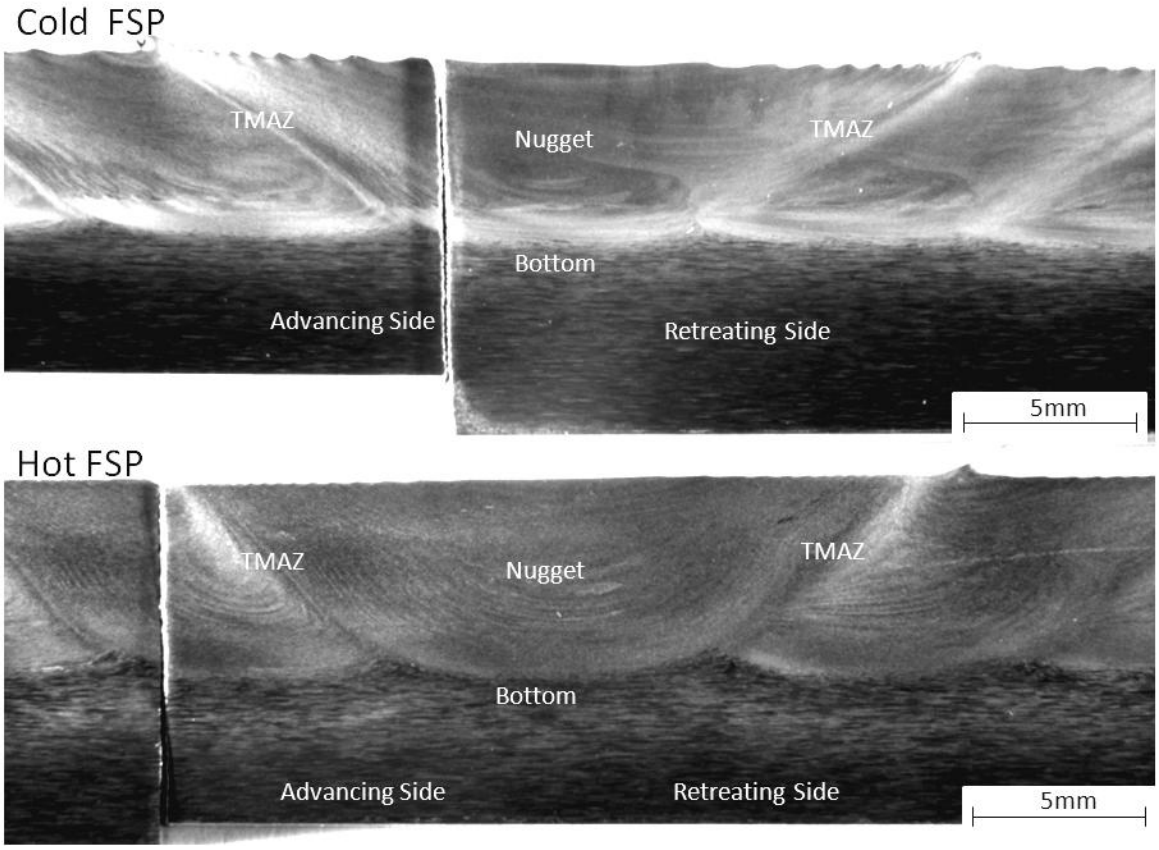

Figure 4.4 – Macroscopic images showing the central weld structures for the hot and cold parameters FSPs, etched using Keller's to reveal the grain structure taken from a cross-section in the longitudinal plane

Figure 4.6 shows how the microstructure of the central nugget of the both FSPs changes with increasing depth until the base material is reached. It can be seen that the depths of microstructural processing are similar with the hot averaging 7.1 mm and the cold averaging 6.8 mm. It can also be seen that the grain structure is slightly finer for the cold FSP parameter, particularly between depths of 1-5 mm with an average grain diameter of 5-7 μm in the cold parameter, compared with an average of 9-11μm in the hot conditions at a depth of 2.5 mm from the FSP surface.

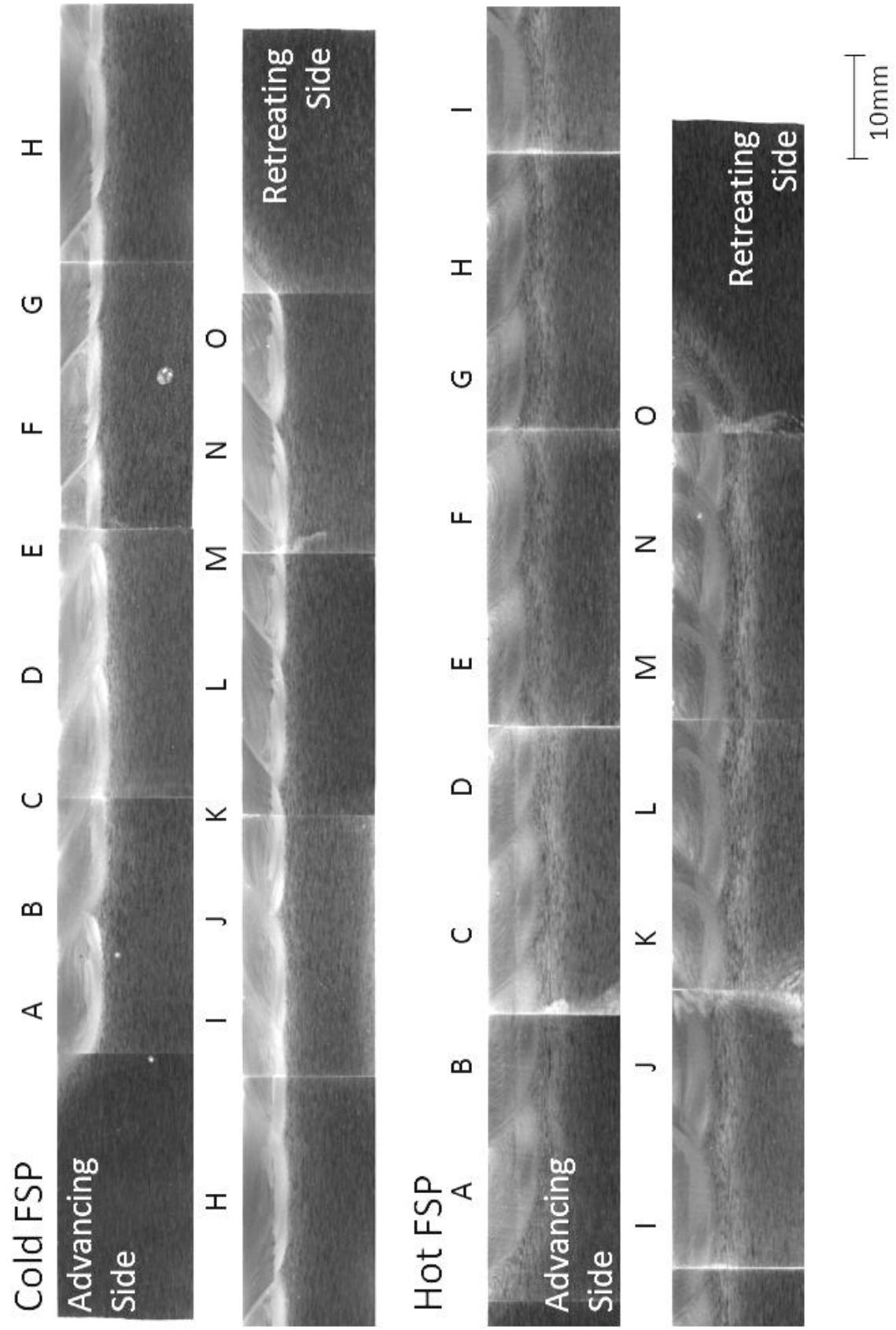

Figure 4.5 – Macroscopic images showing the cross-section of the entire hot and cold FSP passes, etched using Keller's reagent to reveal the grain structure taken from a cross-section in the longitudinal plane

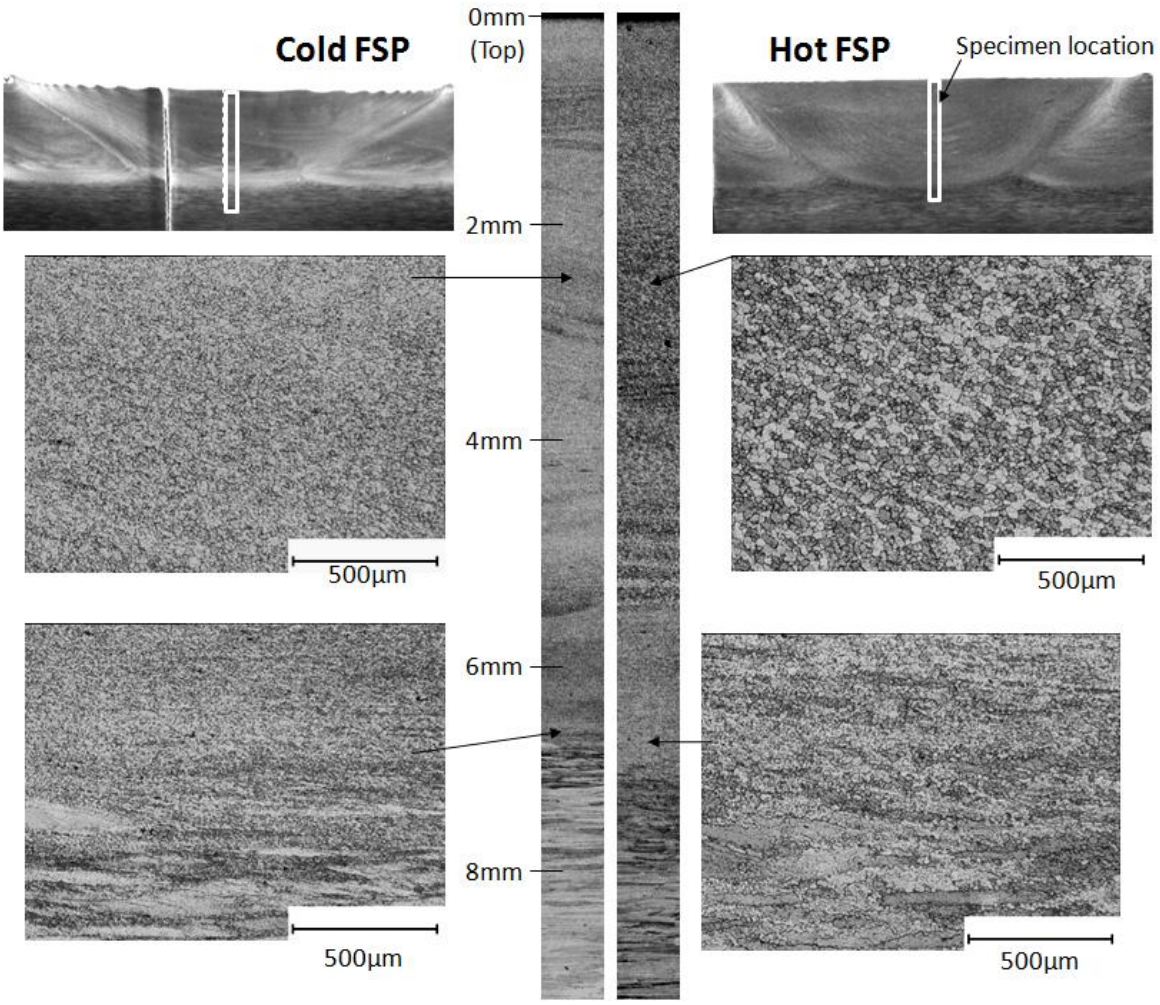

Figure 4.6 – Macroscopic and microscopic images showing the depth of hot and cold FSP microstructural mechanical deformations, taken from a cross-section in the longitudinal plane

4.2 – Microhardness Results

4.2.1 – FSW Microhardness

Figure 4.7 shows the hardness profile of the central FSW measured in hardness-Vickers (Hv), with a macroscopic image showing the hardness relative to the weld location.

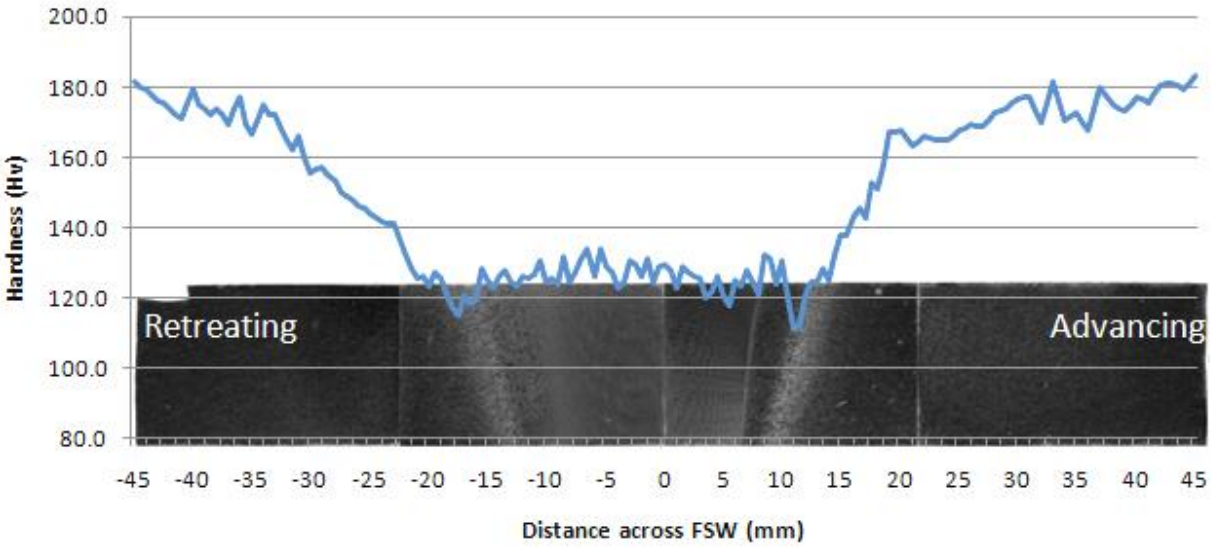

Figure 4.7 – Microhardness graph at a depth of 3 mm from the surface across the cross-section of the FSW, with a macrograph image showing the location across the weld

The hardness profile shown in Figure 4.7 is typical of a FS welded heat-treatable Al-alloy, with a decrease in hardness across the weld, with the lowest hardness recorded in the HAZ. There appears to be no significant difference between hardness on the advancing or retreating side.

4.2.2 – FSP Microhardness

The hardness profile of the hot and cold FSPs are shown also at a depth of 3 mm in Figure 4.8. It can be seen that the hardness is generally between 100-120 Hv across the structure. Figure 4.9 is a profile of hardness downwards from the surface through the middle of the central passes for the two FSP parameters. A measurement was made every 0.5 mm beginning at a depth of 2.5 mm from the original top surface to a depth of 12 mm from the original top surface. There is no significant difference between the hardness of the two FSP parameters. As shown in Section 4.1.3, the depth of microstructural modification is approximately 7.2 mm for the hot FSP and 6.8 mm for the cold FSP. This is consistent with the hardness profiles recorded as the hardness begins to increase at these depths.

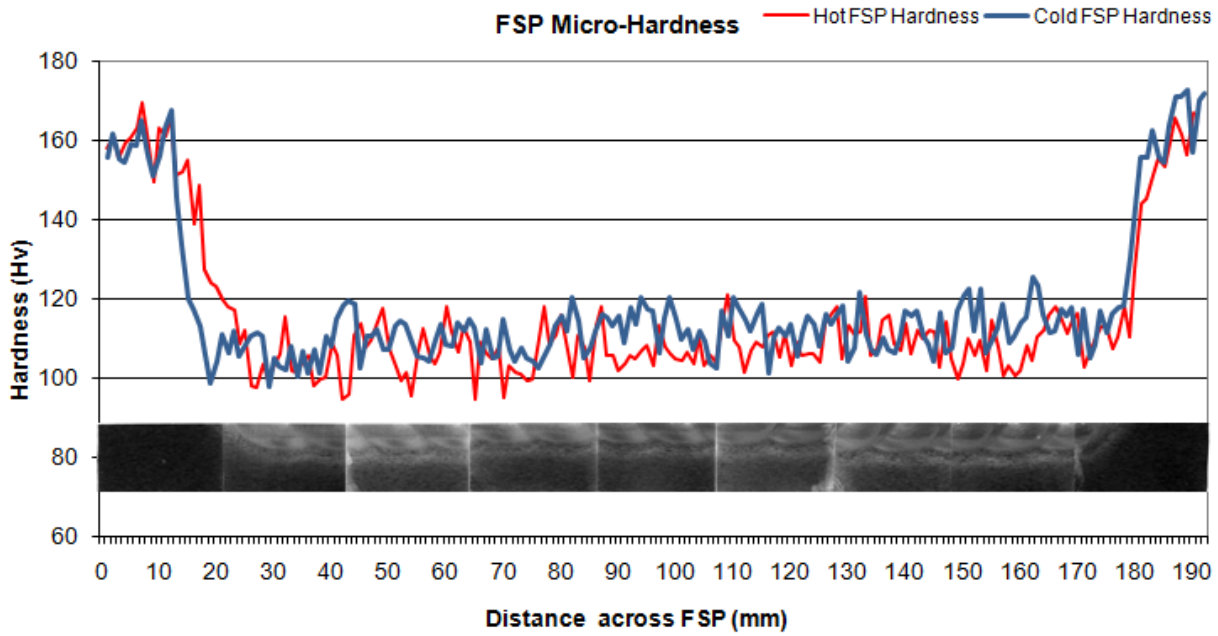

Figure 4.8 – Microhardness profile at a depth of 3 mm from the surface across the cross-section of the hot and cold FSPs, with a macrograph image showing the location across the hot FSP

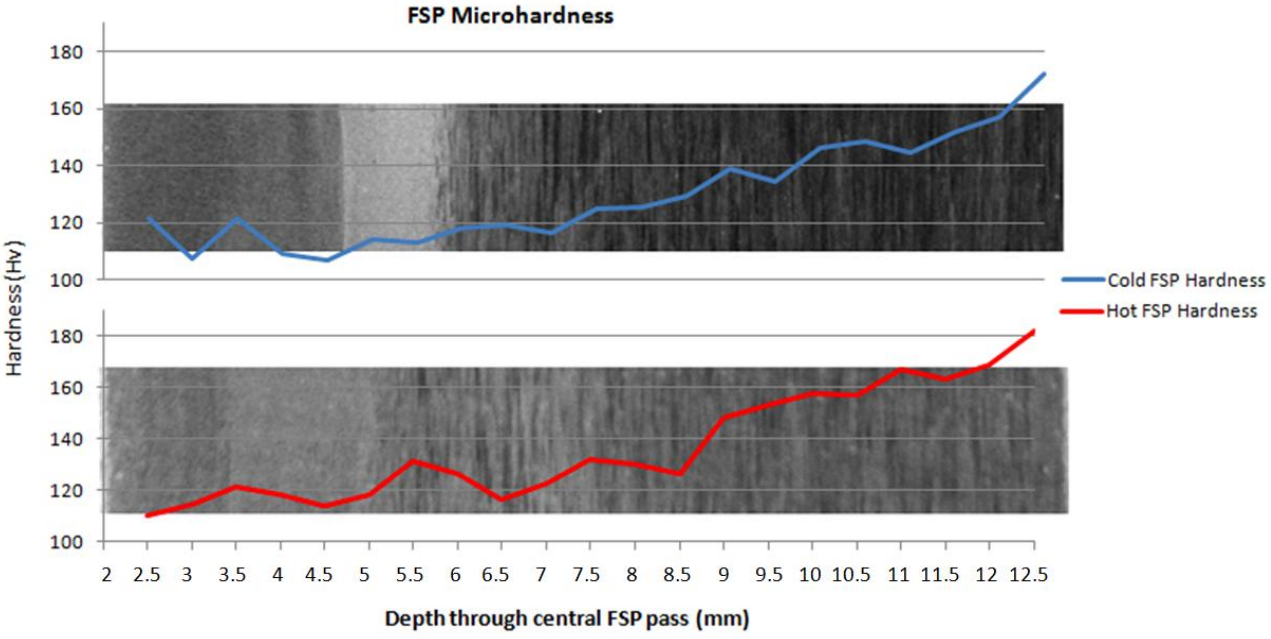

Figure 4.9 – Microhardness profile through the middle of the central hot and cold FSP nugget with a macrograph image showing the hardness relative to the depth of processing

4.3 – MASTMAASIS Results

Following a three part cyclic MASTMAASIS test of 45min spray – 120min drying – 195min soak, of acetic acid (NaCl 5% - pH 2.8-3) at 49°C for 750h a great deal of corrosive attack was found during surface and cross-section observations. The base material displayed severe pitting and intragranular attack, which can be seen in Figure 4.10.

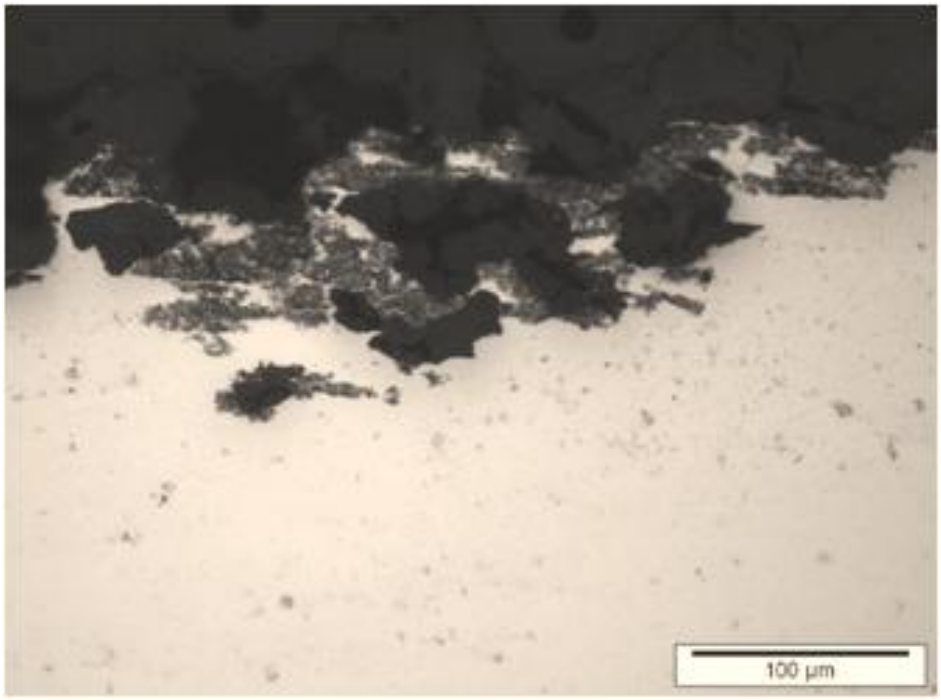

Figure 4.10 – Optical micrograph of intragranular corrosion in the AA2050 base material following 750h MASTMAASIS test taken from a cross-section in the transverse plane

The FSW showed severe IGC in the nugget TMAZ, and TMAZ-HAZ interface, with attack reaching depths of up to 340 µm, as shown in Figure 4.11. In the weld HAZ there was IGC, as well as intragranular attack, and signs of exfoliation corrosion, as show in Figure 4.12. The exfoliation corrosion in Figure 4.12 can be identified apart from standard IGC as the attack travels parallel to the surface lifting sections of the surface upwards away from the bulk of the material.

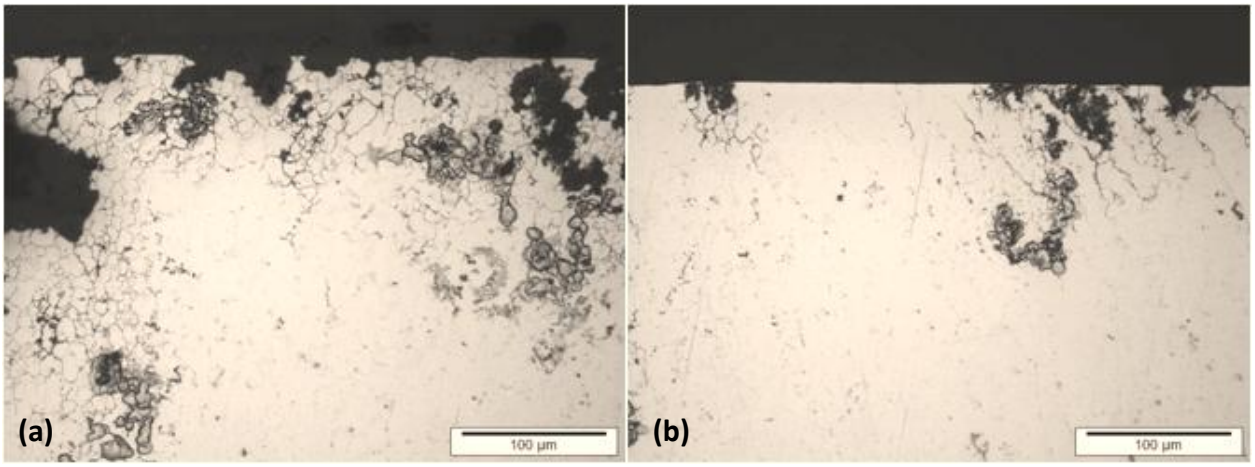

Figure 4.11 – Optical micrographs of IGC attack in (a) the nugget, and (b) the TMAZ-HAZ boundary, of the AA2050 FSW, following 750h cyclic MASTMAASIS testing taken from a cross-section in the transverse plane

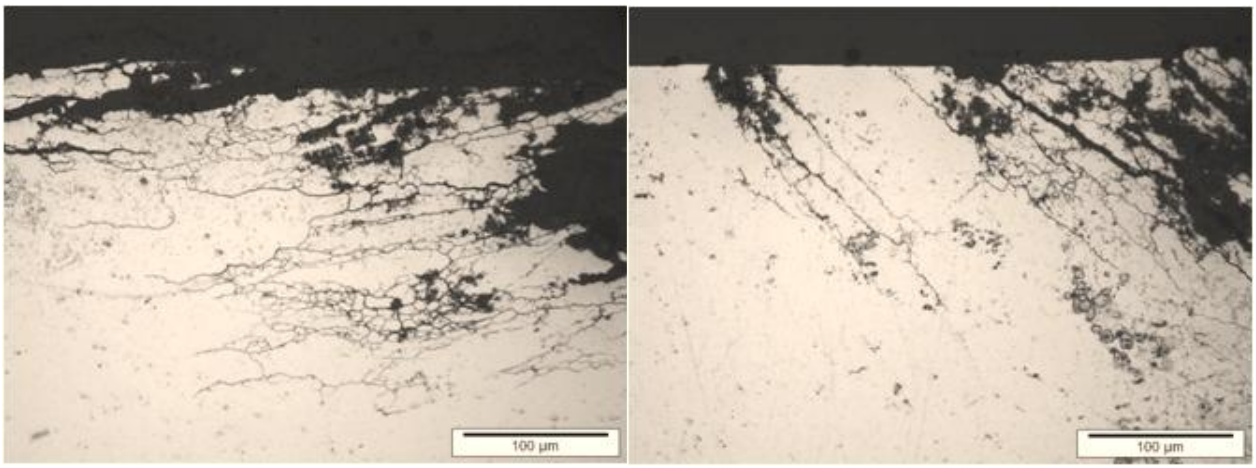

Figure 4.12 – Optical micrographs of IGC and exfoliation corrosion in the FSW HAZ of AA2050 following a 750h cyclic MASTMAASIS test

Inspection of the FSPs following the MASTMAASIS testing showed no significant difference between hot or cold parameters. IGC was the most prevalent form of attack across both FSPs. However, exfoliation attack was observed within the HAZ of the cold FSP. Figure 4.13 shows the examples of attack sites across the hot FSP where attack reached depths of up to 300µm, while Figure 4.14 shows the attack across the cold FSP.

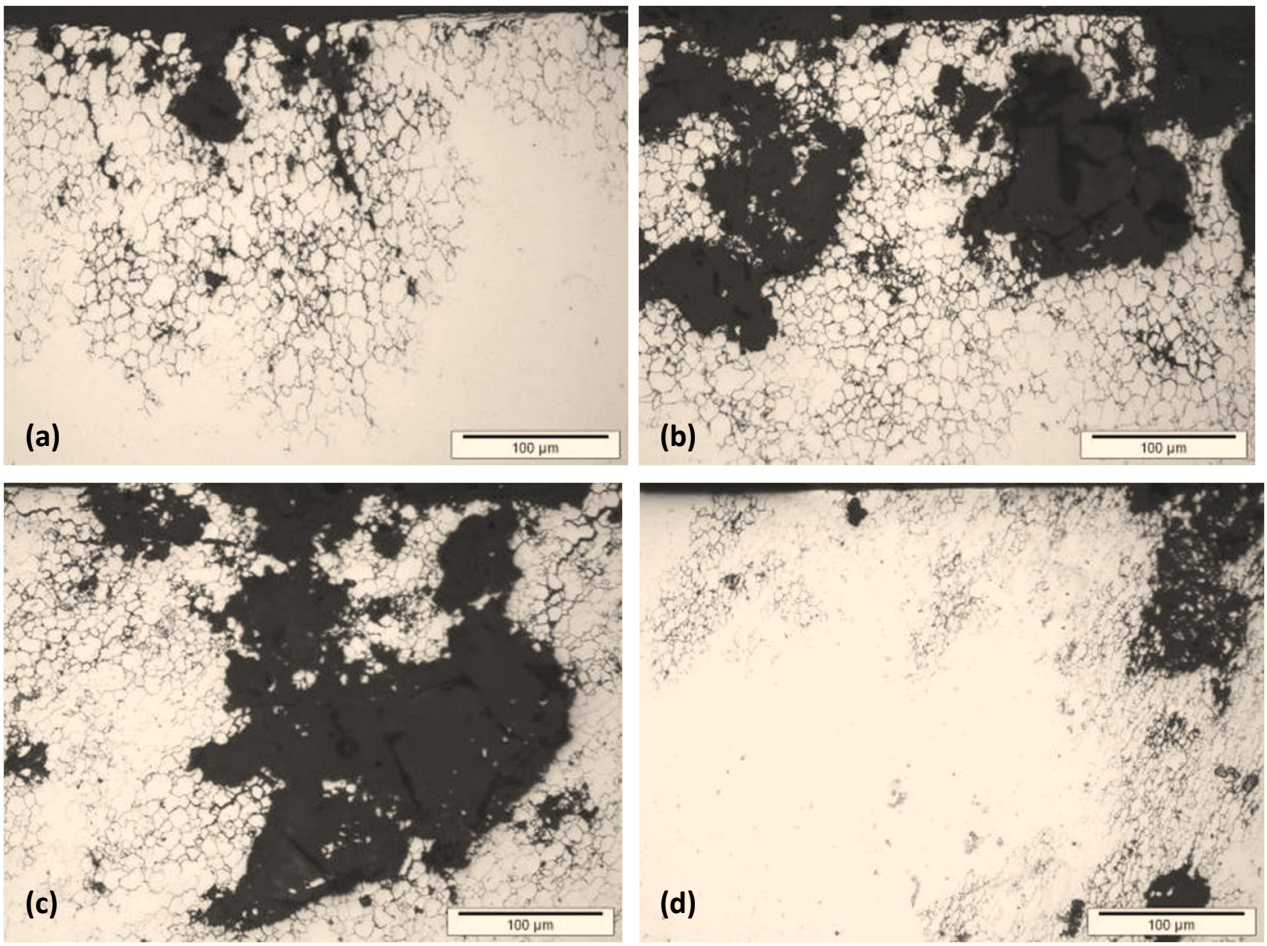

Figure 4.13 – Optical micrographs of IGC attack across the hot FSP of AA2050, following cyclic MASTMAASIS testing, in passes (a) C, (b) F, (c) H, and (d) I

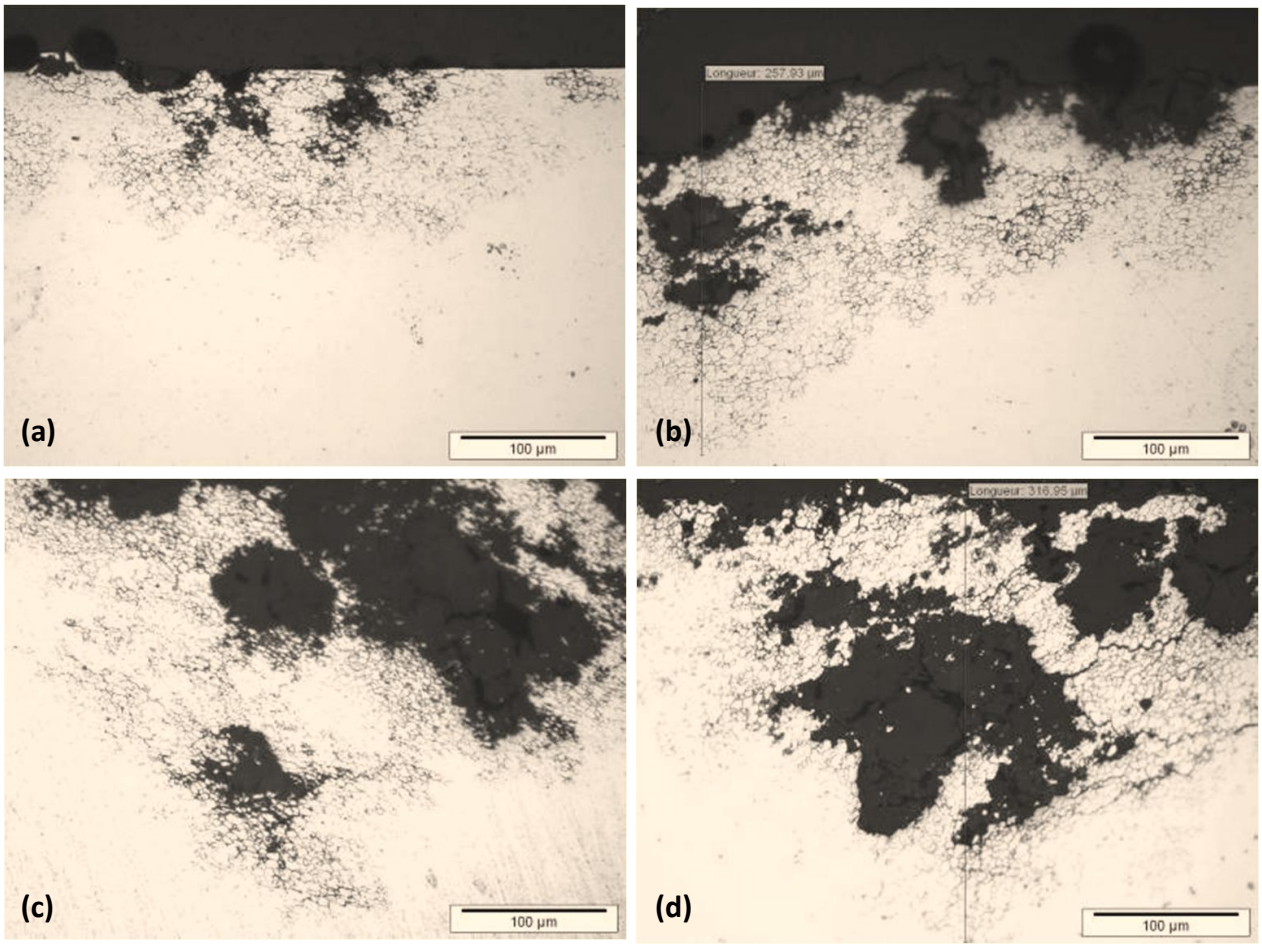

Figure 4.14 – Optical micrographs of IGC attack across the cold FSP of AA2050, following cyclic MASTMAASIS testing, in passes (a) C, (b) E, (c) H, and (d) I

4.4 – Immersion Results

4.4.1 – Immersion Surface Characteristics

4.4.1.1 – FSW Immersion Characteristics

The polished top surface of the friction-stir weld was immersion tested in a naturally aerated 0.1 M NaCl solution for 10 days. Figure 4.15 is an optical macrograph of the corroded specimen with (a) the corrosion product on the surface, and (b) the corrosion product removed by very gentle polishing. Figure 4.15(a) shows an even amount of corrosion product across most of the weld structure, with increased amounts of product in the unaffected base material on both advancing and retreating sides. The lighter regions on the surface of Figure 4.15(b) are the locations of small pits, which appear to follow a striated pattern through the centre of the pass, with the TMAZ on both sides showing reduced pitting attack. The HAZ appears to show a gradual change in the degree of pitting attack with the most severe attack being close to the TMAZ and reducing slightly with increasing distance from the centre of the weld. The unaffected base material suffers from extremely severe pitting on both advancing and retreating sides where very large individual pits can be seen. Figure 4.16 shows how the base material was far more susceptible to pitting than the FSW HAZ.

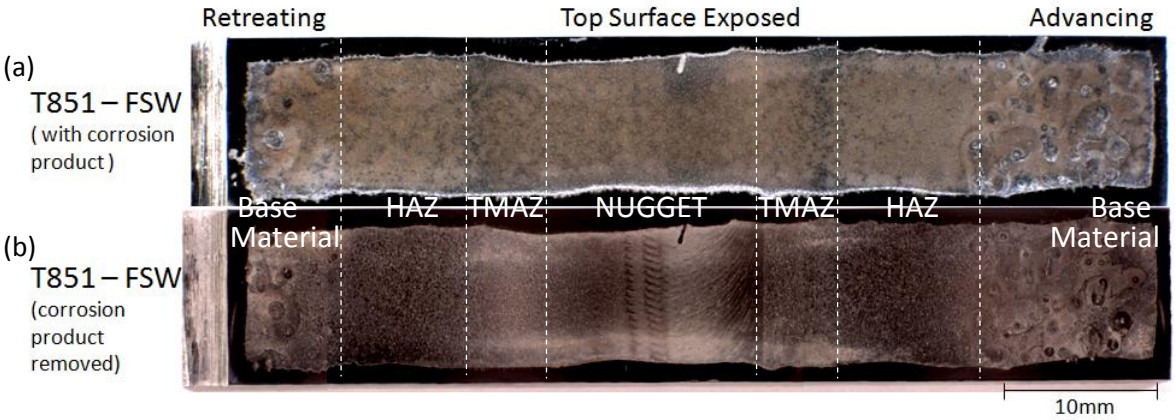

Figure 4.15 – Optical macrograph images showing the top surface of the FSW specimen following 10 day 0.1M NaCl immersion test with, (a) the corrosion product on the surface, and (b) the corrosion product remove via gentle polishing

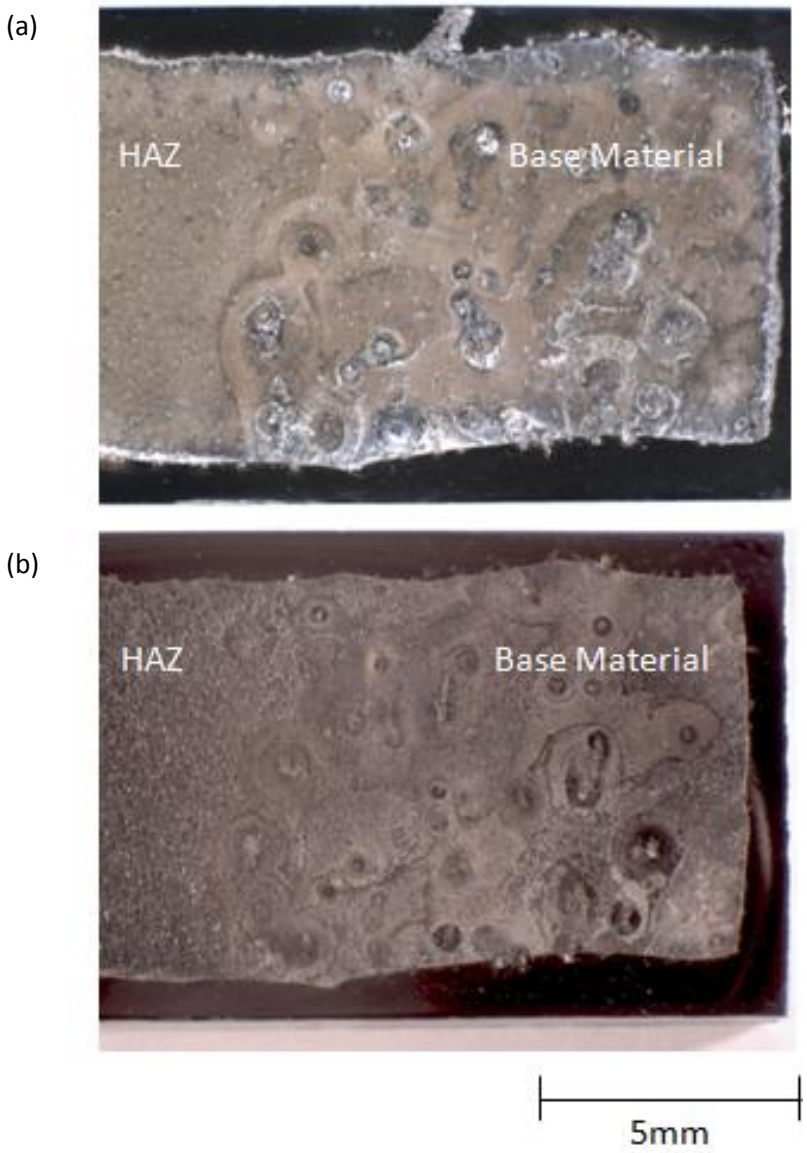

Figure 4.16 – Optical macrograph showing severe pitting in the base material following 10 day 0.1 M NaCl immersion test with (a) the corrosion product on the surface, and with (b) the corrosion product removed

4.4.1.2 – Cold FSP Immersion Characteristics

Figure 4.17 is a series of digital macroscopic images showing cold FSP specimens following 10 day, 0.1 M NaCl immersion testing, with (a) the corrosion product on the surface, (b) the corrosion product removed, (c) the cross-section and plan view of the relative FSP passes with the locations of severe pitting attack, and (d) the plan view of the entire series of cold FSP passes with the locations of severe pitting attack. A degree of generalised

small pitting was observed across the entire specimen. However, there were a number of strips of severely attacked material in the form of large pits that coincide with the boundaries between passes. It can also be seen that the advancing side appears to only be subject to mild pitting attack and does not suffer from the severe pitting seen at the boundaries close to the central pass. The passes that suffered from severe pitting were the boundaries of passes G-H, H-I, I-J, J-K, and K-L as located in Figure 4.17(d). The unaffected base material also suffered from severe large pitting attack, similar to those shown in the base material of the FSW in Figure 4.16.

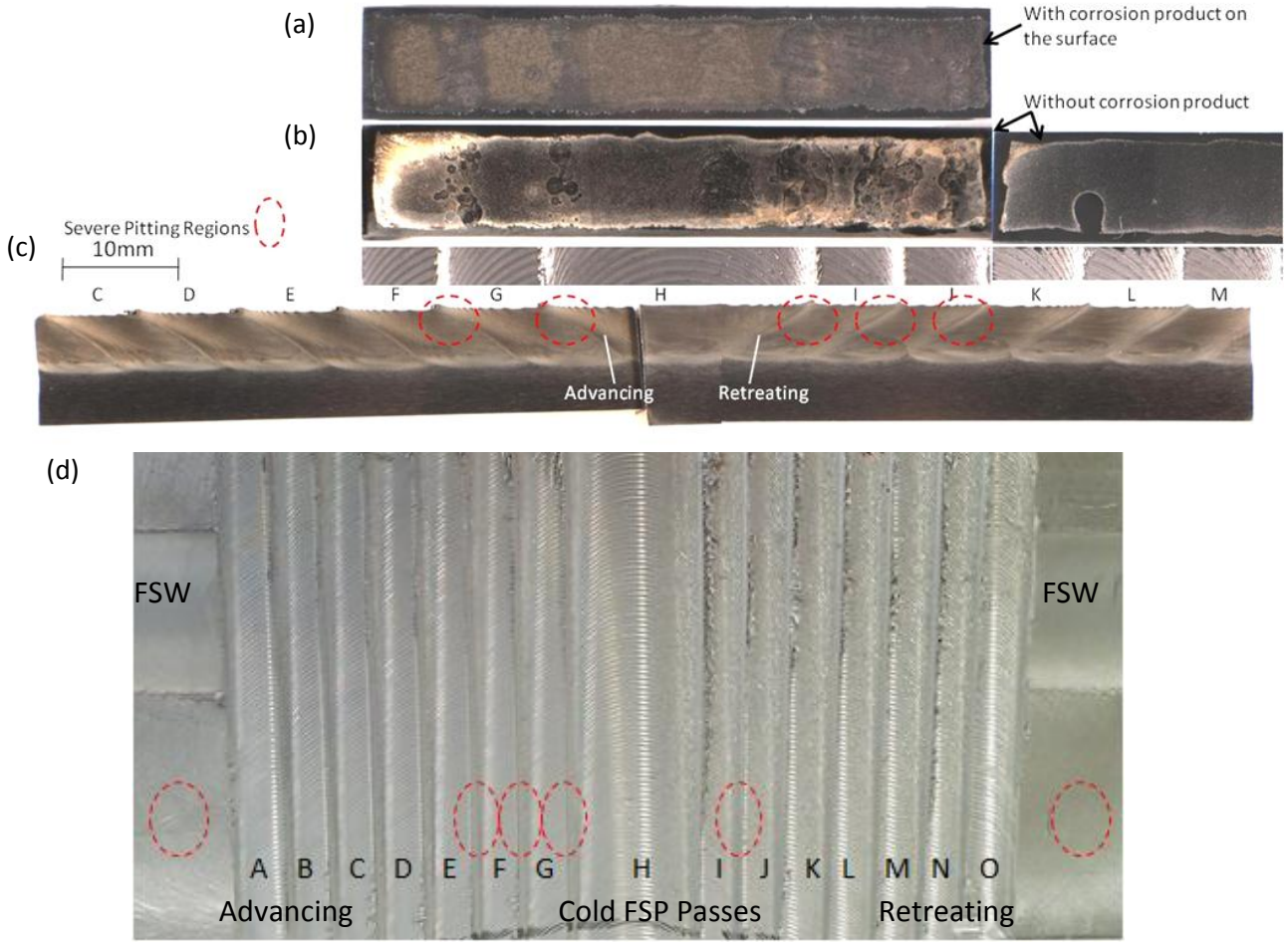

Figure 4.17 – Series of optical macrographs showing cold FSP specimens following 10 day, 0.1 M NaCl immersion testing, with (a) the corrosion product on the surface, (b) the corrosion product removed, (c) the cross-section and plan view of the relative FSP passes with the locations of severe pitting attack, and (d) the plan view of the entire series of cold FSP passes with the locations of severe pitting attack

4.3.1.3 – Hot FSP Immersion Characteristics

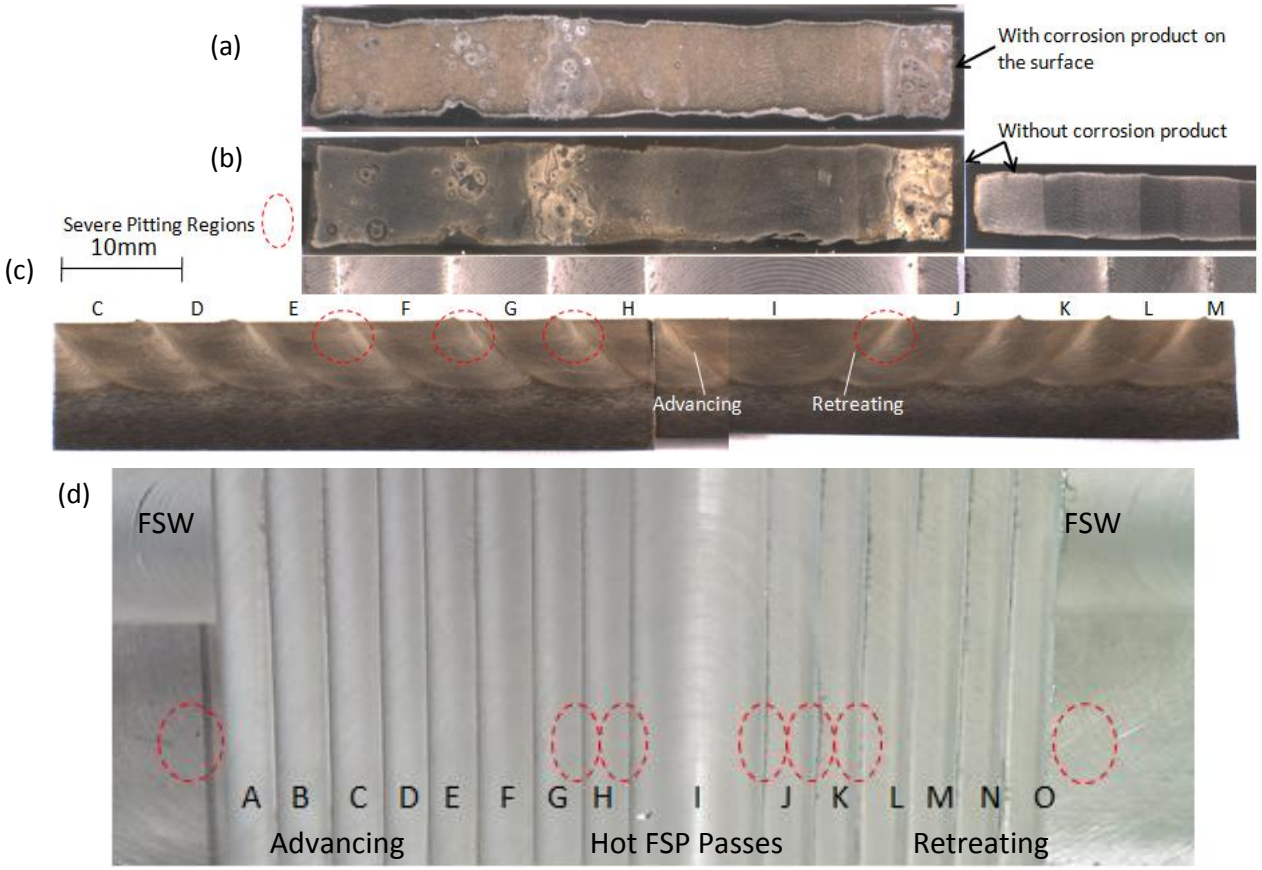

Figure 4.18 – Series of optical macrographs showing hot FSP specimens following 10 day, 0.1M NaCl immersion testing, with (a) the corrosion product on the surface, (b) the corrosion product removed, (c) the cross-section and plan view of the relative FSP passes with the locations of severe pitting attack, and (d) the plan view of the entire series of cold FSP passes with the locations of severe pitting attack

Figure 4.18 is a series of digital macrograph images showing hot FSP specimens following 10 day, 0.1 M NaCl immersion testing, with (a) the corrosion product on the surface, (b) the corrosion product removed, (c) the cross-section and plan view of the relative FSP passes with the locations of severe pitting attack, and (d) the plan view of the entire series of cold FSP passes with the locations of severe pitting attack. In a similar observation to those of the cold FSP parameters, there are regions of corrosion resistance and corrosion susceptibility across the structure. As can be seen in Figure 4.18(d) the worst affected areas

were at the boundaries between passes E-F, F-G, G-H, and I-J, while the remaining FSP surface (not shown) suffered only minor pitting attack. As with the FSW and cold FSP immersion tests, the base material suffered from severe pitting attack.

4.4.2 – Depth of Attack Analysis

Once superficial analysis of the corroded top surface was complete, the specimens were cut through in the transverse plane (see Figure 3.3) to reveal a cross-section that could be used to determine the depth and mode of corrosion attack. Four distinct corrosion modes were identified; pitting corrosion, intergranular corrosion (IGC), pitting with IGC corrosion, and intragranular corrosion. Figure 4.19 shows examples of each of the four modes of attack and how the depth of attack was measured. Each corrosion site was categorised into depths of either; up to 5 µm deep, up to 10 µm deep, up to 20 µm deep, or 30 µm and deeper.

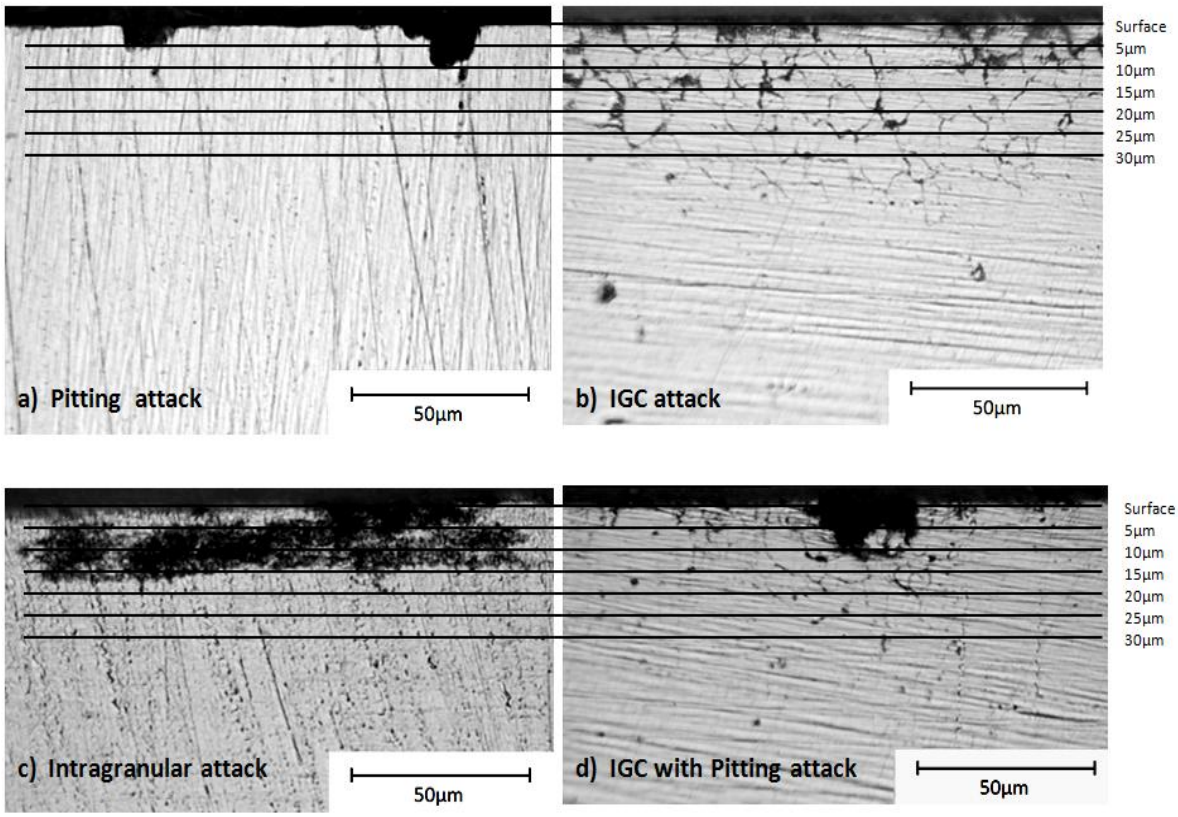

Figure 4.19 – Optical micrographs illustrating the method of determining the depth of attack analysis with examples of, a) pitting attack, b) IGC attack, c) intragranular attack, d) pitting with IGC attack

4.4.2.1 – Base Material Depth of Attack

The base material suffered from severe pitting and intragranular attack, with both producing a large number of attack sites deeper than 30 µm. This can be seen throughout Figures 4.21 - 4.25. It can also be seen that the base material appears to be resistant to IGC, with no sites with IGC alone in any base material across any test specimens, and only a few pits with IGC developing from them.

4.4.2.2 – FSW Depth of Attack

Pitting Corrosion

Pitting attack was observed when the FSW was immersion tested at both 2mm and 13mm depths. However, this attack was often shallow and rarely deeper than 10 µm. The centre of the FSW nugget, particularly at 13 mm deep, appears well protected from pitting attack. However, there were two sites of deep pitting attack in the nugget at 2 mm deep. Figure 4.20 are a series of SEM images taken across the surface of the FSW nugget region in which pitting, and pitting with IGC can be seen. Figure 4.21(c)-(d) suggests that at 2 mm the advancing TMAZ was less susceptible to pitting, while at 13 mm the retreating side was less susceptible. With regards the HAZ, the advancing side of the weld was less susceptible to pitting attack.

Intragranular Corrosion

The locations and severity of attack of intragranular corrosion can be seen in Figure 4.22(c)-(d), and apart from a few incidences is found primarily in the TMAZa, and on both advancing and retreating HAZ regions. There was one incident of shallow intragranular attack in the nugget, and one similar incident in the TMAZr. Figure 4.22(c)-(d) suggests the advancing side is more susceptible to intragranular attack in both TMAZ and HAZ regions.

IGC

The locations and severity of IGC attack follows an almost identical pattern to that of the pitting with IGC attack, as shown in Figure 4.23(c)-(d). It can be seen that the weld nugget is the worst affected, particularly at 2 mm deep, while the TMAZ shows signs of some shallower attack, and the HAZ records almost no IGC. There appears to be little difference in attack between advancing and retreating sides of the weld at either depth.

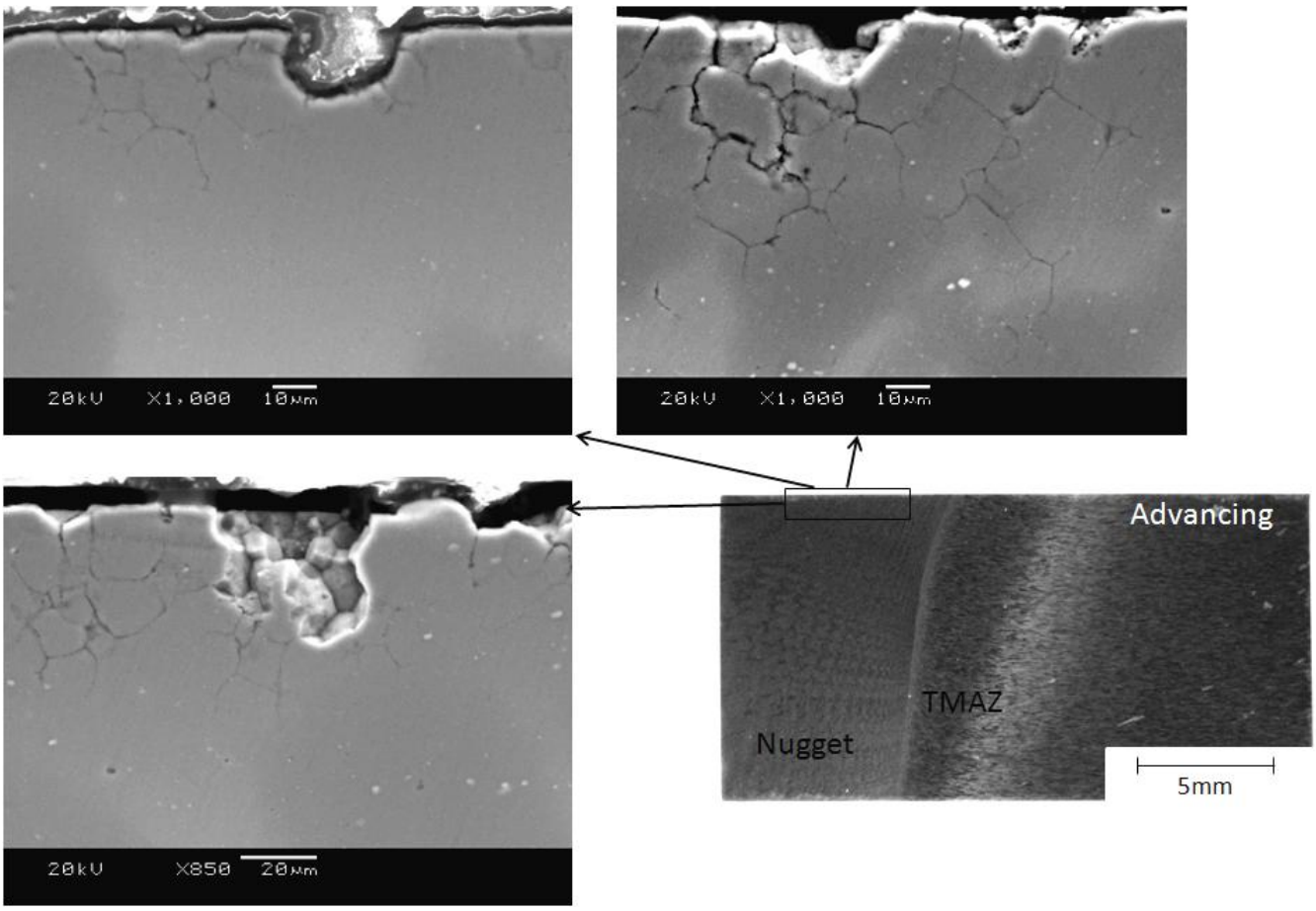

Figure 4.20 – A series of scanning electron microscope images illustrating examples of pitting and pitting with IGC across the surface of the FSW nugget

Pitting with IGC

Figure 4.24(c)-(d) shows the location and severity of pitting and IGC attack across the FSW at 2 mm and 13 mm depths. From this it can be seen that all regions of the weld at both depths were susceptible to pitting with IGC, with the weld nugget attacked most severely at both depths and the weld HAZ proving to be the least susceptible. The advancing sides, as with pitting above, appear to be less susceptible at 2 mm, and more susceptible at 13 mm in the TMAZ and HAZ regions.

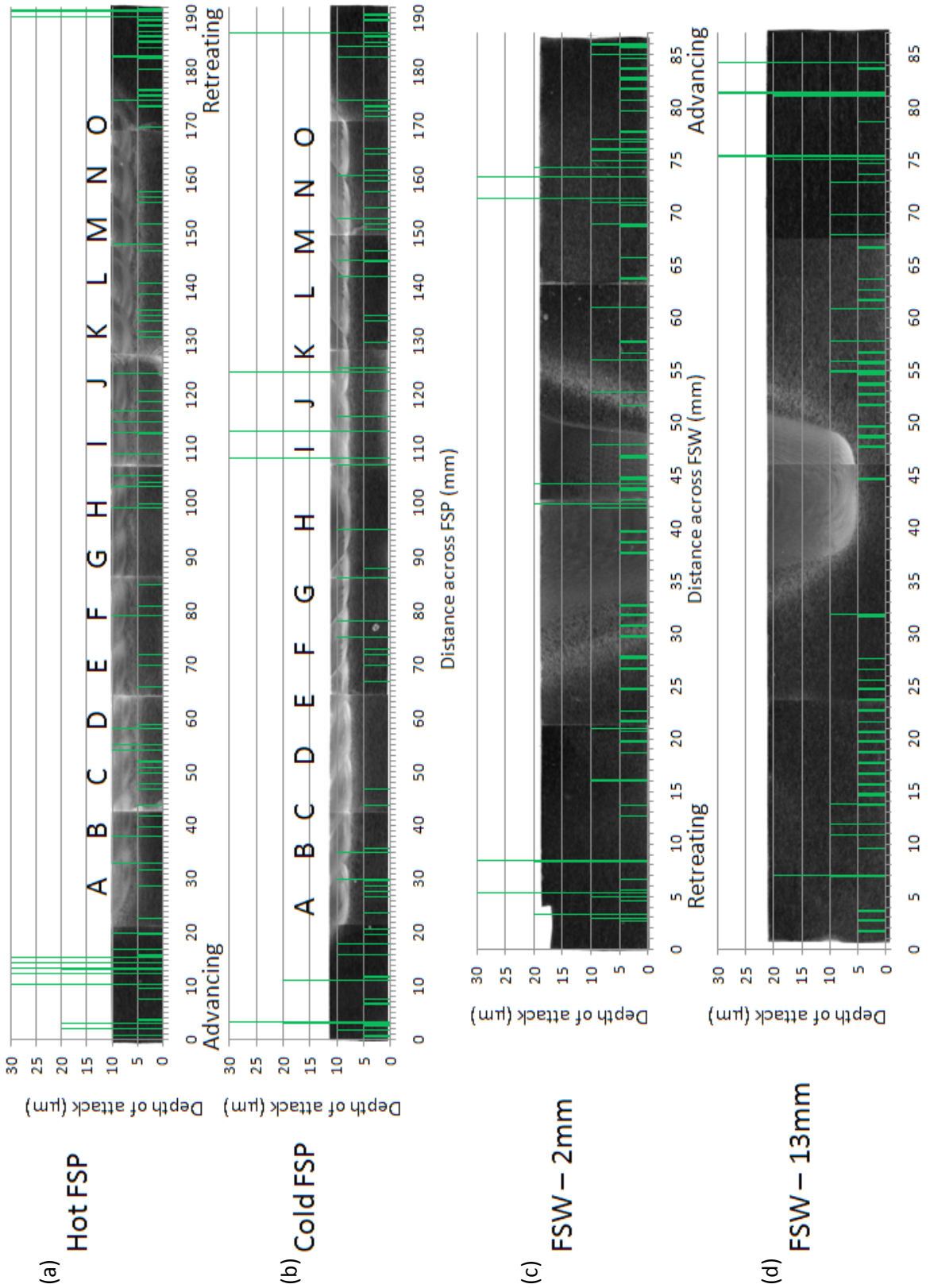

Figure 4.21 – A series of optical macrographs with corrosion data showing pitting attack locations and depths across (a) hot FSP, (b) cold FSP, (c) FSW at 2 mm deep, and (d) FSW at 13 mm deep

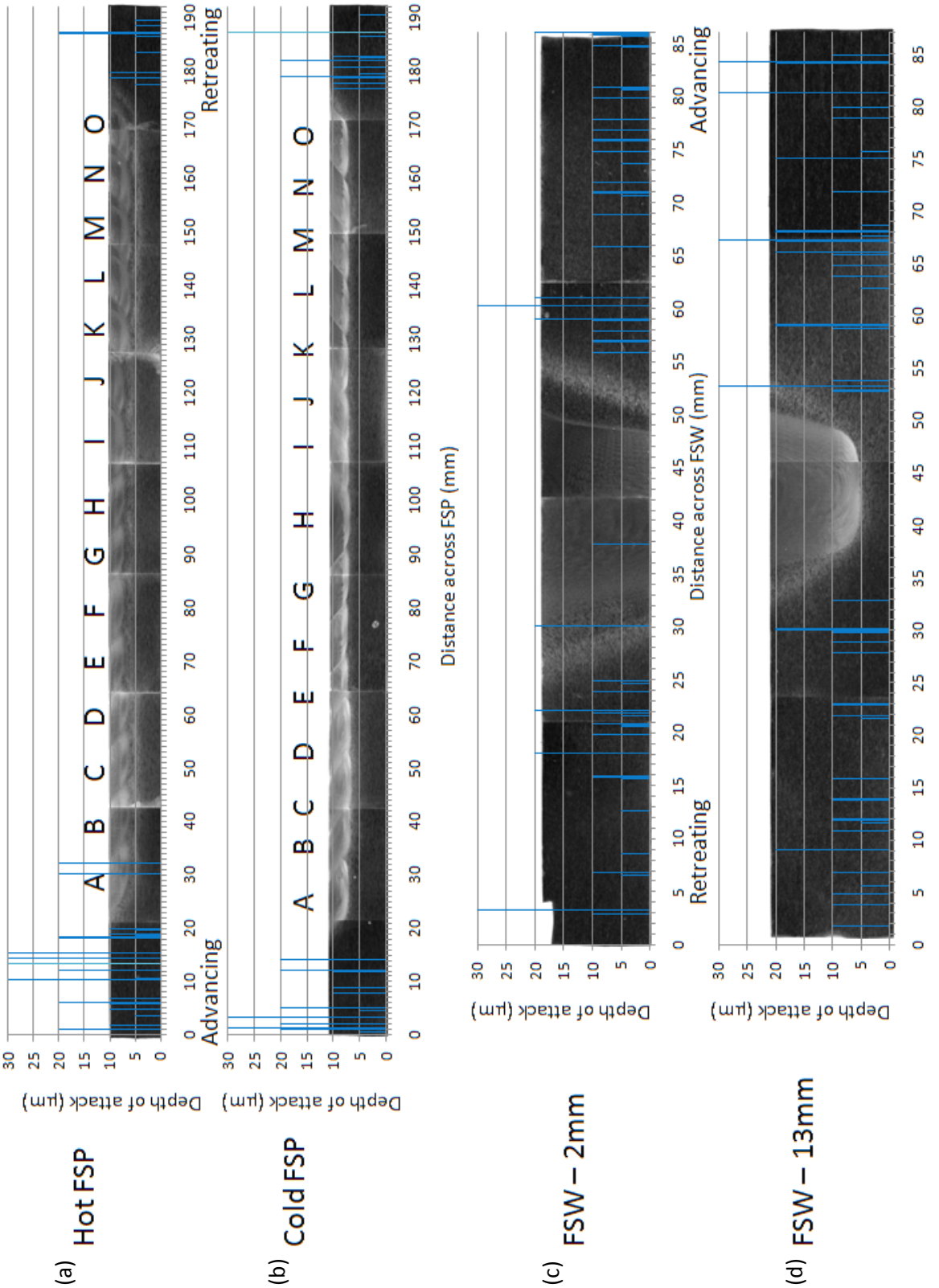

Figure 4.22 – A series of optical macrographs with corrosion data showing intragranular attack locations and depths across (a) hot FSP, (b) cold FSP, (c) FSW at 2 mm deep, and (d) FSW at 13 mm deep

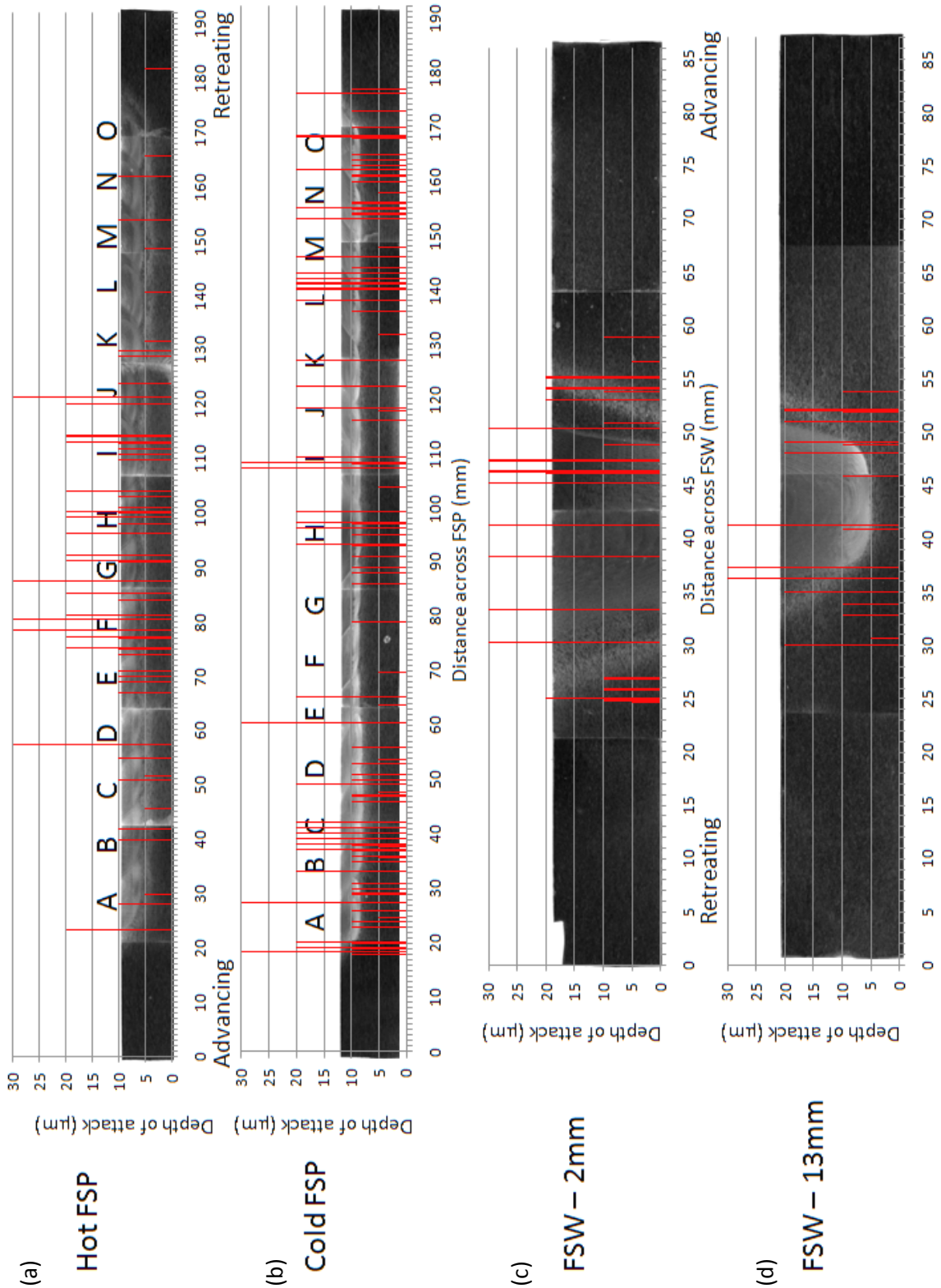

Figure 4.23 – A series of optical macrographs with corrosion data showing IGC attack locations and depths across (a) hot FSP, (b) cold FSP, (c) FSW at 2 mm deep, and (d) FSW at 13 mm deep

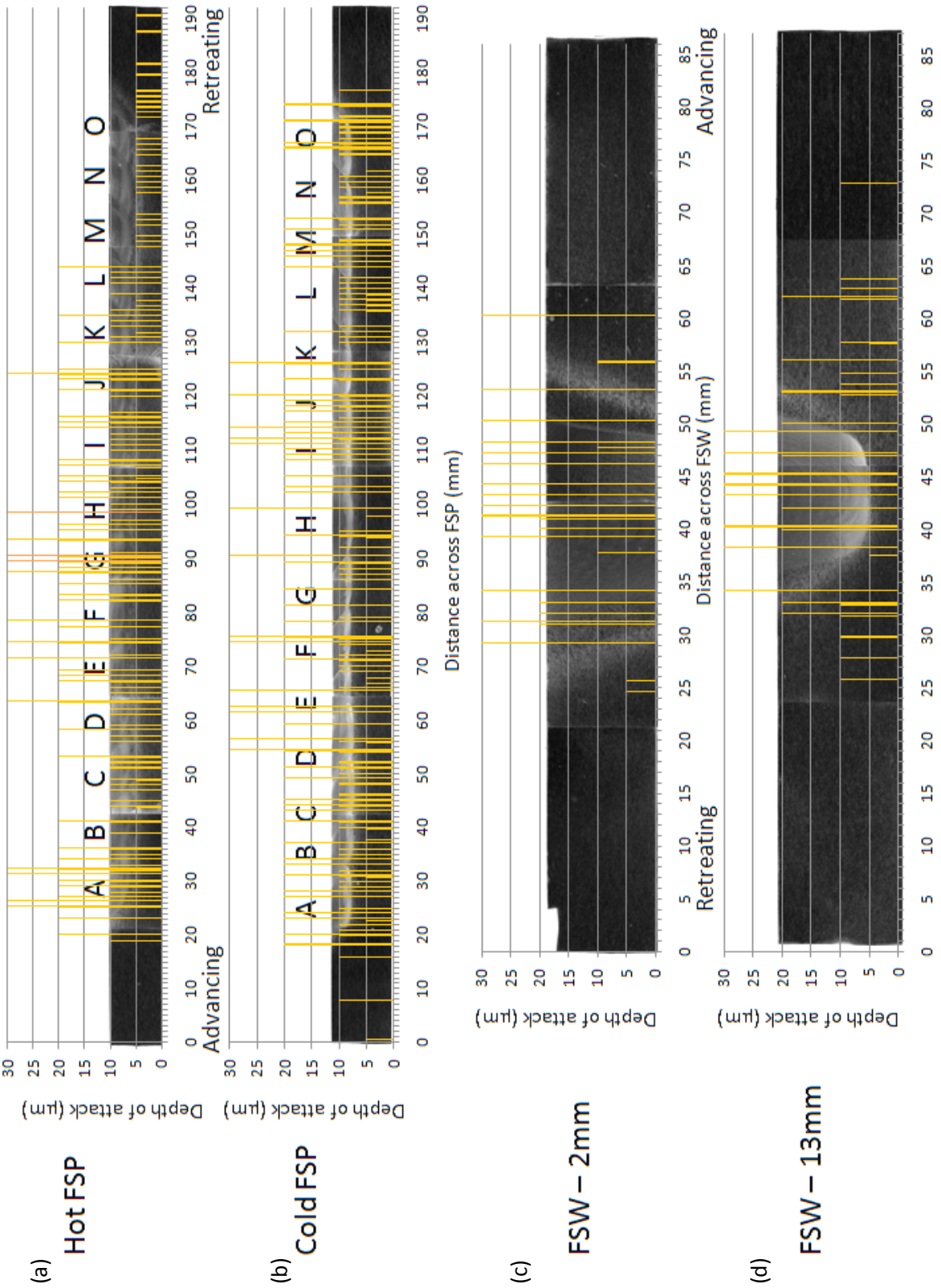

Figure 4.24 – A series of optical macrographs with corrosion data showing pitting with IGC attack locations and depths across (a) hot FSP, (b) cold FSP, (c) FSW at 2 mm deep, and (d) FSW at 13 mm deep

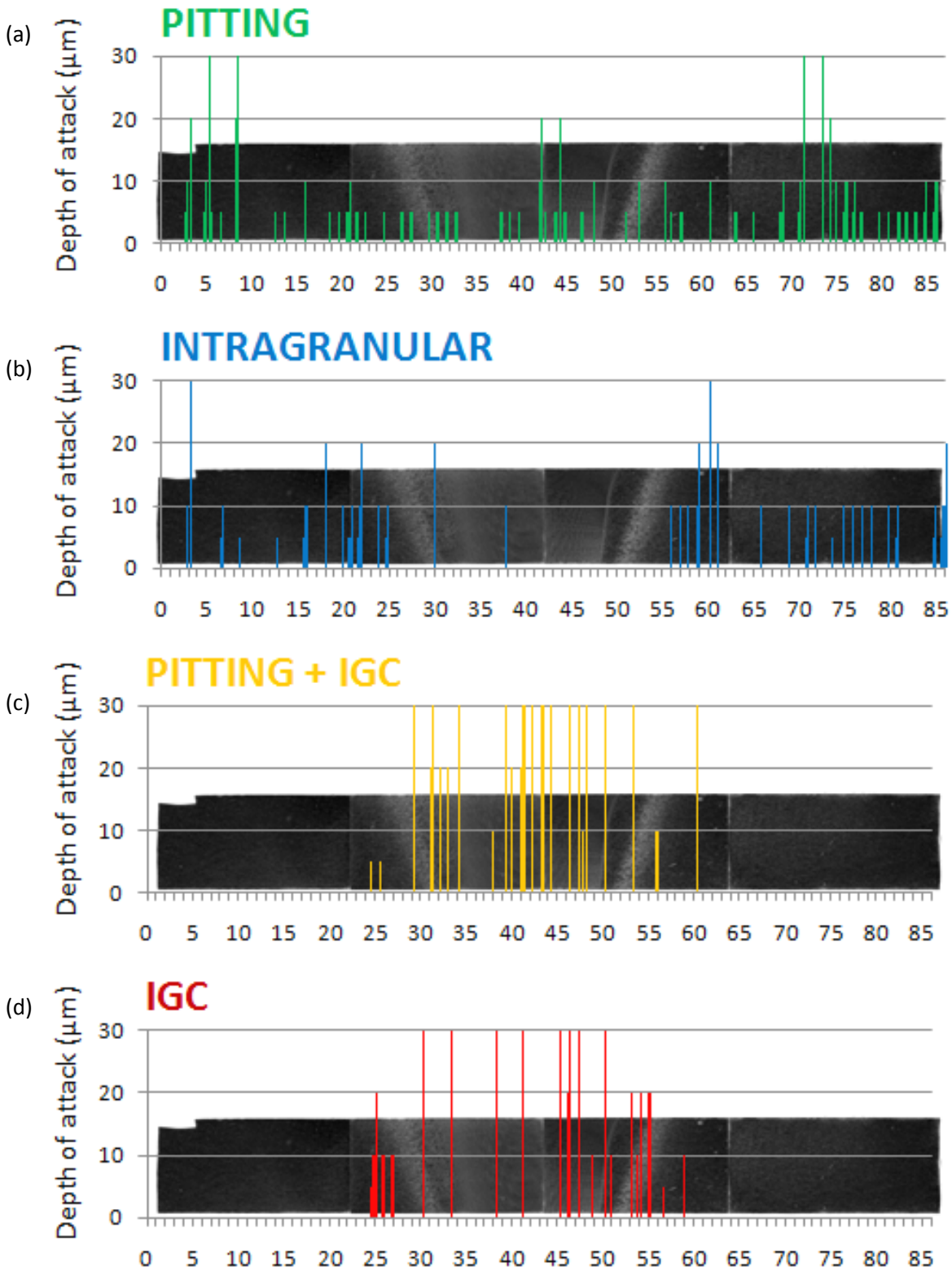

Figure 4.25 – Attack locations and depths across the FSW at 2 mm deep for (a) pitting attack, (b) intragranular attack, (c) IGC attack, and (d) pitting with IGC attack

4.4.2.3 – FSP Depth of Attack

Pitting Corrosion

Figure 4.21(a)-(b) shows the location and severity of pitting attack across both hot and cold FSPs. It can be seen that in comparison to the base material, the processed region is less susceptible to pitting attack, in a similar way to the FSW. The frequency of attack sites across the FSPs is much lower than the surrounding base material and the vast majority of attacks are 10 µm or shallower, which is a great improvement on the pitting susceptibility compared to the base material. There were three incidences of deep pitting attack on the retreating side of the cold FSP, between passes I-K, an example of this is shown in Figure 4.26. There was little difference between hot and cold FSPs, or between advancing and retreating sides of the passes, with just a few discreet areas recording no pitting attack at all; passes D-E in the cold FSP, and passes G and N in the hot FSP being the only fully pitting protected regions.

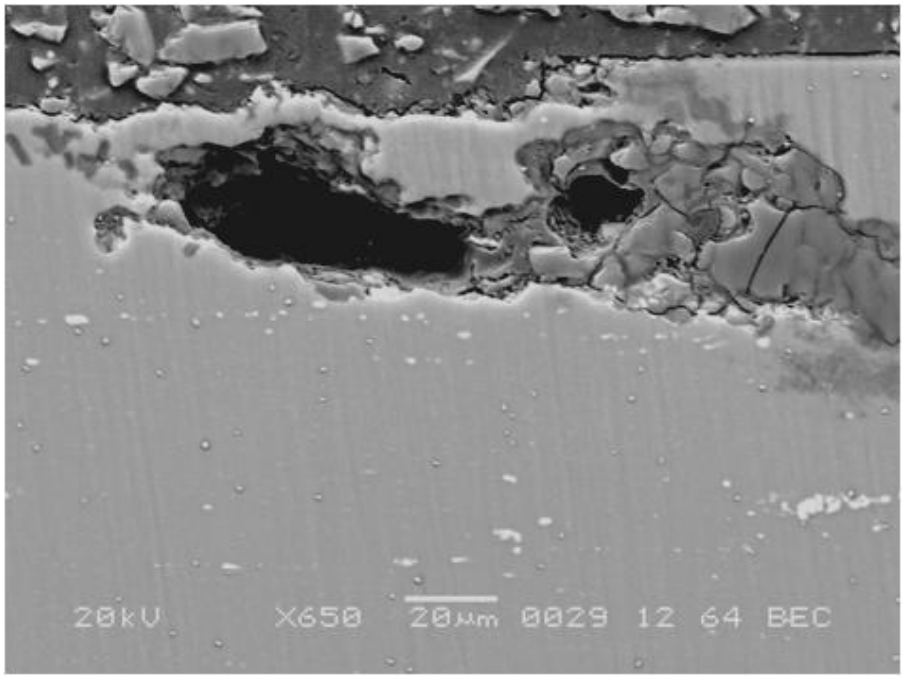

Figure 4.26 – Scanning electron microscope image of severe pitting attack in the retreating side of the cold FSP

Intragranular Corrosion

Figure 4.22(a)-(b) shows the hot and cold FSPs location and severity to intragranular corrosion attack. It can be seen that both conditions produce material that is very much resistant to intragranular attack in comparison to base material which is largely susceptible. Only two incidences of intragranular attack were identified across all of the FSPs, both of which were within pass A under hot conditions. It can be seen that intragranular attack is present at both edges of each of the FSPs where the HAZ must exist. This is similar to the FSW, which also recorded dramatically intragranular corrosion resistant material, particularly in the nugget and TMAZ regions. This suggests that it is the mechanical deformation that prevents the intragranular corrosion process.

IGC

Intergranular corrosion attack sites and depths, as shown in Figure 4.23(a)-(b), follow a similar pattern to those recorded for pitting with IGC attack. However, the frequency and severity is dramatically reduced. Like the FSW, the base material remains resistant to IGC attack, while the nugget and TMAZ regions appear susceptible and have thus suffered much IGC. There are no clear regions that appear to be totally resistant to IGC attack; however the hot FSP does perform better than the cold FSP, with regions of passes A-E, and K-O suffering reduced severity and frequency of IGC, despite a central region being more severely attacked. The cold FSP was more uniformly attacked across the entire FSP. Figure 4.27 is an example of severe IGC attack in the cold FSP, where it is clear to see how the grain boundaries have corroded preferentially. There does not appear to be a significant difference between advancing and retreating sides under either hot or cold conditions, and once again the attack does not appear to be limited to any localised regions within individual passes.

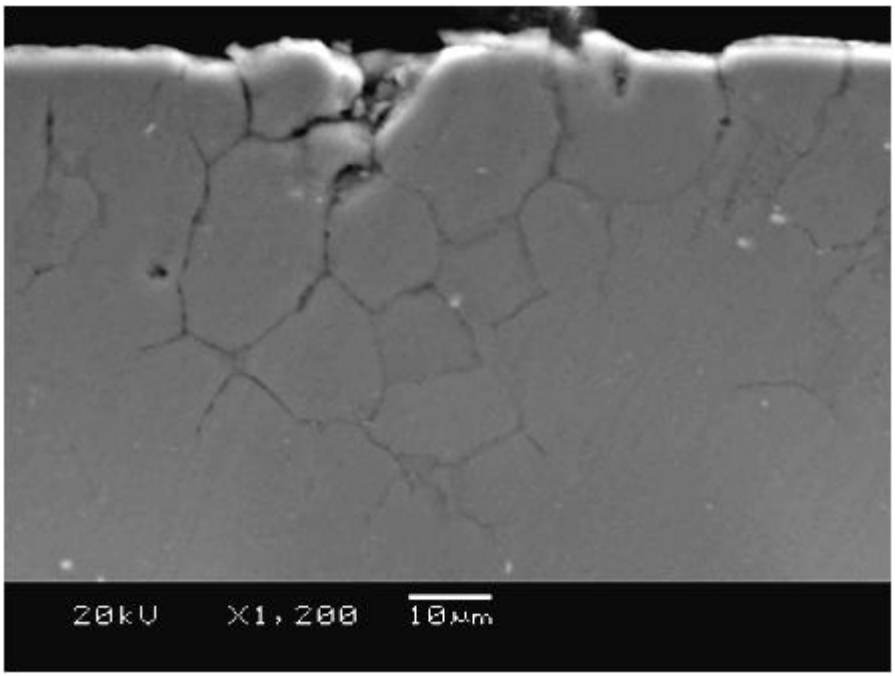

Figure 4.27 – Scanning electron microscope image of deep IGC attack in cold FSP

Pitting with IGC

The locations and severity of pitting with IGC attack across the hot and cold FSPs can be seen in Figure 4.24(a)-(b). It shows, much like the FSW, that there is a greatly increased susceptibility to pitting with IGC compared with the base material, with no areas being fully protected from attack across either FSP. There is no significant difference between hot and cold FSPs, with both have a high number of varying depths of attack across the entirety of their passes. The only region which exhibits slightly better resistive properties is between passes M-O, at the retreating side of the hot FSP. This region displayed only shallow, 5 µm deep attack, but still in a high frequency. Apart from this region in the hot FSP there was no further difference between advancing and retreating sides of either FSP. Similarly both hot and cold FSPs recorded more severe, deeper attack towards the centre of the FSPs, between passes D-K. Figure 4.28 shows two incidences of pitting with IGC across the nugget and retreating side of the cold FSP, while Figure 4.29 summarises the difference in location and

severity of IGC, and pitting with IGC across the hot FSP, illustrating the only notable protected region within the retreating side.

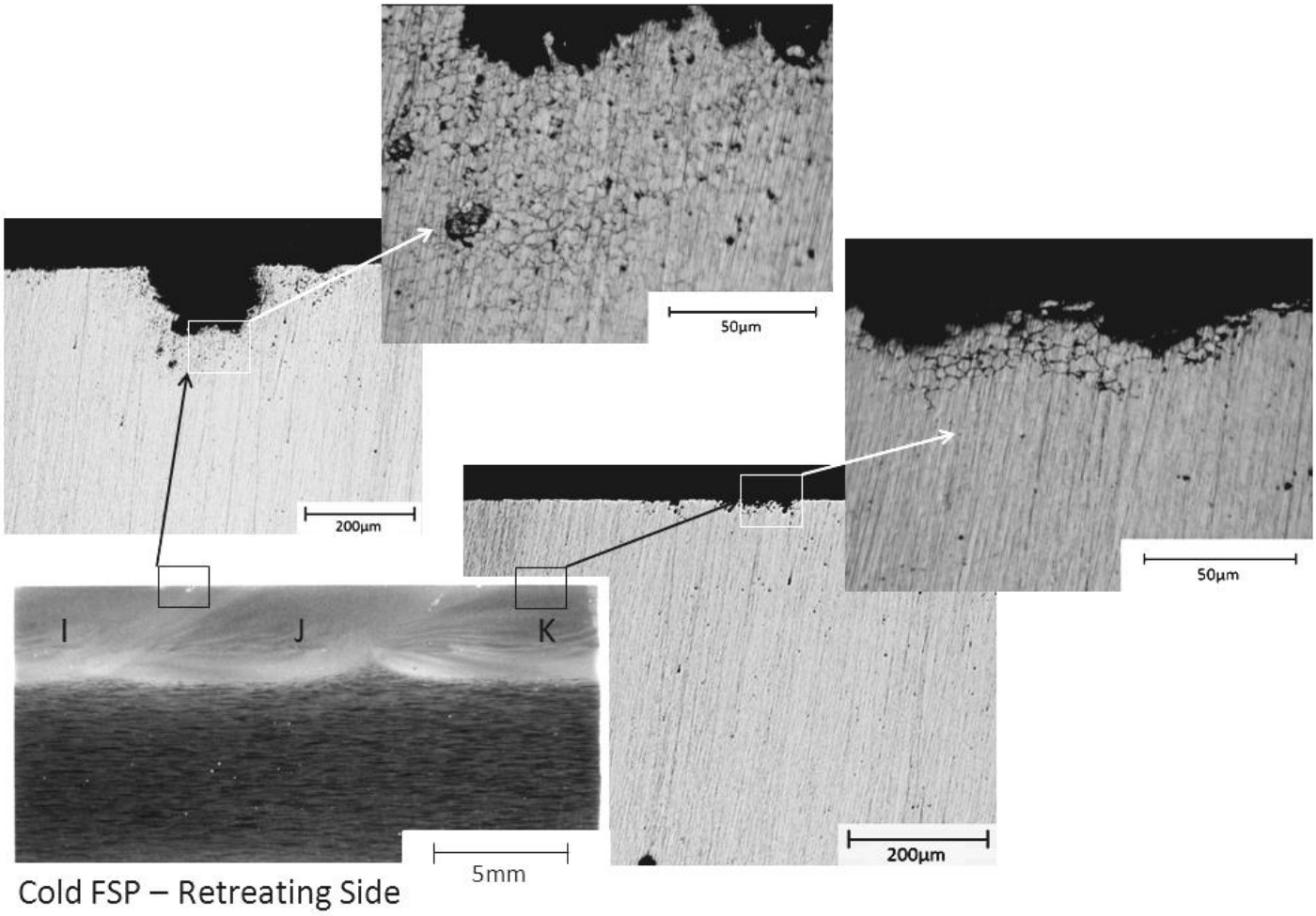

Figure 4.28 – A series of optical micrographs illustrating two examples of pitting with IGC at the interface of passes I-J, and the nugget of pass K in the cold FSP

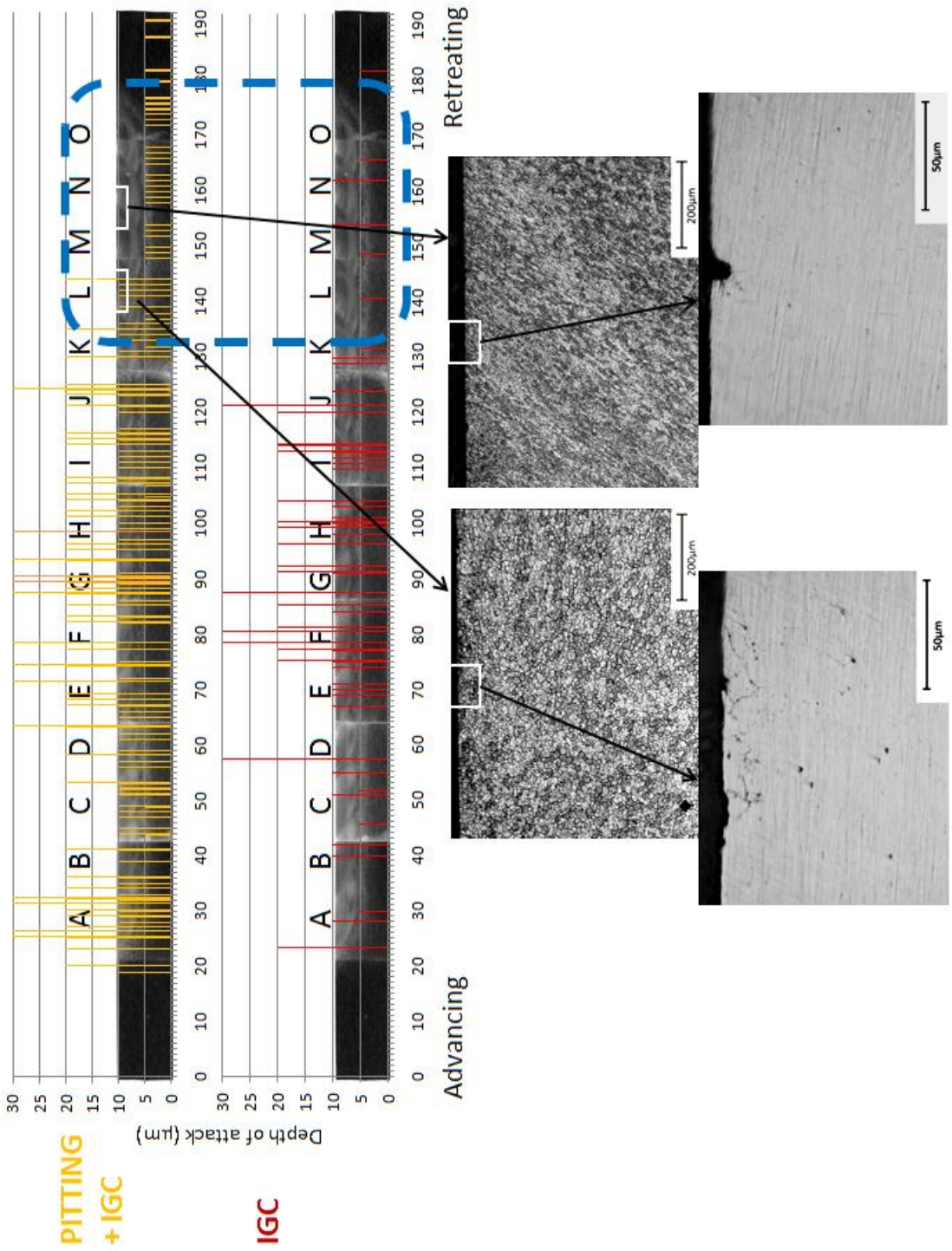

Figure 4.29 – A summary of the corrosion attack on the retreating side of the hot FSP

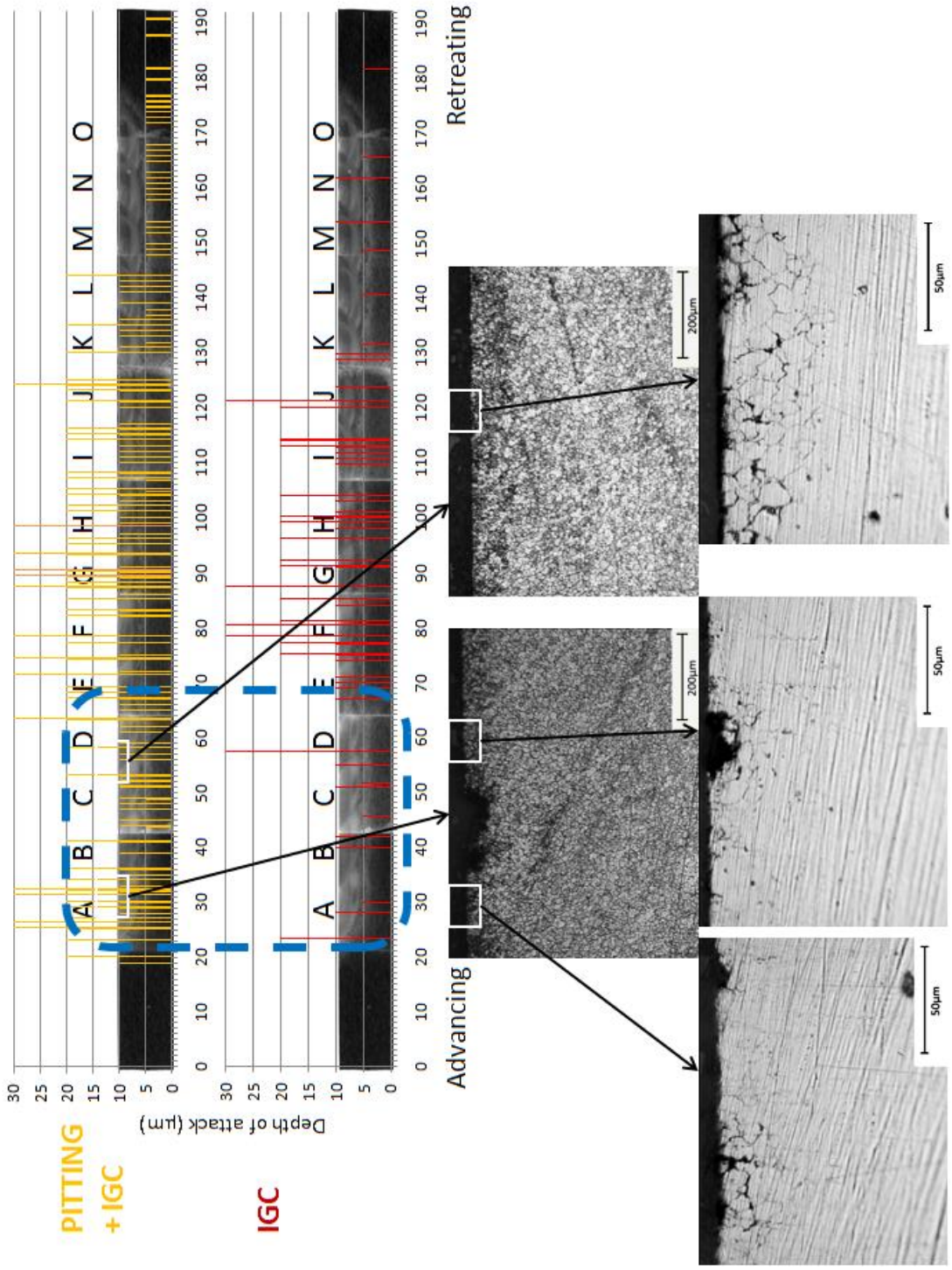

Figure 4.30 – A summary of the corrosion attack on the advancing side of the hot FSP

4.4.3 – FSW with Hot FSP (Retreating Side) Immersion Characteristics

As can be seen in Figure 4.29 and in Figures 4.21-4.24 the best performing FSP region was the retreating side of the hot FSP. Due to this, the region where the retreating side of the hot FSP covered the FSW was immersion tested and examined.

Figure 4.31 is a series of optical macrographs showing the retreating side of the hot FSP, with the perpendicular FS weld beneath. The photomicrographs illustrate the behaviour of the FSP and FSW following an identical 10 day 0.1 M NaCl immersion test to that carried out on the individual sections as described earlier, with the corrosion product still on the surface (b, d), and removed (a, e).

From these images it can be seen that there is little difference in terms of pitting severity or corrosion product deposition between either the FSP alone, the FSW alone, and the FSW with the FSP on top following the 10 day immersion test. All of the above conditions however are a considerable improvement on the unprocessed base material, which as can be seen in Figure 4.16, has suffered severe pitting and produced much more corrosion product on the untreated surface.

Similar to Figures 4.17-4.18 of the FSP alone, and in Figure 4.15 of the FSW, striations caused by the tool piece can be seen on the surface once the corrosion product has been removed in Figure 4.31(a, e). The striations follow the path of the trailing edge of the shoulder of the rotating tool piece. However upon closer inspection there was no difference in severity or distribution of attack across the surface to give reason for the visibility of the striations.

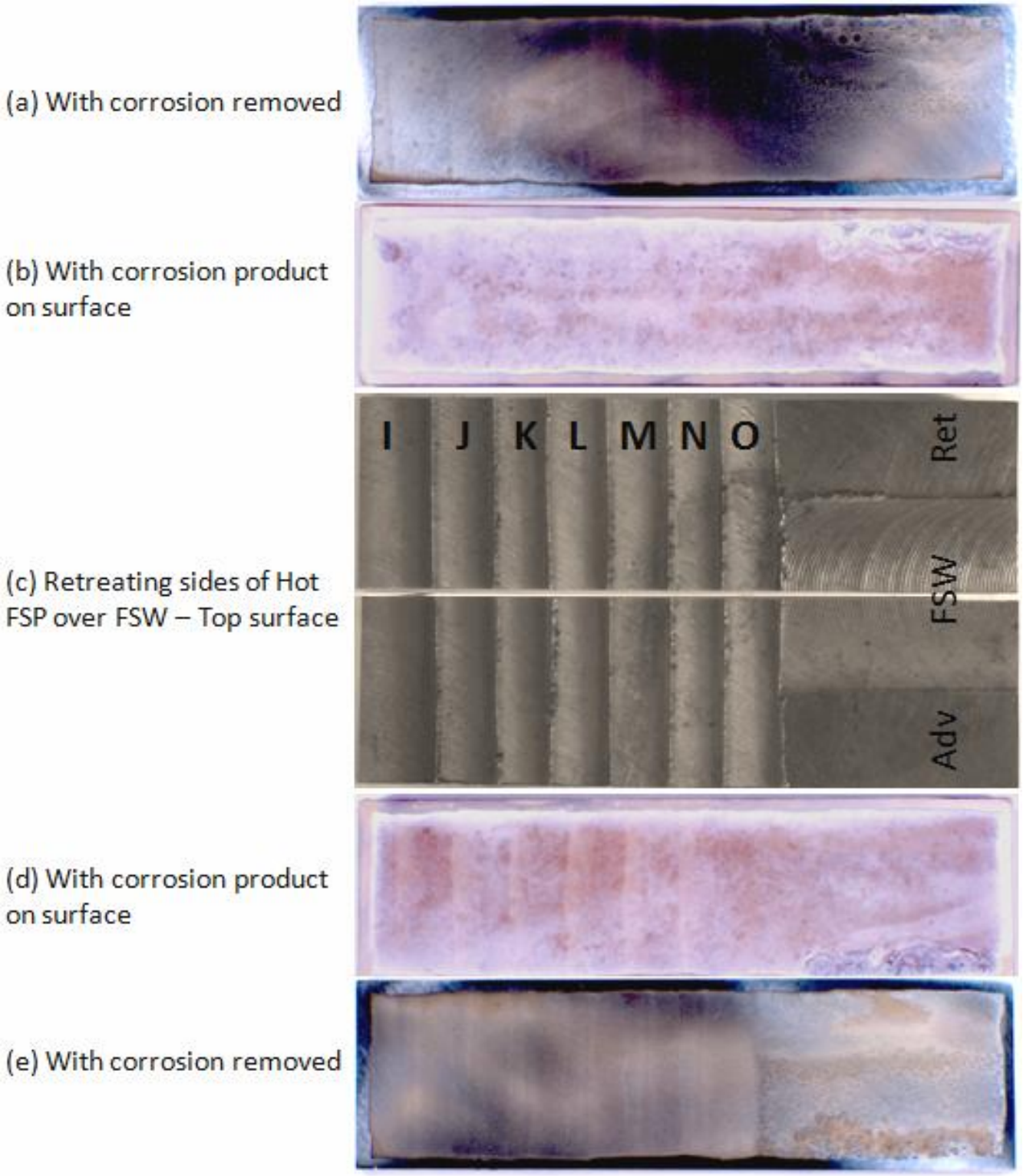

Figure 4.31 – Optical macrograph images showing; c) the top surface of the FSW with hot FSP (retreating side) with b), d) the corresponding surfaces following immersion testing with the corrosion product on the surface, and a), e) with the corrosion product removed

4.4.4 – FSW with Hot FSP (Retreating Side) Depth of Attack Analysis

The depth and mode of attack was analysed in an identical way to the FSW alone, and FSP alone. Three locations of cross-section were taken parallel to the nugget, TMAZ, and the HAZ of the weld, such that they were perpendicular to the FSP, and all of the surrounding material should be in the desired weld region. The three weld regions were selected due to the obvious differences in previous heat treatment and mechanical processing during the FSW before the following FSP across the surface. Figures 4.32-4.34 show the cross-sections of the three weld regions and surface FSP, with the locations and depth of corrosion attack. Only IGC, and IGC with pitting are shown as little or no sign of either pitting by itself, or intragranular attack was found across any of the processed material, just as in the FSW alone (Figures 4.21 (c-d)) and 4.22(c-d), and FSP alone (Figures 4.21 (a-b)) and 4.22(a-b).

4.4.4.1 – FSW Nugget with Hot FSP (Retreating Side) Depth of Attack

IGC

Figure 4.32(b) shows the locations and depths of IGC attack across the FSP in the nugget region of the FS weld. It is clear that the frequency of attack is reduced in the FSP material compared to the weld nugget alone. However the FSP treated area has still suffered from IGC attack, with almost all of the attack sites being 20 μm or deeper and the frequency is still fairly high.

As observed for the FSP alone, there appears to be no correlation between localised microstructure (nugget or TMAZ) of the FSP and the location or severity of attack. There were two small regions that produced increased IGC protection; the centre of pass L, and the transition between passes M-N however there was no apparent visible cause for this effect.

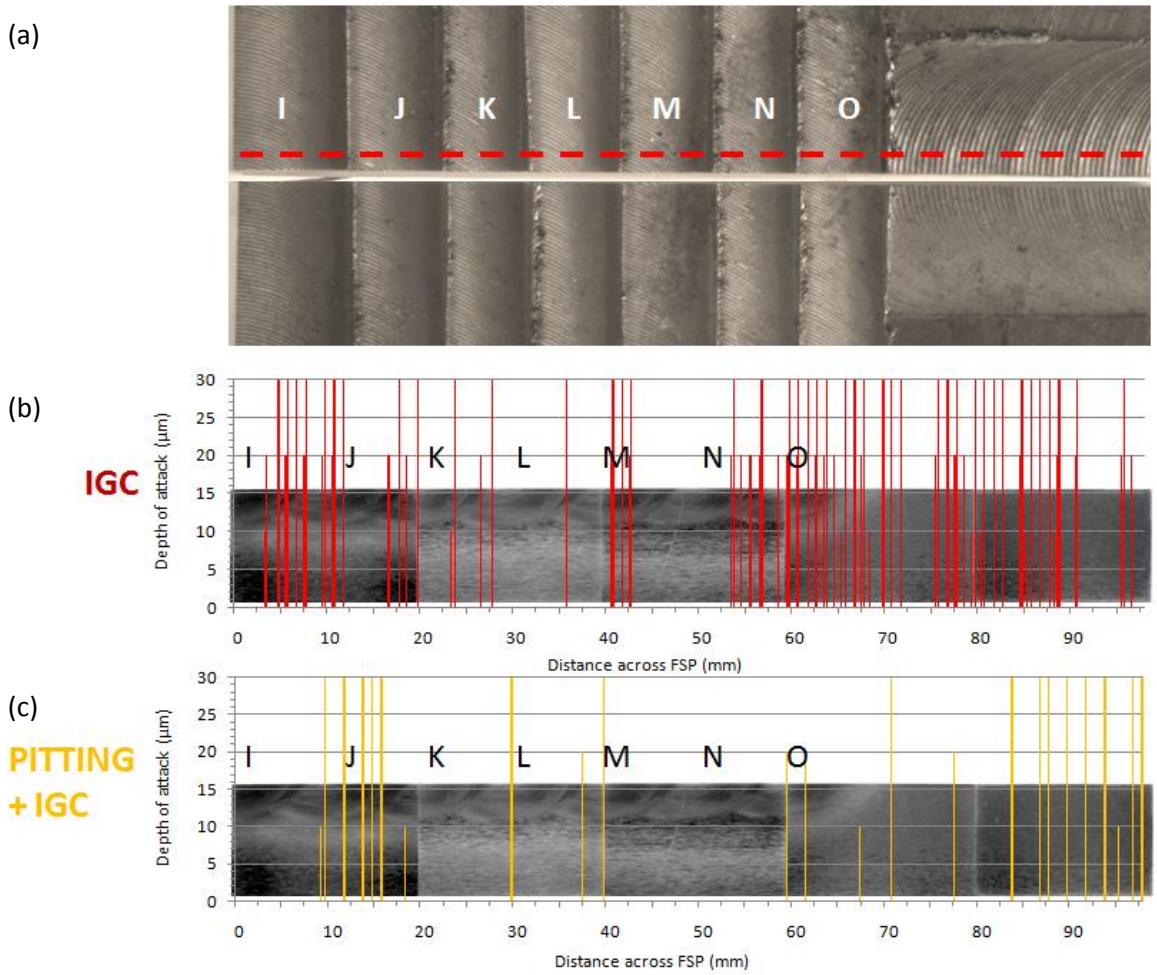

Figure 4.32 – A series of optical macrographs showing the locations and depths of attack for; (a) the nugget of the FSW and the retreating side of the hot FSP for (b) IGC attack, and (c) pitting with IGC attack

In comparison with the FSP alone, the nugget of the FSP-treated weld is significantly less IGC resistant, as shown in Figure 4.36(a, d). It can be seen that the IGC sites are far more severe and more frequent. Also the FS processed FSW nugget appears to be less IGC resistant than the FSW nugget without the FSP, as can be seen when Figures 4.25(d) and 4.36(a) are compared.

Pitting with IGC

Figure 4.32(c) shows the locations and depths of pitting with IGC attack across the FSP in the nugget region of the weld. It is evident that the there is a significant decrease in the frequency of attack sites compared to IGC attack across the same section of material. But similarly to the results for IGC alone, the depth of attack is usually 30 µm, with only two incidences of attack shallower than 10 µm across the FSP region. The FSP region does display improved pitting and IGC resistance compared with the unprocessed FSW nugget as the frequency of attack is much reduced, with passes K, and M-N displaying no attack sites.

It is difficult to determine whether the FSP-treated nugget of the FS weld is more or less resistant to pitting with IGC than FSP alone since the latter showed a high frequency of mostly shallow, 5-10 µm deep attack sites, whereas the FS treated weld nugget has produced a lower frequency of extremely deep (30µm) attack sites. In comparison with the untreated weld (Figure 4.25), the FS processed weld does appear to show a greatly reduced frequency of attack, which would suggest an improvement in resistance to pitting with IGC attack.

4.4.4.2 –FSW TMAZ with Hot FSP (Retreating Side) Depth of Attack

IGC

Figure 4.33(b) is a cross-section showing the locations and depths of IGC attack across the TMAZ of the FSP treated weld. Figure 4.33(b) suggests that the FS processed material is more IGC susceptible than the weld TMAZ without the FSP, as there are five times as many IGC sites across the FSP region than the untreated TMAZ. Also all but three of the sites across the FSP region are deep (30 µm or deeper) attack sites. The frequency of attack is much lower across the TMAZ than the weld nugget, with passes K-L, and M (Figure 4.33) displaying no IGC sites.

In comparison to FSP alone (Figure 4.36(d)), the FSW with the FSP performs slightly worse (Figure 4.36(b)); although the frequency of attack is similar, the depth of attack is far more severe in the FS processed weld. When compared to the FSW alone (Figure 4.25), the FS processed weld is again more susceptible to IGC, showing both an increase in attack depth and frequency.

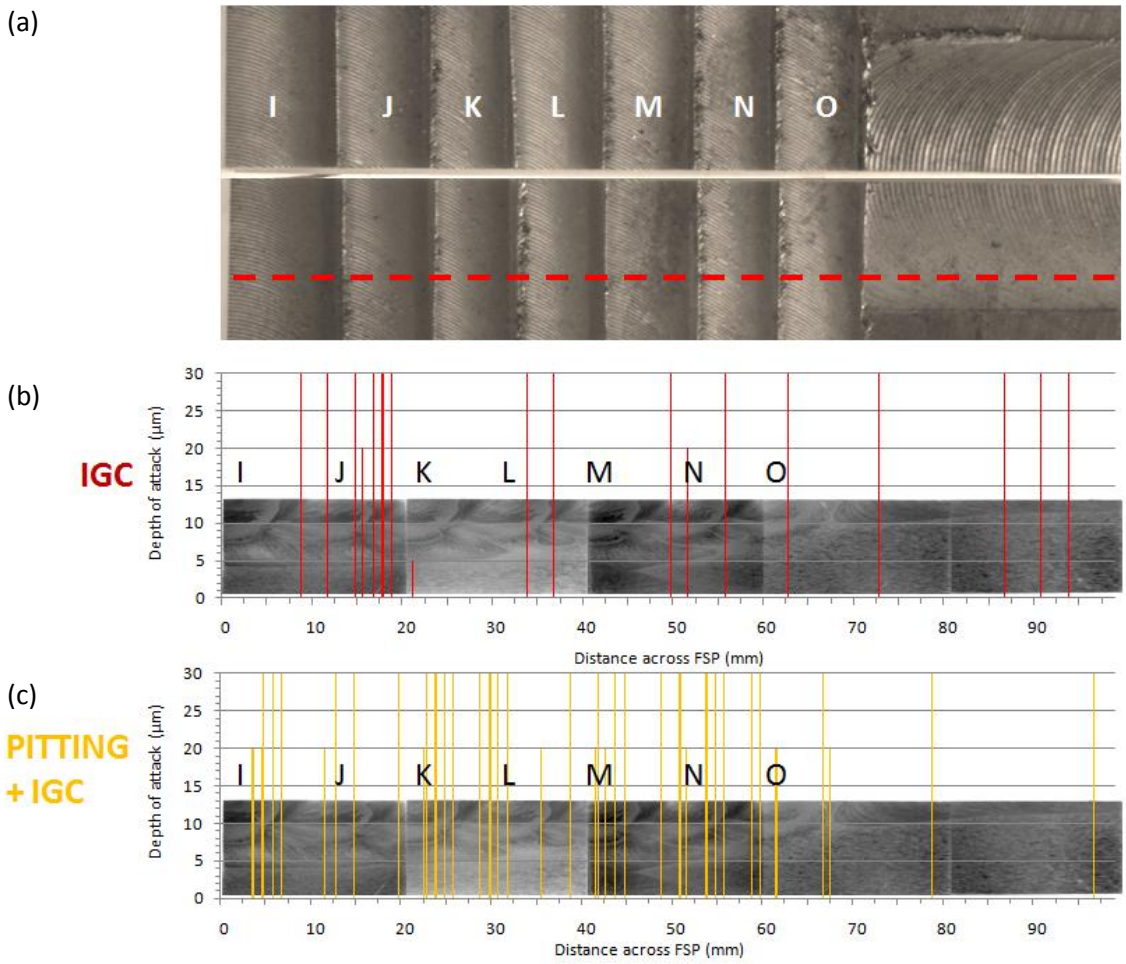

Figure 4.33 – A series of optical macrographs showing the locations and depths of attack for; (a) the TMAZ of the FSW and the retreating side of the hot FSP for (b) IGC attack, and (c) pitting with IGC attack

Pitting with IGC

Figure 4.33(c) shows the depths and locations of attack across the TMAZ region of the FS-processed weld. It shows that there is a high frequency of deep pitting with IGC attack sites across the FS treated region, and only two incidences of attack in the untreated weld TMAZ. None of the attack sites across the FS processed TMAZ were shallower than 20 µm, and there were no distinct regions of corrosion resistance.

In comparison to the FSP alone (Figure 4.36(d)) the FS processed weld TMAZ (Figure 4.36(b)) has a very similar frequency of attack. However, the depths of attack are far more severe for the FS processed weld, resulting in an increase in susceptibility to pitting with IGC attack. Compared with the untreated weld (Figure 4.25(c)), the FS processed weld (Figure 4.36(b)) again has a much higher frequency of attack, although both exhibit severely deep attack sites, although both exhibit severely deep attack sites.

4.4.4.3 – FSW HAZ with Hot FSP (Retreating Side) Depth of attack

IGC

Figure 4.34(b) shows a cross-section of the FS weld HAZ with the FSP and shows the depth and locations of IGC attack. Figure 4.34(b) also shows no data after 80 mm as the region of FSW HAZ without FSP suffered from severe exfoliation corrosion and thus the attack was not quantified in the same way as the above data.

The FS processed weld HAZ however appeared to suffer from significant IGC attack across the entire the FSP region. There were no regions of material that displayed any significant IGC resistance. In comparison with the FSP alone (Figure 4.36(d)), the weld HAZ with FS processing suffers slightly more attack sites, however the depth of attack throughout is far more severe with almost all sites reaching 30 µm deep. Compared to the cross-section of the untreated weld (Figure 4.25(d)) the FS processed HAZ is more susceptible to IGC attack.

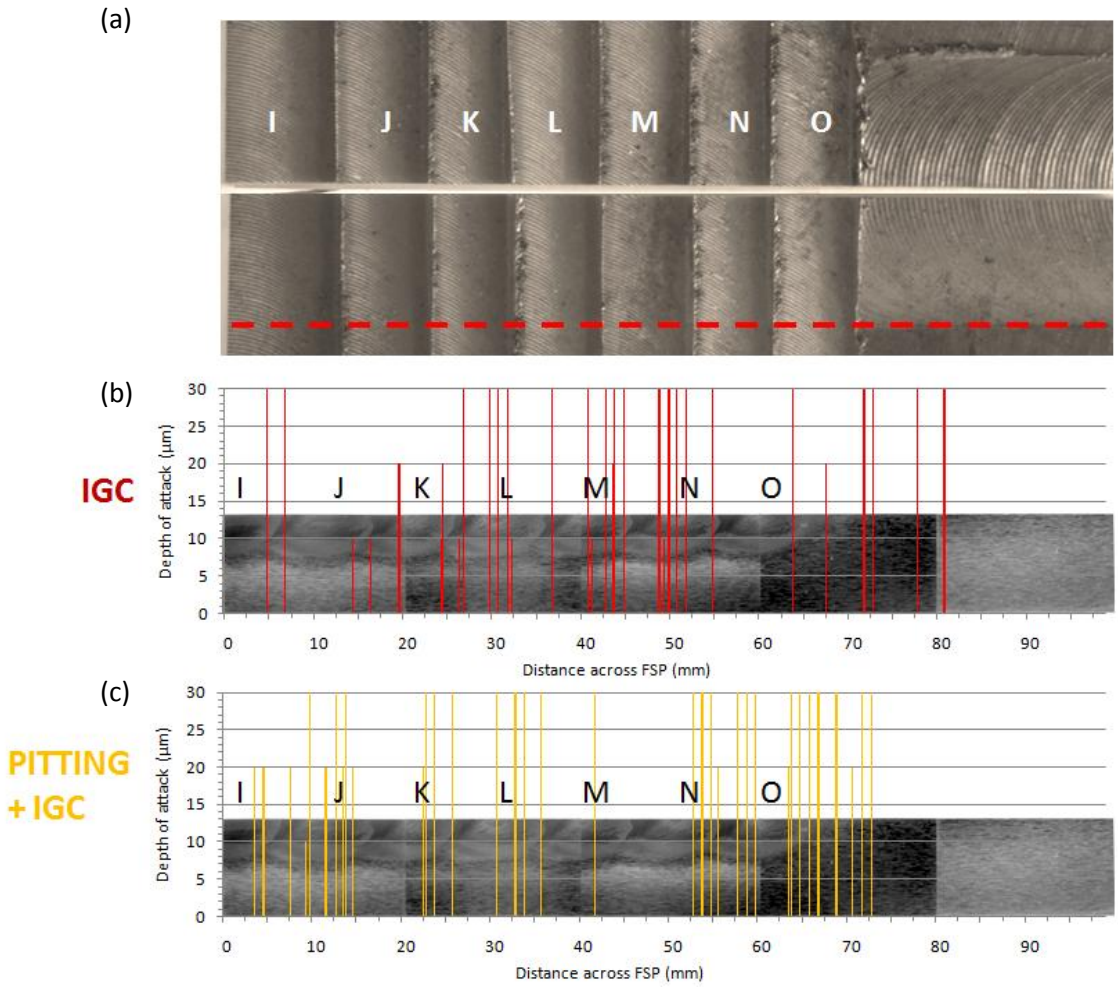

Figure 4.34 – A series of optical macrographs showing the locations and depths of attack for; (a) the HAZ of the FSW and the retreating side of the hot FSP for (b) IGC attack, and (c) pitting with IGC attack

Pitting with IGC

Figure 4.34(c) shows the locations and depths of attack of pitting with IGC across the HAZ of the FSW following FS processing. It can be seen there is a relatively high frequency of attack, and the sites identified were almost all severely deep, with only one at 10 µm or shallower. The only regions that displayed significant resistance to pitting with IGC were the transition between passes M-N, and J-K.

Compared with the FSP alone (Figure 4.36 (d)), the FSP over the FSW HAZ (Figure 4.36(c)) shows slightly fewer attack sites, however, the depth of attack is far more severe. Also the FS processed weld HAZ performs much worse than the untreated weld (Figure 4.25(c)), with significantly more pitting with IGC attack sites, particularly than at 2mm deep.

Exfoliation Corrosion

There is no data quantifying the frequency or depth of IGC or pitting with IGC beyond 80 mm in the FS processed FSW HAZ as shown in Figure 4.34 as exfoliation corrosion was observed after this point and so normal quantification was not possible. Figure 4.35 is a series of photomicrograph images showing the location and severity of the exfoliation attack. The photomicrographs of exfoliation corrosion in Figure 4.35**Error! Reference source not found.** are taken from a cross-section of the FSW HAZ in the longitudinal plane (rolling direction), unlike the images used in Figure 4.25 of the cross-section of the FSW in the transverse plane (end grain). The previous transverse plane examination of the FSW showed no signs of exfoliation corrosion in any weld regions.

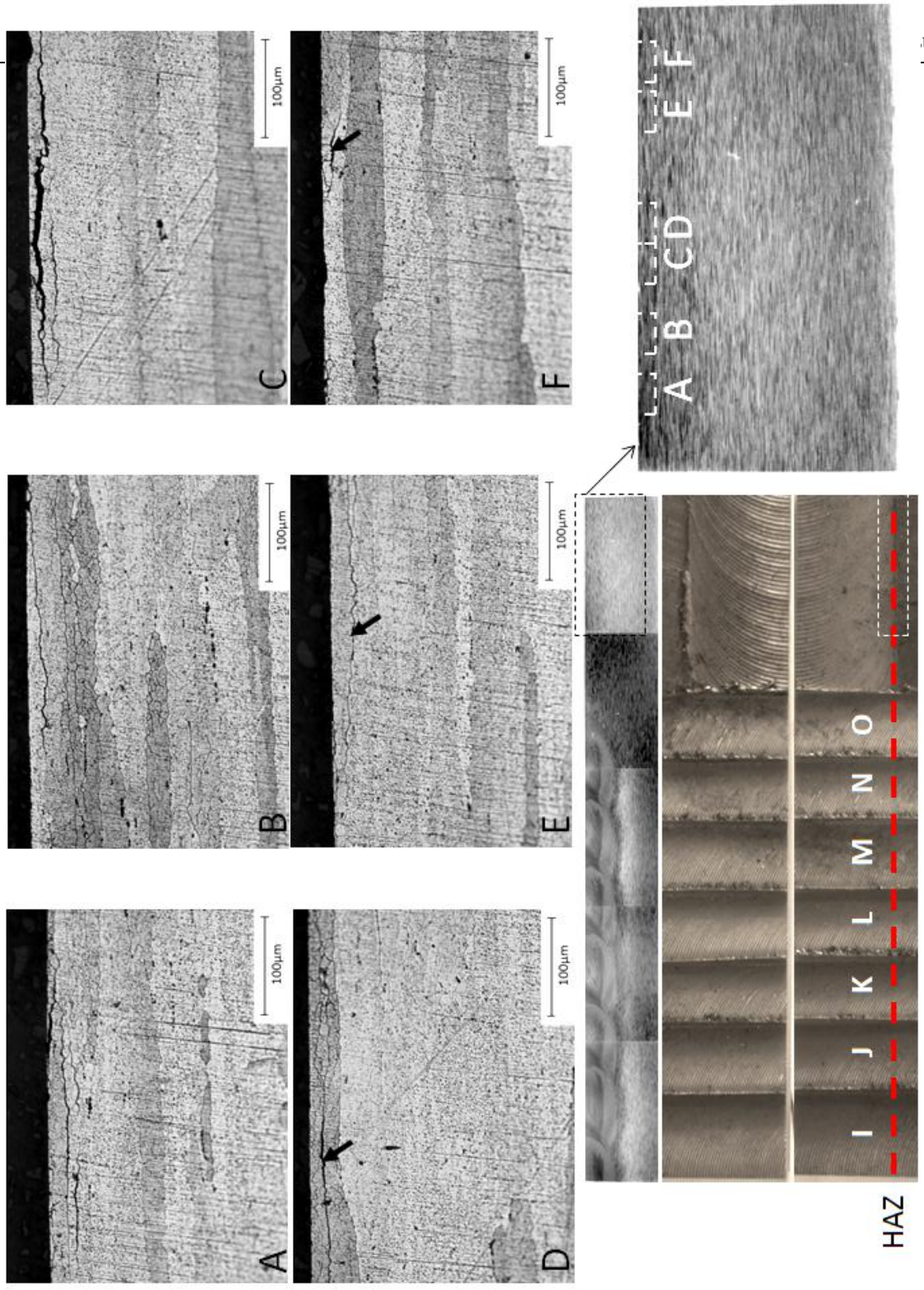

Figure 4.35 – A series of optical macrograph images showing incidences of exfoliation corrosion at the surface of the FSW HAZ without FSP protection taken from a cross-section in the longitudinal plane

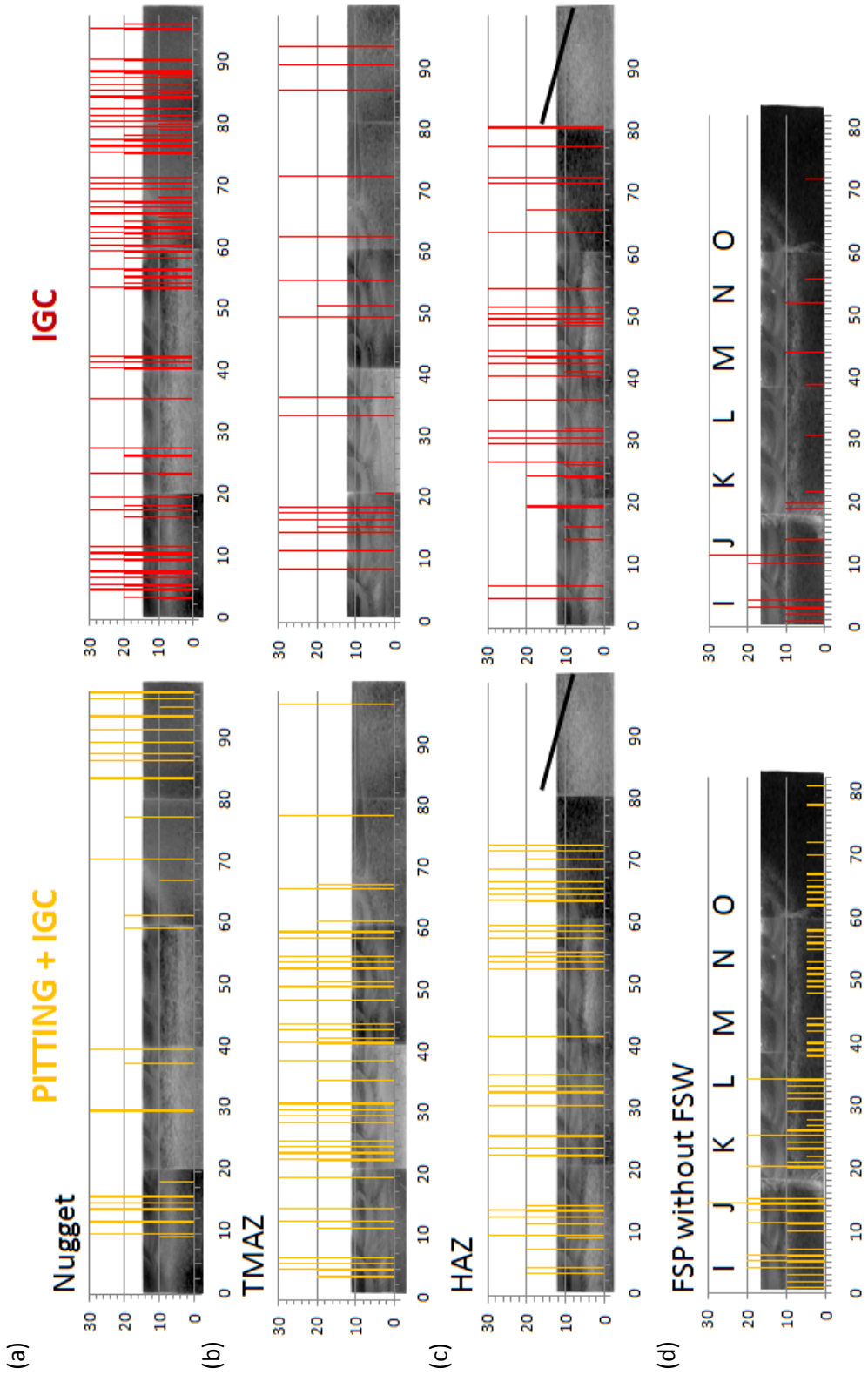

Figure 4.36 – A summary of corrosive attack of the hot FSW and hot FSP retreating side: Optical macrographs with corrosion data showing the locations and depths of IGC attack, and pitting with IGC attack for the (a) nugget (see Figure 4.32), (b) TMAZ (see Figure 4.33), and (c) HAZ (see Figure 4.34) of the FSW processed by the retreating side of the hot FSP, and (d) the FSP without the FSW (see Figure 4.30)

Chapter 5 – Discussion

5.1 – Base Material

This study used FSW AA2050-T851 to further investigate FSW and FSP corrosion properties in Al-Li alloys. In the T851 temper the alloy was solution heat treated before being cold worked (stretched 1.5-3.5%), and artificially aged (18h and 155°C) prior to welding and surface processing. In the T851 condition the alloy is expected to demonstrate optimum mechanical properties, as a result of stretching prior to artificial heat treatment to ensure good precipitation of strengthening phases [4]. This alloy is similar to that used in a previous study by Fendoni [57] on the effect of artificial post-weld heat treatment (PWHT) of FSW AA2050-T34, which was solution heat treated before being cold worked (stretched 1.5-3.5%), FS welded, and left to naturally age for one year before PWHT for various times at 155°C. A PWHT of 18h was investigated by Fendoni, and the base alloy used in that study is expected to be similar to the one used in the present work.

The base material is the alloy that was not subjected to any thermal or mechanical effects of friction-stir welding or processing. The base material hardness observed in this study was approximately 170Hv, whereas Fendoni recorded hardness values of 195-200Hv in AA2050-T34 following 18h PWHT specimens.

The corrosion behaviour of the base material in this study showed severe pitting parallel to the rolling direction and some intragranular corrosion but no IGC attack. Fendoni found the base material in the 18h PWHT specimen to show some signs of pitting attack, as well as IGC and intragranular corrosion following an identical 10 day 0.1M NaCl immersion test. In general it was observed that under-aged base material displayed mainly grain boundary attack, possibly due to the precipitation of T_1 at high energy grain boundaries as this

is the primary location for precipitation to occur, while over-aged base material suffered from mainly pitting and intragranular attack as precipitates coarsen in the matrix [57].

It is likely that in the T851 condition there is a uniform, low level of copper throughout the matrix, as well as at grain boundaries. From the results of this study and using the time-temperature-precipitation diagrams of AA2195 (see Figure 2.2) [15], a similar alloy to AA2050, it can be assumed that there is some precipitation of the active T_1 phase in the matrix, but a high concentration of T_1 forming at sub-grain boundaries leading to severe intragranular attack. From the observations and previous work it is possible that the base material in this study was effectively slightly over aged as the hardness had perhaps begun to fall and it suffered from only pitting and intragranular attack.

5.2 – Friction-Sir Weld

5.2.1 – Nugget

The nugget region consists of a fine equiaxed grain structure as a result of dynamic recrystallisation [35]. In the present study, it displayed a reduced severity of pitting attack, and no intragranular attack, but a higher frequency of severe IGC and pitting with IGC attack compared with the base material.

The FSW nugget recorded a microhardness of 130-135Hv, a slightly higher hardness than the TMAZ whilst still significantly lower than the base material. This slight increase is likely to be due to the fine microstructure rather than the precipitation of strengthening phases as there is a low dislocation density within the nugget following recrystallisation [59], and at such high temperatures (450-550°C [42]) it is difficult to precipitate T_1 phase. In addition, because the dislocation density is low, precipitates that do form are likely to form at grain boundaries and thus do not contribute to hardness. Copper-containing precipitates

forming at grain boundaries can produce copper-depleted zones adjacent to the grain boundary, rendering the nugget susceptible to IGC attack, which may explain this FSW nugget's corrosion behaviour. The immersion and MASMAASIS results show a decrease in pitting by itself, but an increase in IGC, and pitting with IGC.

In comparison with previous analysis of corrosion of FSW in AA2050, the weld produced for this study appears to have superior corrosion resistance. The study by Fendoni [57] using only thin gauge FSW AA2050-T34 (20 mm thick plate), displayed much poorer corrosion properties in the FSW nugget. Particularly in the as-welded condition, the TMAZ and HAZ showed severe pitting and IGC attack, although it is difficult to compare directly as the processing parameters were different, with a faster rotational speed (250rpm compared to 220rpm), and faster traverse speed (200 mm/min compared to 152 mm/min).

5.2.2 – Thermomechanically-Affected Zone

The TMAZ region is subjected to high temperatures and much plastic deformation due to the rotation of the tool piece during FSW. The TMAZ suffered from increased IGC attack but reduced pitting and no intragranular attack. At high temperatures typical of those found in the TMAZ of FSWs (350-450°C [3]), θ' phase forms at grain boundaries, which reduces the amount of copper in solid solution, and can produce copper depleted regions adjacent to the grain boundaries [40].

The severe levels of deformation that occur in the TMAZ should increase dislocation density, making precipitation in the matrix easier, however the high temperatures can cause strengthening precipitates to coarsen and become more widely distributed leading to bowing by dislocations. This is probably the case in this study as the lowest hardness of 115-120Hv was recorded in the TMAZ.

Previous research has seen a peak in the hardness within the TMAZ region of FSW AA2050. However the weld was carried out using faster traverse speeds (200 mm/min) on thinner 20mm gauge plate and was not through-thickness [57], whereas the nugget in the present study reached a depth of approximately 25 mm. It is possible that in the 20 mm gauge plate the temperatures produced in the TMAZ are sufficiently low enough not to cause such extensive over-ageing of precipitates, which may instead be easily nucleated and finely dispersed due to the increased dislocation density.

5.2.3 – Heat-Affected Zone

The HAZ is the region of material that is subjected to elevated temperatures of between 250-350°C [15, 40] due to the friction created during the welding process, but is not mechanically deformed. The microhardness testing showed a gradual decrease in hardness from approximately 170 Hv in the base material, to 120 Hv at the edge of the TMAZ.

When a cross-section was taken and examined in the transverse plane (end grain) following immersion testing of the top surface, the FSW HAZ showed some IGC, reduced pitting compared with the base alloy, but increased intragranular attack. The intragranular corrosion is likely to be as a result of θ' phase forming quickly first at sub-grain boundaries and secondly in the matrix at higher temperatures (approximately 300-350°C) close to the TMAZ [15]. While at lower temperatures (250-300°C), further away from the weld centre T_1 is the predominant phase that precipitates preferentially at sub-grain boundaries before forming in the matrix [15]. At the lowest temperatures within the HAZ (<250°C), closest to the base material there can be coarsening of T_1 in the matrix, but particularly at sub-grain boundaries [40]. These behaviours have also previously been observed in AA2050 [57],

where generally an increase in ageing time of the base material lead to an increase in intragranular.

MASTMAASIS testing showed the FSW HAZ was also susceptible to IGC attack, as well as a tendency to suffer exfoliation corrosion (see Figure 4.12). Following immersion testing, exfoliation corrosion was observed in the FSW HAZ when examined in the longitudinal plane (rolling direction) but not when examined in the transverse plane (end grain). This could be due to a number of reasons: it is possible that the corrosion propagates more easily in the rolling direction so more corrosion product was produced in the longitudinal section, and that this was not possible or visible in the transverse plane. Alternatively it may be that the cross-section taken in the transverse plane did not intersect any incidences of exfoliation corrosion, and that because it was only small attack in its early stages it was not visible from surface observations.

5.3 – Friction-Surface Processing

The friction surface processed regions consisted of a series of overlapping shallow FSW-like structures, such that all of the passes on the advancing side of the central pass were made up of only advancing characteristic FSW material, while all of the passes on the retreating side of the central pass consisted of only retreating material. In addition, half of each previous pass was erased as the next pass was formed, and the of HAZ subsequent passes was effectively within the previous pass. The two passes produced with different parameters, “hot” and “cold”, had different tool piece traverse speeds: the hot parameter traversed slower than the cold allowing more time to generate frictional heat at any given point.

With little recorded difference in hardness between the two parameters, the microhardness profiles of both hot and cold FSPs showed considerable scatter, but averaged between 100-120Hv, which was slightly lower than the centre of the FSW. This is possibly due to the extra heat input imposed on to previous passes leading to coarsening of the strengthening precipitates. The variation or scatter in microhardness may be explained by the presence of large intermetallic particles or precipitates.

The corrosion behaviour of FSP passes with both parameters generally followed the same pattern as the FSW in comparison with the base material, with no observations of intragranular attack across any FSP material, as well as a reduction in the severity of pitting attack, but again as with the FSW there was an increase in IGC and pitting with IGC. There was no obvious correlation between the location of the attack sites (nugget, TMAZ, or transition regions across the FSP) and mode of corrosion, or the varied scatter of microhardness, and the change in microstructure across either FSP. Furthermore, each pass creates a HAZ which is imposed on to the nugget of the previous pass, which can effectively be considered as a rudimentary localised post-weld heat treatment on the surrounding area. The increased susceptibility to IGC is likely to be as a result of similar mechanisms occurring in FSW TMAZ and nugget, caused by precipitation of active phases and copper depleted regions at grain boundaries.

Previous research on the post-weld heat treatment of AA2050-T34 has found increased susceptibility to IGC with increased ageing time [57], although processing parameters have a large influence on the corrosion susceptibility of FSW and FSP.

5.4 – Effect of FSP on the Corrosion Behaviour of FSW

Due to time constraints, only the best performing region (retreating side of the hot FSP) was examined closely as a method of corrosion protection of the FSW. It is important to note that all cross-sectional microstructural analysis of the FSW treated with hot FSP were made in the longitudinal plane, such that the analysed sections were perpendicular to the FSP but parallel to the FSW to ensure only the desired FSW region (nugget, TMAZ, or HAZ) was under examination.

There were clear differences in the severity of IGC and pitting with IGC attack between the FSP alone and the FSP covering the FSW, as well as differences in the severity and most prevalent mode of attack in the nugget, TMAZ, and HAZ (see Figure 4.36). The weld nugget suffered predominantly IGC attack, while the TMAZ suffered predominantly pitting with IGC attack, and the HAZ had roughly equal frequencies of both IGC and pitting with IGC attacks. However, as can be seen in Figure 4.36, the FSP over the surface of the FSW suffered from an increase in the frequency and severity of IGC and pitting with IGC in all three FSW regions. The differences in corrosion behaviour are interesting as one would expect the two FSP regions to behave similarly as performing FSP across and material surface, be it base material or FSW, should totally eradicate any previous processing history. Furthermore, exfoliation corrosion was observed in the untreated FSW HAZ, but not in the region that had been treated by FSP. Exfoliation corrosion was also seen in the HAZ of the untreated FSW following MASTMAASIS testing.

The differences observed in the selected cross-sections may be significant real effects, or may be results of statistical variations throughout the processed material. More microstructural characterisation would be required to confirm any real effect, as well as further repeated measurements at different points through the FSP and FSW to account for

statistical variability. For that reason the observations made of the FSW in the longitudinal plane should be treated with caution.

It does however appear that FSP may decrease the incidence of exfoliation corrosion in the FSW HAZ, which would be beneficial. This is likely to be due to both the fine microstructure of the FSP which, unlike the pancake like grains of the base material, does not promote the rapid propagation of exfoliation, as well as a possibly reduced susceptibility of grain boundaries in the FSP region.

Chapter 6 – Conclusions

This study explored the use of friction-surface processing as a method of corrosion protection for a thick plate friction-stir welded Al-Cu-Li alloy AA2050-T851.

The base material suffered severe pitting and intragranular attack, with no signs of IGC. The FSW, although showing good corrosion resistance compared to a previous Al-Li-Cu alloy FSW, did suffer from IGC and pitting with IGC in the nugget and TMAZ, while the HAZ suffered from minor IGC attack and exfoliation corrosion. The FSPs showed some promising signs of improved corrosion resistance in areas, particularly the retreating side of the hot FSP.

Disappointingly, a possible increased susceptibility to IGC and pitting with IGC was created at the surface upon combining the FSW and retreating side of the hot FSP. However, the FSP did show promise as a method for protecting the FSW HAZ from exfoliation corrosion.

In the future, further work should be undertaken in a more extensive study to ensure results are more statistically significant. Particular attention should be made to relate varying processing parameters with the resulting microstructure, specifically regarding the role copper depletion in IGC and exfoliation corrosion. Investigations into processing parameters, particularly thinner ‘colder’ surface processed layers, and the use of rapid cooling to prevent the impact of heat transfer during each pass could prove beneficial. With regards specific aerospace applications, the assessment of environmentally assisted cracking and fatigue susceptibility following corrosion using relevant geometries.

Chapter 7 – References

1. Balmuth, E.S. and R. Schmidt, *A perspective on the development of aluminum-lithium alloys*, in *Aluminum-Lithium Alloys*, T.H. Sanders Jr and E.A. Starke Jr., Editors. 1981, The Metallurgy Society of AIME: Stone Mountain, Georgia. p. 69-88.
2. Thomas, W.M., et al., *Friction Stir Welding*. 1991: GB patent no. 9125978-8.
3. Mishra, R.S. and Z.Y. Ma, *Friction stir welding and processing.* Materials Science & Engineering R-Reports, 2005. **50**(1-2): p. 1-78.
4. Polmear, I.J., *Wrought aluminium alloys, in Light Alloys (Fourth Edition)*. 2005: Butterworth-Heinmann: Oxford. 97-204.
5. Campbell, F.C., *Manufacturing Technology for Aerospace Structural Materials*. 2006: Elsevier.
6. Martin, J.W., *Aluminum-Lithium Alloys.* Annual Review of Materials Science, 1988. **18**: p. 101-119.
7. Silcock, J.M., *The structural aging characteristics of aluminum-copper-lithium alloys.* Journal of Institute of Metals, 1959. **88**.
8. Starke Jr., E.A. and W.E. Quist, *The Microstructure and Properties of Aluminum-Lithium Alloys.* New Light Alloys, 1990(174): p. 1-23.
9. Cassada, W.A., G.J. Shiflet, and E.A. Starke, *The effect of plastic-deformation on Al_2CuLi (T_1) precipitation.* Metallurgical Transactions a-Physical Metallurgy and Materials Science, 1991. **22**(2): p. 299-306.
10. Huang, B.P. and Z.Q. Zheng, *Independent and combined roles of trace Mg and Ag additions in properties precipitation process and precipitation kinetics of Al-Cu-Li-(Mg)-(Ag)-Zr-Ti alloys.* Acta Materialia, 1998. **46**(12): p. 4381-4393.
11. Kumar, K.S., S.A. Brown, and J.R. Pickens, *Effect of a prior stretch on the ageing response of an Al-Cu-Li-Ag-Mg-Zr alloy.* Scripta Metallurgica Et Materialia, 1990. **24**(7): p. 1245-1250.
12. Gayle, F.W., F.H. Heubaum, and J.R. Pickens, *Structure and properties during aging of an ultra-high strength Al-Cu-Li-Ag-Mg alloy.* Scripta Metallurgica Et Materialia, 1990. **24**(1): p. 79-84.
13. Sanders, R.E. and E.A. Starke, *Effect of grain refinement on low-cycle fatigue behaviour of an aluminium-zinc-magnesium-(zirconium) alloy.* Materials Science and Engineering, 1977. **28**(1): p. 53-68.
14. Gu, B.P., et al., *Application of the Weibull density-function to describe the delta'-(Al_3Li) particle-size distribution in binary Al-Li alloys.* Materials Science and Engineering, 1986. **78**(1): p. 71-85.
15. Chen, P.S. and B.N. Bhat, *Time-Temperature-Precipitation Behaviour in Al-Li alloy 2195*. 2002, National Aeronautics and Space Administration, Washington, DC 20546-0001.
16. Kumar, K.S., S.A. Brown, and J.R. Pickens, *Microstructural evolution during aging of an Al-Cu-Li-Ag-Mg-Zr alloy.* Acta Materialia, 1996. **44**(5): p. 1899-1915.
17. Cassada, W.A., G.J. Shiflet, and E.A. Starke, *Electron-diffraction studies of Al_2CuLi (T_1) plates in an Al-2.4Li-2.4Cu-0.18Zr alloy.* Scripta Metallurgica, 1987. **21**(3): p. 387-392.
18. Thompson, G.E. and G.C. Wood, *Corrosion: Aqueous Processes and Passive Films*. 1982: Academic Press London.
19. Shreir, L.L., R.A. Jamin, and G.T. Burstein, *Corrosion Metal/Environment Reactions*, in *Aluminium and Aluminium Alloys*. 1994, Butterworth-Heinemann Ltd.
20. http://corrosion-doctors.org/Corrosion-Thermodynamics/Potential-pH-diagram-aluminum.htm.
21. Muller, I.L. and J.R. Galvele, *Pitting potential of high purity binary aluminium alloys II. Al-Mg and Al-Zn alloys.* Corrosion Science, 1977. **17**: p. 995-1007.

22. Paglia, C.S. and R.G. Buchheit, *The time-temperature-corroison susceptibility in a 7050-T7451 friction stir weld.* Materials Science and Engineering A, 2008. **492**(1-2): p. 250-254.
23. Galvele, J.R. and Demichel.Sm, *Mechanism of intergranular corrosion of Al-Cu alloys.* Corrosion Science, 1970. **10**(11): p. 795-&.
24. Li, J.F., et al., *Exfoliation corrosion and electrical impedence spectroscopy of an Al-Li alloy in EXCO solution.* Materials and Corrosion, 2007. **58**(4): p. 273-279.
25. Kelly, D.J. and M.J. Robinson, *Influence of heat treatment and grain shape on exfoliation corrosion of Al-Li alloy 8090.* Corrosion, 1993. **40**(10): p. 787-795.
26. Vargel, C., *Corrosion of Aluminium*. First Edition ed. 2004: Elsevier.
27. Kumai, C., *Influence of aging at 200°C on the corrosion resistance of Al-Li and Al-Li-Cu alloys.* Corrosion, 1989. **45**(4): p. 294-302.
28. Wall, F.D. and G.E. Stoner, *The evaluation of the critical electrochemical potentials influencing environmentally assisted cracking of Al-Li-Cu alloys in selected environment.* Corrosion Science, 1997. **39**(5): p. 835-853.
29. Ricker, R.E. and D.J. Duquette, *Potentiodynamic polarization studies of an Al-Mg-Li alloy*. Aluminium-Lithium Alloys II, ed. E.A. Starke and J.T.H. Sanders. 1983: Monterey, California.
30. Buchheit, R.G., J.P. Moran, and G.E. Stoner, *Electrochemical Behavior of the T1 Intermetallic Compound and its Role in Localized Corrosion of Al- 2% Li- 3% Cu Alloys.* Corrosion, 1994. **50**(2): p. 120-130.
31. Kertz, J.E., P.I. Gouma, and R.G. Buchheit, *Localized corrosion susceptibility of Al-Li-Cu-Mg-Zn alloy AF/C458 due to interrupted quenching from solutionizing temperatures.* Metallurgical and Materials Transactions a-Physical Metallurgy and Materials Science, 2001. **32**(10): p. 2561-2573.
32. Li, J.F., et al., *Corrosion mechanism associated with T1 and T2 precipitates of Al-Cu-Li alloys in NaCl solution.* Journal of Alloys and Compounds, 2008. **460**(1-2): p. 688-693.
33. Colligan, K., *Material flow behavior during friction stir welding of aluminum.* Welding Journal, 1999. **78**(7): p. 229S-237S.
34. Dawes, C.J. and W.M. Thomas, *Friction stir process welds aluminum alloys.* Welding Journal, 1996. **75**(3): p. 41-45.
35. Nandan, R., T. DebRoy, and H.K.D.H. Bhadeshia, *Recent advances in friction-stir welding - Process, weldment structure and properties.* Progress in Materials Science, 2008. **53**: p. 980-1023.
36. Fujii, H., et al., *Effect of tool shape on mechanical properties and microstructure of friction stir welded aluminum alloys.* Materials Science and Engineering a-Structural Materials Properties Microstructure and Processing, 2006. **419**(1-2): p. 25-31.
37. Sato, Y.S., M. Urata, and H. Kokawa, *Parameters controlling microstructure and hardness during friction-stir welding of precipitate-hardenable aluminum alloy 6063.* Metallurgical and Materials Transactions A, 2002. **33A**: p. 625-635.
38. Su, J.Q., T.W. Nelson, and C.J. Sterling, *Grain refinement of aluminum alloys by friction stir processing.* Philosophical Magazine, 2006. **86**(1): p. 1-24.
39. Fonda, R.W., J.F. Bingert, and K.J. Colligan, *Development of grain structure during friction stir welding.* Scripta Materialia, 2004. **51**: p. 243-248.
40. Shukla, A.K. and W.A. Baeslack, *Study of microstructural evolution in friction-stir welded thin-sheet Al-Cu-Li alloy using transmission-electron microscopy.* Scripta Materialia, 2007. **56**: p. 513-516.
41. Ma, Z.Y., R.S. Mishra, and M.W. Mahoney, *Superplastic deformation behaviour of friction stir processed 7075Al alloy.* Acta Materialia, 2002. **50**: p. 4419-4430.
42. Rhodes, C.G., et al., *Effects of friction stir welding on microstructure of 7075 aluminum.* Scripta Materialia, 1997. **36**(1): p. 69-75.
43. Jata, K.V. and S.L. Semiatin, *Continuous dynamic recrystallization during friction stir welding of high strength aluminum alloys.* Scripta Materialia, 2000. **43**(8): p. 743-749.

44. Hassan, K.A.A., et al., *Effect of welding parameters on nugget zone microstructure and properties in high strength aluminium alloy friction stir welds.* Science and Technology of Welding and Joining, 2003. **8**(4): p. 257-268.
45. Prangnell, P.B. and C.P. Heason, *Grain structure formation during frictioin stir welding observed by the 'stop action technique'.* Acta Materialia, 2005. **53**: p. 3179-3192.
46. Threadgill, P.L., *Friction stir welding - A state of the art joining technique*. 1999, TWI.
47. Krishnan, K.N., *On the formation of onion rings in friction stir welds.* Materials Science and Engineering a-Structural Materials Properties Microstructure and Processing, 2002. **327**(2): p. 246-251.
48. Booth, D.P.P., M.J. Starink, and I. Sinclair, *Analysis of local microstructure and hardness of 13 mm guage 2024-T351 AA friction stir welds.* Materials Science and Technology, 2007. **23**(3): p. 276-284.
49. Mahoney, M.W., et al., *Properties of friction-stir-welded 7075 T651 aluminum.* Metallurgical and Materials Transactions a-Physical Metallurgy and Materials Science, 1998. **29**(7): p. 1955-1964.
50. Leonard, A.J. *Friction stir welding*. in *TWI 2nd International Symposium*. 2000. Gothenburg, Sweden.
51. Mishra, R.S., Z.Y. Ma, and I. Charit, *Friction stir processing: a novel technique for fabrication of surface composite.* Materials Science and Engineering a-Structural Materials Properties Microstructure and Processing, 2003. **341**(1-2): p. 307-310.
52. Lathabai, S., et al., *Friction Stir Processing: A Technique for Microstructural Refinement in Metallic Materials*, in *Light Metals Technology 2009*, M.S. Dargusch and S.M. Keay, Editors. 2009, Trans Tech Publications Ltd: Stafa-Zurich. p. 63-67.
53. Mishra, R.S. and M.W. Mahoney, *Friction stir processing: A new grain refinement technique to achieve high strain rate superplasticity in commercial alloys*, in *Superplasticity in Advanced Materials, Icsam-2000*, N. Chandra, Editor. 2001, Trans Tech Publications Ltd: Zurich-Uetikon. p. 507-512.
54. Ma, Z.Y., *Friction stir processing technology: A review.* Metallurgical and Materials Transactions a-Physical Metallurgy and Materials Science, 2008. **39A**(3): p. 642-658.
55. Elangovan, K. and V. Balasubramanian, *Influences of pin profile and rotational speed of the tool on the formation of friction stir processing zone in AA2219 aluminium alloy.* Materials Science and Engineering a-Structural Materials Properties Microstructure and Processing, 2007. **459**(1-2): p. 7-18.
56. Su, J.Q., T.W. Nelson, and C.J. Sterling, Scripta Materialia, 2005. **52**: p. 135-140.
57. Fendoni, A., *The effect of post weld heat treatment on the corrosion behavior of a AA2050T34-FSW*. 2009, The University of Birmingham. p. 1-113.
58. Threadgill, P.L., et al., *Friction stir welding of aluminium alloys.* International Materials Reviews, 2009. **54**(2): p. 49-93.
59. Sato, Y.S., et al., *Microstructural evolution of 6063 aluminum during friction-stir welding.* Metallurgical and Materials Transactions a-Physical Metallurgy and Materials Science, 1999. **30A**.
60. Jariyaboon, M., et al., *The effect of welding parameters on the corrosion behaviour of friction stir welded AA2024-T351*. Corrosion Science, 2007. **49**(2): p. 877-909.
61. Paglia, C.S., et al. *Strength, corrosion, and environmentally assisted cracking of a 7075-T6 friction stir weld*. in *8th International Conference on Aluminium Alloys*. 2002. Cambridge, England: Trans Tech Publications Ltd.
62. Paglia, C.S., et al. *The corrosion and environmentally assisted cracking behavior of high strength aluminum alloys friction stir welds: 7075-T651 vs. 7050-T7451*. in *Symposium on Friction Stir Welding and Processing II*. 2003. San Diego, Ca: Minerals, Metals & Materials Soc.
63. Bala Srinivasan, P., et al., *Effects of inhibitors on corrosion behaviour of dissimilar aluminium alloy friction stir weldment.* Corrosion Engineering, Science and Technology, 2007. **42**(2): p. 161-167.

64. Surekha, K., B.S. Murty, and K.P. Rao, *Microstructural characterization and corrosion behavior of multipass friction stir processed AA2219 aluminium alloy.* Surface & Coatings Technology, 2008. **202**(17): p. 4057-4068.
65. Surekha, K., B.S. Murty, and K.P. Rao, *Effect of processing parameters on the corrosion behaviour of friction stir processed AA 2219 aluminum alloy.* Solid State Sciences, 2009. **11**(4): p. 907-917.
66. Wadeson, D.A., et al., *Corrosion behaviour of friction stir welded AA7108 T79 aluminium alloy.* Corrosion Science, 2006. **48**: p. 887-897.
67. Corral, J., et al., *Corrosion of friction-stir welded aluminum alloys 2024 and 2195.* Journal of Materials Science Letters, 2000. **19**(23): p. 2117-2122.
68. Frankel, G.S. and Z. Xia, *Localized corrosion and stress corrosion cracking resistance of friction stir welded aluminum alloy 5454.* Corrosion, 1999. **55**(2): p. 139-150.
69. Zucchi, F., G. Trabanelli, and V. Grassi, *Pitting and stress corrosion cracking resistance of friction stir welded AA 5083.* Materials and Corrosion-Werkstoffe Und Korrosion, 2001. **52**(11): p. 853-859.
70. *http://www.wmtr.com/Content/AstmG85A2.htm.*